GROWTH AND CHARACTERIZATION OF Ga_2O_3, $(Ga_{1-x}Gd_x)_2O_3$ & $(Ga_{1-x}Fe_x)_2O_3$ THIN FILMS BY PULSED LASER DEPOSITION

by

Md Dalim Mia, M.S.

A dissertation submitted to the Graduate Council
of Texas State University in partial fulfillment
of the requirements for the degree of
Doctor of Philosophy
with a Major in Materials Science, Engineering and Commercialization
August 2020

Committee Members:

Ravi Droopad, Chair

Craig Hanks

Larry Larson

Wilhelmus Geerts

Maggie Chen

COPYRIGHT

by

Md Dalim Mia

2020

FAIR USE AND AUTHOR'S PERMISSION STATEMENT

Fair Use

Duplication Permission

DEDICATION

To my eldest brother, Md Mozibur Rahman, a man with loving heart

ACKNOWLEDGEMENTS

At first, I would like to express my sincerest gratitude to my supervisor, Prof. Ravi Droopad, who has supported me throughout this journey by his patience and expertise, while allowing me to explore research in my own way. Without his guidance and support, my PhD work would not have been completed. Only few people have the privilege to work under someone as caring and understanding as him. I simply could not have wished for a friendlier and better supervisor.

I am also grateful to the committee members of my dissertation Dr. Wilhelmus J. Geerts, Dr. Maggie Chen, Dr. Craig Hanks, Dr. Larry Larson for their time and valuable suggestions. I am especially grateful to Dr. Wilhelmus Geerts, who helped me a lot beyond his regular schedule in analyzing data and instrumentation, and to Dr. Maggie Chen for letting me use her lab for optical characterization.

I would like to thank my collaborators Dr. Luisa Scolfaro and Dr. Pablo D. Borges for performing theoretical calculations for the $(Ga_{1-x}Fe_x)_2O_3$ alloy and sharing their knowledge and guidance.

Special thanks to Dr. Casey Smith and Nate England for their assistance on various technical measurements and troubleshooting of the various instruments. I learned a lot from them in our discussion and meetings.

I would like to acknowledge my colleagues Brian Samuels, Md Abdul Ahad Talukder, Sourav Das, and Zachary Fox, for assistance in some experimentation and analysis. Special thanks to Brain C Samuels, who supported me from the beginning while

troubleshooting instruments, providing guidance with data collection, and bringing new insights to our discussions.

I would like to acknowledge my friends Shafiqur Rahman, Susmita Ghose, Md Anwar Siddique, Mehedhi Hasan, Raju Ahmed, and Rony Saha for their constant assistance and sharing their knowledge and skills.

I also would like to express my gratitude to my parents, sisters, brothers and to my wonderful wife Easrat Haque for always supporting me.

Finally, I would like to acknowledge that this work was supported in part by NSF through an DMR-MRI Grant under Award 1726970.

TABLE OF CONTENTS

Page

LIST OF TABLES

Table **Page**

LIST OF FIGURES

Figure **Page**

ABSTRACT

Thin film wide bandgap Ga_2O_3 based alloys are important for applications in high power electronic, deep UV photonic devices and nuclear detectors. Such alloys can be deposited epitaxially by pulsed laser deposition on c-plane sapphire substrates with varied compositions. This work enables the development of heterostructures with Ga_2O_3 and bandgap tunable device structures with a variety of functionalities. Examples include the use of Gd in the alloy for higher bandgap material which can be used as a gate dielectric in MOSFET devices, and due to the high nuclear cross section of Gd, for nuclear radiation detectors. Alloys containing Fe can be used for the development of high bandgap magnetic devices and high resistive buffer layers for FET applications. Combinations of these thin film alloys open the possibility of heterostructure devices that includes HEMT and quantum well UV optoelectronics. Being motivated by these reasons, this thesis work focused on the growth optimization and characterization of $(Ga_{1-x}Gd_x)_2O_3$ & $(Ga_{1-x}Fe_x)_2O_3$ thin films using pulsed laser deposition.

Epitaxial $(Ga_{1-x}Gd_x)_2O_3$ & $(Ga_{1-x}Fe_x)_2O_3$ thin films with varied x were successfully grown on c-plane sapphire substrates to tune the optical and structural properties using variations in the growth parameters. High growth temperatures favor the formation of the monoclinic $(Ga_{1-x}Gd_x)_2O_3$ phase; the higher the Gd composition, the greater the growth temperature required for high quality crystalline thin films. UV-vis measurements demonstrate a slight red shift of the bandgap (4.99eV~4.82eV) in comparison with the pure β-Ga_2O_3.

Successfully grown, both spinel and monoclinic $(Ga_{1-x}Fe_x)_2O_3$ thin films exhibit room temperature ferromagnetism, which can be used for the fabrication of nonvolatile semiconductor memories, magneto-optic devices, and microelectronics. Incorporation of Fe into Ga_2O_3 expands the lattice constant eventually transforming the crystal structure from the monoclinic to the spinel phase for $x>0.1$. Optical transmission measurements show that with increasing Fe content the absorption edge moves toward longer wavelengths with the introduction of an intermediate band. Similarly, high oxygen pressure introduces intermediate bands, while low oxygen pressure eliminates defects as well as induces a phase transformation from the monoclinic to the spinel phase. On the other hand, the thermally induced spinel structures transform to the monoclinic phase during a high temperature anneal in an oxygen environment. Chemical composition, surface states, optical properties, and crystal structure were systematically evaluated by several techniques. XRD and pole figure analysis were used to distinguish the crystal phase. X-ray photoelectron spectroscopy measurements suggest that the $(Ga_{1-x}Fe_x)_2O_3$ alloy contains a mixture of Fe^{3+} and Fe^{2+} valence states in the films. However, higher oxygen pressure during growth and annealing favors formation of Fe^{3+} over Fe^{2+}.

1. INTRODUCTION AND RESEARCH MOTIVATION

Essentially, wide bandgap semiconducting materials with high electron mobility, negative electron affinity, excellent thermal conductivity, and high electrical breakdown voltage are important for high power devices. More importantly a heterostructure having a two-dimensional electron gas (2DEG) channel, especially due to the polarization effect, as in the case of GaN, have been utilized in the development of important electronic applications [1]–[3]. Because of their wide bandgaps, these materials, including oxides, also find applications in UV detectors, UV-transparent conductive films, and have the potential for microwave switching and amplification. Currently, the leading semiconductor materials that have been developed for transistor logic are based on silicon (Si) while those for high speed opto-electronics are based on compound semiconductors. The properties of Si have been extensively studied and it has been the preferred semiconductor material in the 20^{th} and 21^{st} century because of its abundancy, easy mechanical handling, and ease for mass production. However, Si has inherent limitations in detector technology because it is an indirect bandgap material, and in high power, high frequency applications because of its relatively narrow room temperature bandgap (~1.12 eV) , resulting in low electrical breakdown voltage, limiting high voltage performance at elevated temperatures. Additionally, the search for wide bandgap diluted magnetic semiconductor oxide (DMS) has been a growing interest in the research community for spintronics and magnetic sensor applications. These limitations are motivating researchers to investigate alternative wide bandgap binary and ternary compounds and their alloys, which can be used in moderate or high temperature, in high-power opto-electronic and spintronics applications.

Alternative materials, for example, SiGe, InP, GaAs, SiC, ZnO, ZnS, and GaN have been under extensive study to meet the demand for power conversion electronics [4]. In power electronic applications, a small ON resistance is required while providing high blocking voltages in the OFF state. High blocking voltage requirements can only be satisfied using thicker layers of conventional semiconductors, which limit the miniaturization of power electronics systems. However, implementing wide bandgap semiconductors with ultra-high breakdown voltages can offer orders of magnitude reduction in system size, cost, and weight. Breakdown voltages and bandgaps are related by a power exponential, and the universal relationship between them is expressed as $E_c = a\ (E_g)^n$, where E_c and E_g are the breakdown voltage and energy gap respectively, α is the ionization rate of holes and electrons, n is in the range of 2-2.5 [5],[6],[7] . Hence, electric breakdown voltage, which primarily depends on the bandgap, is a key parameter for switching devices to reduce leakage current and facilitate power devices with reduced sizes.

Therefore, based on material parameters, SiC and GaN are preferred materials for power switching devices due to their higher breakdown voltage as well as provide for high power density devices [4]. For the social and technological demand, much effort has been placed on the research and development of GaN and SiC based devices. However, there are still many barriers to exploiting their full potential such as the lack of high crystal quality substrates which leads to materials dislocation and grain boundaries in device structures that leads to high manufacturing cost, low yield, efficiency and stability that ultimately determine the adoption of a technology for society.

More recently, an emerging viable wide bandgap candidate, beta gallium oxide (β-Ga_2O_3), which is widely known as a 'solar-blind' photoconductor, has attracted a great deal of attention for next generation power electronics by virtue of its exceptionally wide optical bandgap. In addition, it has been predicted to have a high electrical breakdown voltage (V_{br}), and suitability for mass production as compared to its SiC and GaN counterparts [8]. β-Ga_2O_3 also has tremendous commercial potential by reason of high quality, larger size wafers that can be manufactured from single crystal bulk synthesized by melt-growth methods such as the vertical Bridgman method, and the Czochralski, floating-zone and edge defined film-fed growth techniques [9]–[15]. In contrast, manufacturing bulk crystal of SiC and GaN wafers requires complex vapor growth techniques which are very expensive. This is a great advantage for Ga_2O_3 and suggest that Ga_2O_3 devises might be more commercially successful as compared to existing wideband gap technologies.

Ga_2O_3 also has great potential in detector technology. O vacancies cause a change in the conductivity by absorption of various gases, a characteristic that can be used for gas detection [16], [17] . The large bandgap (~4.9eV) of Ga_2O_3 makes it optically transparent at all wavelength above ~250 nm. These properties make it potentially useful as a transparent electrode or transparent conducting oxide for solar cell and other optical devices. Also, the conductivity of Ga_2O_3 can be changed from an insulator to a conductor based on the growth conditions and doping concentration[18]–[21] . Furthermore, the search for dilute magnetic semiconductor (DMS) materials has been of great interest from the industrial point of view because of their potentiality as new functional materials, which can open a way to fabricate novel functional semiconductor devices [22]. The

Ga_2O_3 conduction electron's spin generates the magnetic memory effect, and various researchers have demonstrated ferromagnetic and magnetoelectric properties above room temperature, which can be a good alternative to the commonly used ferromagnetic material $BiFeO_3$ [23]–[27]. Diet et al. worked on room temperature ferromagnetism in magnetically doped semiconductors, which ignited significant research efforts on semiconductors having wider bandgap (>3eV), particularly GaN and ZnO [28], [29]. Thus, doping, or alloying of Ga_2O_3 with Fe can be useful for ferromagnetic applications at room temperature or higher.

To further utilize the potential of Ga_2O_3, the use of bandgap engineering and heterostructure designs that have brought significant attention to the scientific research arena, can be utilized. The alloy of Ga_2O_3 with Al and In can provide bandgap tunability which can be used in device design and optimization with enormous freedom. High electron mobility transistors (HEMTs) based on $Al_xGa_{1-x}O_3/Ga_2O_3$ has demonstrated the presence of a 2DEG channel through Si modulation doping [30]-[31]. Similar wide bandgap alloys ZnMgO (3.3~7.7 eV) [32] and AlGaN (3.4 ~ 6.2 eV) [33] have also been studied due to their large bandgap that enable them to work in the UV range for detection of 160nm-375nm and 200 to 365nm wavelengths respectively. However, successful fabrication of alloys of Ga_2O_3, for example, AlGaO and InGaO can be tuned from 3.5 ~ 8.6 eV [34],[35], [36]. This feature unlocks a new horizon in designing UV photodetectors in a wider range of 125 to 375nm. However, research activities in the growth and characterization of Ga_2O_3 alloys is still in its infancy [34]. Alloying Ga_2O_3 with Fe_2O_3 and Gd_2O_3 can offer the opportunity to tailor the optical bandgap, through the formation of compositional dependent bandgaps, and hence electrical and optical

properties. As a result, it is important to develop an understanding on their alloys in terms of growth, stability, and properties, both structural, electrical, and optical.

Currently the most widely used transparent conductive oxides (TCO) for optical devices are ITO, ZnO, SnO_2, and In_2O_3. But, with a small optical bandgap (~3eV) these materials are limited in their applications for a wide spectral range [37]. Gallium oxide (Ga_2O_3), is considered to have the widest bandgap among the transparent conducting oxides (TCO) [38] with a refractive index of 1.84-1.88 at 980 nm wavelength, and has been used for an anti-reflective coating on GaAs with reflectivity as low as 10^{-5} and a small absorption coefficient of about 100 cm^{-1} [21],[5]. It remains transparent in the visible to UV optical range with doping, for example, doping with Al, In, Sn, Ge, and Si. Since doping concentration or alloying changes its structural, optical and electrical properties, this makes Ga_2O_3 a promising material to be used for a broader range of applications such as solar cell, graded heterostructures for optoelectronics applications, photodetectors having tunable cutoff wavelength, and optical filters with tunable transmission range or transparent substrates for GaN based LED growth [39],[40].

Ga_2O_3 is a comparatively unexplored materials with a large bandgap. Five well known polymorphs of gallium oxide exist: α- Ga_2O_3, β-Ga_2O_3, γ-Ga_2O_3 , δ- Ga_2O_3 and ε-Ga_2O_3. Among them the monoclinic structure β-Ga_2O_3 is most stable phase and the majority of current research is based on this polymorph. However, other phases may have more attractive materials properties and applications by manipulating its spin by photons, possessing intrinsic cation vacancies and large bandgap that make polymorphs such as γ- Ga_2O_3 potential candidates for next generation DMS devices. As an example, Mn doped γ- Ga_2O_3 has excellent ferromagnetic properties at room temperature, as well

as excellent light emitting characteristics in the ultraviolet regions [41], [42],[43]. DMS which contain spin and charge degrees of freedom in a single material has attracted tremendous interest since ferromagnetism in $In_{1-x}Mn_xAs$ [44] and $Ga_{1-x}Mn_xAs$ [45] was discovered. Nevertheless low magnetic ordering temperatures in these systems limits applications at room temperatures [46], [47] . Although, immense work has been carried out for wide bandgap DMS materials, such as, on Mn doped GaN [48], its ferromagnetism above room temperature is still being debated. Ga_2O_3 with Fe content can be a strong candidate for ferromagnetic applications. For example, recently reported epitaxial growth of ferromagnetic $(Ga_{1-x}Fe_x)_2O_3$ thin films for Fe content ($x < 9.62\%$) by the PLD technique [49] has been demonstrated.

The goal of this work is to study the effect of the growth parameters on the structural, optical, and magnetic properties of $(Ga_{1-x}Gd_x)_2O_3$ and $(Ga_{1-x}Fe_x)_2O_3$ thin films for various Gd and Fe content(x), respectively. Crystal structure and crystal quality were explored using X-Ray diffraction (XRD), pole figure (PF) and phi scan analysis. Along with XRD, X-Ray photoelectron spectroscopy (XPS) and energy dispersive spectroscopy (EDS) were used to determine chemical composition, oxidation state and atomic concentration. Atomic force microscopy (AFM) and Scanning electron microscopy were used to explore the surface morphology- grain size, grain boundaries and roughness. UV spectroscopy was used to extract the bandgap by extrapolating the linear region of the absorption spectrum. Results were compared with ellipsometry measurement. Magnetization versus magnetic field (M-H), were investigated using vibrating sample magnetometer (VSM). Finally, the effect of high temperature in an O_2 atmosphere of the properties of $(Ga_{1-x}Fe_x)_2O_3$ was investigated.

1.1 State of the Art

Although Ga_2O_3 has five phases, the β-Ga_2O_3 is the most stable polymorph. As a result, most of the recent study has been based on the monoclinic β-Ga_2O_3 structure. In addition, studies on β-Ga_2O_3 have been partly accelerated due to the availability of crystalline β-Ga_2O_3 substrates, as well as the rapid development of homoepitaxy and some success with n-type impurity doping. Growth on non-native substrates has also been evolving quickly with significant development in high quality epitaxy, alloying and doping control [50]. Controlling carrier concentration by doping is crucial to the development of β-Ga_2O_3 in optoelectronic applications. To produce n-type conductivity in typical compound semiconductors, normally used dopants impurities include Si, Ge, and Sn. In Ga_2O_3 these work as shallow donors, have lower activation energy, and can substitute onto Ga sites. Similarly, F and Cl act as shallow donors through substitutional doping at the O site [51]. N-type doping has been successful with conductivity being tunable over a wide range of magnitude, 10^{-12} – 10^{2} S/cm [52],[53]. Sasaki et al. [54] reported on MBE growth Sn doped n-type β-Ga_2O_3 thin films with electron concentrations ranging from 10^{16}-10^{19} cm^{-3} on semi-insulating Mg doped β-Ga_2O_3 (010) substrate.

The bulk mobility of β-Ga_2O_3 has been predicted to be 182cm^2/(V.s), while in the presence of two dimensional electron gas (2DEG) the expected mobility is about 418 cm^2/V [55] . Baldini et al. [56] reported maximum mobility of 41 cm^2/(Vs) for a carrier density of $10^{18}cm^{-3}$ in Sn doped β-Ga_2O_3 thin films grown by metal organic vapor-phase epitaxy (MOVPE). Ahmadi et al. studied Ge doping of β-Ga_2O_3 films using [57] plasma assisted molecular beam epitaxy (PAMBE) as the growth method, and achieved

mobilities of 97 $cm^2V^{-1}s^{-1}$ for charge density of 1.6×10^{18} cm^{-3}. K. D. Leedy et al. [58] studied Si-doped Ga_2O_3 thin films fabricated by pulsed laser deposition (PLD) on semi-insulating (010) β-Ga_2O_3 and (0001) Al_2O_3 substrates. In this study the authors reported conductivity of 732 S/cm^{-1} with a mobility of 26.5 cm^2/Vs for carrier concentration of 1.74×10^{20} cm^{-3}. In addition, the lowest specific contact resistance (4.6×10^{-6} Ωcm^2) and resistivity (1.4 mΩ.cm) through Si ion implantation doping in β-Ga_2O_3 was achieved for electron density 5×10^{19} cm^{-3} [59].

He et al.[60] studied the electronic properties of Cr, Fe, Mn, and Ni doped β-Ga_2O_3 using first principle calculations. They have shown that in these doped materials one spin polarized state exists around the Fermi level and predicted ferromagnetism for Mn and Ni doped material and spin glass ground states for Cr and Fe doped β-Ga_2O_3. Atanelov et al. [61] performed ab initio density-functional theory calculations to study the electronic and magnetic properties of $GaFeO_3$ for different Fe/Ga ratios. They found incorporating dopants and applying strain alters the intrinsic structure of the material resulting in magnetic properties of gallium ferrite.

In principle, one way to accomplish high resistive β-Ga_2O_3 is to introduce divalent ions- Zn^{2+}, Fe^{2+}, Mg^{2+} and Be^{2+} into the lattice that substitute into the trivalent site [62], [63], [64], [65]. Fe-doped Ga_2O_3 ($Ga_{1.95}Fe_{0.05}O_3$) thin films were grown on c-plane Al_2O_3 substrates at different temperatures (450, 550, 650 and 750^o C) and oxygen pressures (10^{-5}, 10^{-4}, 10^{-3}, 10^{-1} Pa) using laser molecular beam epitaxy (LMBE). The results obtained provided evidence that Fe doped Ga_2O_3 can be a promising candidate for homogenous epitaxial gate dielectric material on Ga_2O_3-based high-power electronic devices [62].

Guo et al. [66] have investigated the growth and magnetic properties of Ga_2O_3 /$(Ga_{1-x}Fe_x)_2O_3$ multilayer thin films on (0001) sapphire substrate fabricated by alternating deposition of Ga_2O_3 layer and Fe ultrathin layer using LMBE. They controlled the thickness and composition of $(Ga_{1-x}Fe_x)_2O_3$ solely by changing the number of laser pulses during each run for depositing Fe while fixing the number of laser pulses for the deposition of the Ga_2O_3 layer thereby digitally approximating a ternary material. Measurements revealed room temperature ferromagnetism with high ultraviolet transparency of the multilayer films with a cut off wavelength of 250nm.

While n-type doping of Ga_2O_3 was successful, there are few reports on the existence of p -type Ga_2O_3 . The band structure predicted that it may be impossible to create p-type Ga_2O_3 materials due to the nature of the valence band [67], [68]. Alexandros Kyrtsos et al. [52] investigated various cation substitutional impurities Li, Na, K, Be, Mg, Ca, Cu, Au and Zn for effective p-type doping in Ga_2O_3 using density functional theory. They found these dopants introduce deep acceptor levels with ionization energy greater than 1eV. In addition, they might create deep trap levels which hinder p-type conductivity.

More recently, donors and acceptors in β-Ga_2O_3 were studied by Neal et al. [69]. They have studied the properties of deep acceptors Fe, Mg and shallow donors Si, Ge in β-Ga_2O_3 by temperature dependent van der Pauw and Hall measurements of samples grown by different methods: edge defined film fed, molecular beam epitaxy, Czochralski and chemical vapor deposition. They were able to precisely determine the donor energy for Ge and Si to be 30meV. In case of Fe doped β-Ga_2O_3, acceptor energy was determined to be 860meV with respect to the conduction band for the Fe deep acceptor,

and Van der Pauw measurements of Mg doped β-Ga_2O_3 revealed higher activation energy of 1.1eV. In addition, various researchers have been investigating Cr, Ce, Eu, Ni, and Nd doped β-Ga_2O_3, that revealed interesting electrical and optical properties [70]–[76]. Growth, doping, electrical, optical, and structural properties of β-Ga_2O_3 are not well established. Repetition and reproducing result, as well as investigating new properties will be essential to bring maturity this wide bandgap oxide material system.

In the case of device applications, gallium oxide and its alloy has gained tremendous attention in the field of UV detectors, gas sensors, power devices (MESFET, MOSFET), and fin-array field effect transistor [77], [78], [79]. For example, ultra-wide bandgap and conductive β-Ga_2O_3 has been an attractive choice for adoption as new solar blind photodetector materials. The most reported Ga_2O_3 solar blind photodetector in the literature is a metal-semiconductor-metal (MSM) structure most commonly deposited on sapphire substrates [50]. Osama et al. [80] investigated a MSM β-Ga_2O_3 UV detector on c-plane sapphire substrate by PAMBE. This device demonstrated a small dark current of 1.2nA, and a photoresponsivity of 0.037A/W under 254nm UV illumination at 10V bias voltage. Hu et al. [81] studied Ga_2O_3 photodetectors with interdigitated electrodes. The highest responsivity and quantum efficiency (Q.E) were 17A/W and 8228% respectively for a 20V bias voltage around 255nm, amongst best value reported. These high values were ascribed to the Au electrode providing an arena for carrier multiplication. Even higher values of spectral responsivity (259 A/W) and EQE (7.9×10^4 %) were reported by Liu et al. [82]. Several groups, recently, have reported improved performance of MSM β-Ga_2O_3 UV detector by doping with Si, Sn, Zn etc.[83], [84], [85],[64]. Other research is also being conducted and is based on heterostructures including β-Ga_2O_3/Nb:$SrTiO_3$, β-

Ga_2O_3/ZnO, β-Ga_2O_3/GaN, β-Ga_2O_3/p-Si etc. [86], [87], [88], [89]. Though the results support the progress of β-Ga_2O_3 deep solar blind photodetector, improvement in the epitaxial crystal quality would enable detailed studies on reproducible doping control and device performance enhancement.

Furthermore, beside extensive research on the ternary alloys such as $(Al_xGa_{1-x})_2O_3$ [90]and $(In_xGa_{1-x})_2O_3$ [91], researchers have been putting their attention to the quaternary alloy, for example, β-$(Al_xIn_yGa_{1-x-y})_2O_3$ [66]. Quaternary alloys have been successfully accomplished among group III-Nitride and III-V materials to generate desirable performance [92]. Quaternary alloys are expected to have further improved materials properties such as deep UV detection and increased mobility for the Ga_2O_3 based transistor development.

Along with the most stable phase of β-Ga_2O_3, research on other polymorphs such as γ- Ga_2O_3, ε- Ga_2O_3, δ- Ga_2O_3 and α-Ga_2O_3 is poorly investigated. There are only a few reports for these metastable phases. Recently they are being considered for various versatile applications and researchers are investigating ways to stabilize these metastable structures. These phases are thought to have wide bandgap and potential scientific and technological application in optoelectronics (solar blind photodetectors, phosphor and electroluminescent devices, solar cell), power electronics (MOSFET, Schottky barrier diodes) and memory devices (resistive random access memory, spintronics application), sensing devices applications (nuclear radiation detector and gas sensor), deep UV transparent conductive oxide electrode, photocatalyst [93], [94]. γ-phase has a spinel structure that is important in ferromagnetic applications. γ-Ga_2O_3 with Mn, Fe , Cu content has been reported elsewhere and shows potential for use in optoelectronics and

ferromagnetic applications. For example, Qi Liu et al. studied the metastable γ phase in Ga_2O_3 thin films by Cu doping showing that the bandgap can be varied from 4.38 to 4.90 eV with stronger photoluminescence properties than undoped β-Ga_2O_3 [95]. Mn doped γ-Ga_2O_3 was fabricated by the Rong Huang et al. and demonstrated ferromagnetism at room temperature [43]. Yuanqi et al. showed Fe doped stabilized γ-Ga_2O_3 thin films with high room temperature saturation magnetization [49].

1.2 Crystal Structure of β-Ga_2O_3

Gallium oxide (Ga_2O_3) is an inorganic compound that has been reported to exist in five phases: α, β, γ, δ and ε. Table-1 [96] shows the crystal properties of the various phases in the Ga-O systems [97]. Among them β- Ga_2O_3 is the only stable crystalline phase at high temperature and this stable formation persists under cooling. In contrast, all other polymorphs are metastable and transform to the β form at sufficiently high temperatures [97]–[101]. X-ray diffraction studies shows that the crystal structure of β-Ga_2O_3 is monoclinic with space group C2/m [102], [96], [103].

Table 1.1. Solid phases in the Ga-O system [96].

Phase	Composition (at.% O)	Pearson symbol	Space group	Prototype	Lattice parameters (nm, deg)	Reference
α-Ga_2O_3†	60	*hR*30	$R\bar{3}c$	α-Al_2O_3	a = 0.49791(6) c = 1.3437(4)	27
β-Ga_2O_3	60	*mC*20	*C*2/*m*	β-Ga_2O_3	a = 1.2214(3) b = 0.30371(9) c = 0.57981(9) β = 103.83(2)	2
γ-Ga_2O_3†	60	*cF*56	$Fd\bar{3}m$	Al_2MgO_4	a = 0.822	30
δ-Ga_2O_3†	60	*cI*80	$Ia\bar{3}$	Tl_2O_3	a = 1.000	14
ε-Ga_2O_3†	60	*oP*40	$Pna2_1$	κ-Al_2O_3		14,15
Ga_2O†	33.3			Amorphous		8

†Metastable phase.

Figure-1.1. illustrates the crystal structure of the based-centered monoclinic structure with lattice parameters a=12.23 A°, b = 3.04 A°, c=8.80 A°, α = γ = 90° and β=103.8° (angle between lattice parameters a and c) [96],[8], [104].

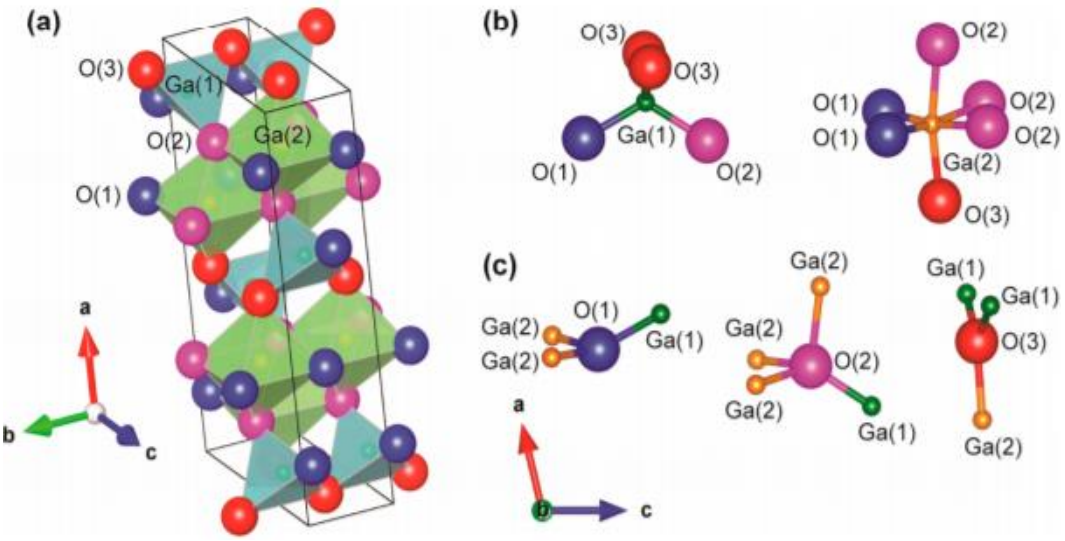

Figure 1.1. (a) Crystal structure of β- Ga_2O_3, showing two different Ga sites - tetrahedral (I) and octahedral (II), 3 fold and 4 coordinated O sites, and 3-fold coordinated, and open channels in b-direction [104].

The unit cell is made up of 8 Ga and 12 O atoms, containing four formula units fig. 1(a). Per crystallographic unit cell, there are four Ga_2O_3 units, each unit cell contains two inequivalent Ga sites and 3 inequivalent O sites. one-half of the Ga atoms belongs to tetrahedrally coordinated sites Ga(1), and other half in distorted octahedral coordination Ga(2), shown in fig. 1(b). Ga (1) is surrounded by 4 oxygen atoms, while Ga(2) surrounded by 6 oxygen atoms. Oxygen atoms reside in three nonequivalent highly distorted sites: O (1) and O(3) being tricoordinate and O(2) being four-coordinated demonstrated in fig. 1(c) . The calculated average interatomic distances in tetrahedral Ga-O is 1.83 A°, octahedral Ga-O is 2.00 A°, tetrahedron edge O-O is 3.02 A°, and octahedron edge O-O is 2.84 A° [102], [36],[21].

1.3 Crystal Structure of γ- Ga_2O_3

Among the several polymorphs well known for Ga_2O_3 are α, β, γ, δ and ε. These phases are part of different space groups having different coordination number(CN). γ-Ga_2O_3 has recently come to the forefront for scientific research because of its applications for electronic and optical devices. The crystal structure of γ- Ga_2O_3 resembles that of γ-Al_2O_3, a cubic, cation-deficient spinel with partial occupancy of both octahedral and tetrahedral sites. The lattice parameter of a cubic defective spinel phase is around a=0.822 nm and corresponds to the Fd3m space group. It has the same coordination number as β-Ga_2O_3 (CN=4, and CN=6 sites) [43]. In order to be a spinel structure the original molecular formula for the spinel phase is AB_2O_4, where the unit cell consists of 32 cubic closed packed oxygen ions [105], [106]. Figure 1.2 shows the crystal structure of γ- $Ga_{24}O_{32}$, containing 8 tetrahedrons (4 oxygen bonded single Ga atom) and 16 octahedrons (one Ga atom surrounded by 6 oxygen atom). It's two nonequivalent sites named Ga_T and Ga_O are tetrahedrally and octahedrally coordinated, respectively, in the unit cell [107],[49].

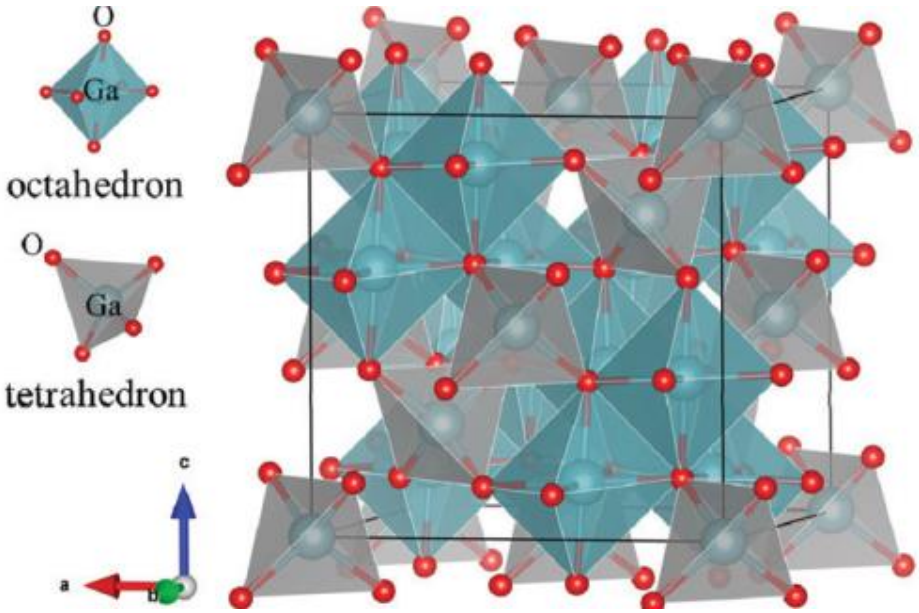

Figure 1.2. Crystal structure of γ-gallium oxide containing two octahedron and tetrahedron site [49].

1.4 Crystal Structure of α, δ and ε

Along with β, γ- Ga_2O_3 other polymorphs α, δ and ε phases are interesting because of their unique material properties. For example, the ε phase is particularly promising due to its simpler epitaxial growth conditions and higher symmetry with respect to the monoclinic β phase. In addition, it shows a favorable lattice matching with a sapphire substrate and with other hexagonal or pseudohexagonal substrates [108]–[110]. There have been theoretical studies to determine the crystal structure and formation energy of the ε phase[111]. Though some theoretical papers and experimental reports suggest that the ε phase is orthorhombic [112], [111], [113], [112], other experimental studies shows a hexagonal structure [108]–[110], [113], [114]. Although, there is debate between experiment and theoretical study of metastable ε phase, it has some interesting properties for materials applications, for example, wide bandgap applications, ferroelectricity, UV sensor, and gate oxide [115], [116].

α - Ga_2O_3 is also a metastable phase of Ga_2O_3 but has a wider bandgap (5.1-5.3 eV) than the β phase [117], [118]. The structure of α phase analogous to α-Al_2O_3 (corundum) [114], with lattice constant a=0.49825, c=1.3433nm, while α-Al_2O_3 are a=0.4765, c=1.3001nm[119].

The δ-phase is the least reported in the scientific community. δ-phase was first reported by Roy et al. and was proposed to be a bixbyite structure, which known as C-type rare earth and obeys the body centered cubic unit cell of $Ia\overline{3}$ space group analogous to In_2O_3 and Mn_2O_3 etc.[120]. Later, nano structured δ-phase were synthesized from $Ga(NO_3)H_2O$ by Aditya Sharma et al. [121], which also confirm this corresponds to $Ia\overline{3}$ space group. However, to the best of our knowledge, we did find any other report on the growth of thin film δ-phase.

1.5 Materials Properties of Ga_2O_3

Among all polytypes the most stable crystallizes into the β- Ga_2O_3 gallia structure belonging to the monoclinic system , whereas other polytypes are metastable [38].
It was expected that the crystal structure of Ga_2O_3 is similar to Al_2O_3 owing to resemblance of ions between the Al and Ga. In fact, α-Ga_2O_3 (unstable) has a typical likewise corundum structure as the natural state of Al_2O_3 (stable). Roy et.al [120] studied the polymorphism of Ga_2O_3 by various heat treatments and the results are summarized in the following figure 1.3. They used crystalline gallia gel as the starting substance prepared from aqueous solution. Crystalline hydrated gallia first converts to α-Ga_2O_3 then to GaO_2H, with diaspore structure as well as γ- Ga_2O_3 at specific aging condition. The most stable form of β- Ga_2O_3 was formed when any other form of Ga_2O_3 or its hydrates are annealed in air above 1000^o C or hydrothermally heating above 300^o C at any H_2O

pressure. They also demonstrated that a substance prepared by metal nitric acid and subsequent heating to 250° C for evaporation and later overnight heating at 200° C transforms it to δ- Ga_2O_3. Similarly, when δ- Ga_2O_3 is heated under different thermal conditions ε- Ga_2O_3 appears. Conversion of $Ga_{2-x}Al_xO_3$ to β- Ga_2O_3 occurs only when x<1.3.

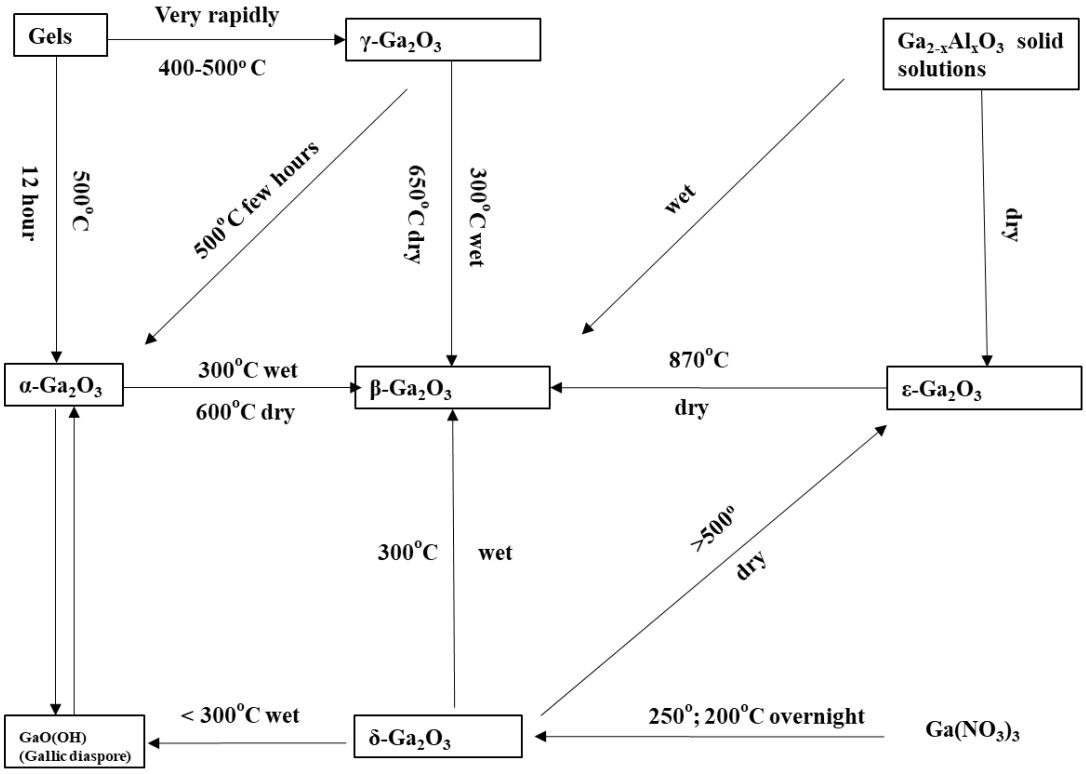

Figure 1.3. Transformation relationship of different Gallia and its hydrates under different thermodynamic conditions [120].

Later a similar study was performed and reported elsewhere[121], which shows transformation of Ga_2O_3 phases at different temperatures synthesized from $Ga(NO_3)_2.xH_2O$ chemical compound as shown in following figure.

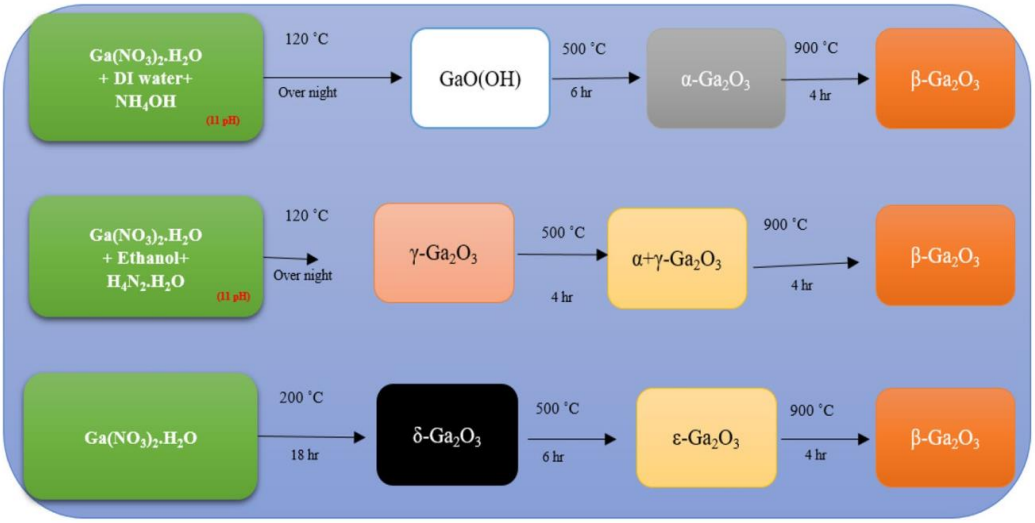

Figure 1.4. Schematic diagram of synthesizing Ga_2O_3 phases in three ways [121].

The reported bandgap of β- Ga_2O_3 is 4.5- 4.9 eV [104], [122], [123]. Pure Ga_2O_3 is an insulator but can show significant n-type conductivity even without doping. This conductivity is assumed to be due to oxygen vacancies, but this assumption not yet been verified. Varley et al. [124] showed that oxygen vacancies create deep donor states (1eV), i.e. requires high activation energy and some other theory attribute the observed n-type conductivity as being due to oxygen vacancies. Instead, it was proposed that several shallow donor impurities including Si and monoatomic hydrogen are responsible for the n-type conduction [21],[51]. Besides, doping with Sn, Si, and Ge makes it an n-type material. Sn and Si atoms work as shallow donors with small activation energies. Sn prefers the octahedral coordination of the Ga (2) site, while Si and Ge prefer the tetrahedral coordination of the Ga (1) site. Cl and F both prefer the threefold coordination of the O (1) site [51]. Carrier density can be controlled in the wide range of 10^{15}-10^{19} cm^{-3} [125], [78], [8]. Technology based on n-type doping is therefore relatively easy and mostly successful. In contrast, p-type doping is challenging because of its extreme wide

bandgap; high formation energy of point defects that produce holes, i.e., a shallow acceptor level with respect to the host valence band; low energy of hole killer native defect like anion vacancies and cation interstitials; as well as of lack of suitable dopant [126]. In addition, first principle calculation on the electronic structure of β- Ga_2O_3 demonstrates the conduction band minimum is almost isotropic with extremely light effective mass for electrons, whereas valence bands close to the band edge are relatively flat in curvature, which leads high effective mass for holes at the valence band minimum [127]. To the best of our knowledge there has been no report on effective hole conduction in Ga_2O_3. As a potential p-type dopant, divalent ions, for example- Mg^{2+} [128], Zn^{2+} [129], [130], and Cu^{2+} [130],[64], which substitute into trivalent Ga^{3+} in β- Ga_2O_3 have been explored, but without considerable success. It would be major hindrance for Ga_2O_3 technology if p-type conduction is not possible, since without p-type conductivity, p-n junctions are not possible. Although, high electrical breakdown voltage can be achieved for majority carrier devices, low on-resistance is difficult to obtain without minority carriers [21]. While this is a present limitation, technical innovations incorporating hetero p-n junction may be possible. The mobility (μ) of electrons in Ga_2O_3 was estimated to be 300cm^2/Vs for the typical electron concentration (n) range of 10^{15}-10^{16} cm^{-3} and expected electric breakdown voltage of 8 MV cm^{-1} [131], [77]. Figure 1.5 demonstrates the dependency of on resistance with breakdown voltage, and bandgap with respect to electric breakdown voltage. When Ga_2O_3 is examined using different figure-of-merit methods (FOM), such as the most commonly used, Baliga FOM, Ga_2O_3 has significant advantages over other wide bandgap semiconductors for high power applications [8], [21]. Thermal conductivity of β- Ga_2O_3 is also highly anisotropic at room temperature,

the [100] direction has the lowest conductivity of 10.9.0 ±1.0 W/mK, in contrast along with [010] direction has the highest value of 27.0 ±2.0 W/mK [132]. Table 1.3 summarizes major physical and semiconducting properties of β- Ga_2O_3 in comparison with other relevant semiconductors.

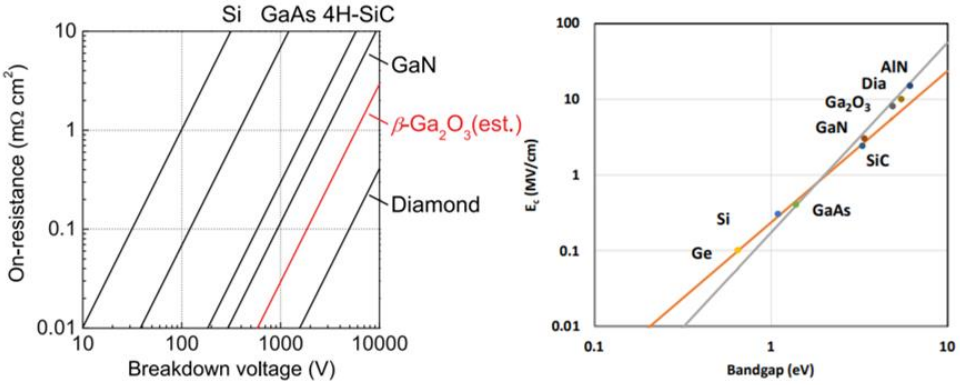

Figure 1.5. (a) Calculated theoretical performance breakdown voltage with respect to on-resistance and other semiconductor power devices [8], and (b) bandgap versus breakdown voltage for direct and indirect bandgap semiconductor [36].

Table 1.2. Properties of β- Ga_2O_3 and comparison with other currently leading semiconductor materials ([24]).

TABLE II. Properties of β-Ga_2O_3 relative to other more commonly used semiconductors. We also show some of the common figures-of-merit used to judge the suitability or potential of these materials for various high temperature, high voltage or power switching applications.

Materials parameters	Si	GaAs	4H-SiC	GaN	Diamond	β-Ga_2O_3	Comments
Bandgap, E_g (eV)	1.1	1.43	3.25	3.4	5.5	4.85	Bandgap of Ga_2O_3 reported in range 4.6–4.9 eV
Dielectric constant, ε	11.8	12.9	9.7	9	5.5	10	
Breakdown field, E_C (MV/cm)	0.3	0.4	2.5	3.3	10	8	Experimental values for Ga_2O_3 have reached ~0.5 times the theoretical maximum
Electron mobility, μ (cm^2/Vs)	1480	8400	1000	1250	2000	300	
Saturation velocity, v_s (10^7 cm/s)	1	1.2	2	2.5	1	1.8-2	1.8 ⟨0 0 1⟩ and ⟨0 1 0⟩, 2.0 ⟨0 1 0⟩
Thermal conductivity λ (W/cm K)	1.5	0.5	4.9	2.3	20	0.1–0.3	0.13 ⟨1 0 0⟩, 0.23 ⟨0 1 0⟩
Figures of merit relative to Si							
Johnson = $E_c^2 \cdot V_s^2/4\pi^2$	1	1.8	278	1089	1110	2844	Power-frequency capability
Baliga = $\varepsilon \cdot \mu \cdot E_c^3$	1	14.7	317	846	24 660	3214	Specific on-resistance in (vertical) drift region
Combined = $\lambda \cdot \varepsilon \cdot \mu \cdot V_s \cdot E_c^2$	1	3.7	248.6	353.8	9331	37	Combined power/frequency/voltage
Baliga high frequency = $\mu \cdot E_c^2$	1	10.1	46.3	100.8	1501	142.2	Measure of switching losses
Keyes = $\lambda \cdot [(c \cdot V_s)/(4\pi \cdot \varepsilon)]^{1/2}$	1	0.3	3.6	1.8	41.5	0.2	Thermal capability for power density/speed
Huang HCAFOM, $\varepsilon \mu^{0.5} E_C^2$	1	5	48	85	619	279	Huang chip area manufacturing FOM

On the other hand, metastable phases are poorly studied, and their properties are not completely known. Even though there are few reports on α- Ga_2O_3, δ- Ga_2O_3 and ε- Ga_2O_3, γ- Ga_2O_3, they have some interesting properties that may be useful for device applications. In addition, they have ultrawide bandgap which is close to β- Ga_2O_3. For example, recently structures utilizing quantum dots with visible blue green light emission property were studied by Tao Chen et al. [133]. They prepared the quantum dots by solvolysis of $GaCl_3$ in N, N-dimethylformamide and observed light emission by the naked eye. Recently, Yuanqi Huang et al.[49] studied Fe doped γ- Ga_2O_3 , and measured room temperature ferromagnetism. However, the origin of the ferromagnetism in spinel structure γ- Ga_2O_3 is not clearly understood due to there being few reports in the literature.

2. GROWTH OF THIN FILMS USING PLD

2.1 Overview

The advantage of β- Ga_2O_3 compared to the other large optical gap semiconductors such as GaN, AlN, diamond and SiC, is the availability of economically high purity monocrystalline substrates. Ga_2O_3 substrates can be fabricated with low cost techniques, such as the melt growth methods (floating zone, Czochralski, edge-defined film-fed growth). Researchers have been using several physical and chemical techniques to fabricate β-Ga_2O_3 thin films including pulsed laser deposition (PLD), plasma enhanced atomic layer deposition (PEALD), spray pyrolysis, chemical vapor deposition (CVD), sol-gel method, halide vapor phase epitaxy (HPVE), and plasma assisted molecular beam epitaxy (PAMBE) [21].

This research is solely based on the PLD technique, a handy technique for thin film deposition owing to several vital factors, such as the growth environment, the controlling substrate temperature, deposition rate, wide range of materials deposition and doping, and controlling of the plume geometry. These factors can be controlled individually to alter film quality. Firstly, it offers growth at different temperatures to have better crystallinity or desired properties. F.-P. Yu et al. [134] investigated the deposition of monoclinic Ga_2O_3 thin films on sapphire substrate at various substrate temperatures ranging from 400-1000^oC using PLD. By altering the substrate temperature, they were able to demonstrate a single crystalline phase at 800^oC with higher crystal quality than at lower temperatures. Lauren M. Garten et al. [135] showed there is a strong temperature dependence on the electronic properties, morphology, and phase formation of β-Ga_2O_3 from 350-550 °C. Secondly, the growth ambient can be significantly changed by

providing high purity oxygen (O_2) and/or argon (Ar) at varying pressures into the chamber. Gas flow is introduced and controlled through a mass flow controller (MFC). Several earlier reports [134], [36] studied the dependence of temperature and oxygen pressure on the crystal quality of Ga_2O_3.

Doping of the oxide films allows for a change of its properties from insulator to semiconductor. Stefan Muller et al. [136] investigated the conductivity of Si-doped β-Ga_2O_3 at temperatures of 400 and 650^{o}C and oxygen pressures ranging from 3×10^{-4} - 2.4×10^{-2} mbar prepared by PLD on sapphire substrates. They observed that at high oxygen partial pressure the film consisted of multiple crystalline phases but by decreasing the pressure (below 10^{-3} mbar) they were able to obtain $(\bar{2}01)$ oriented single-phase thin films. They found that with oxygen pressure below 10^{-3} mbar, there is a slight increase in the film thickness, which can be attributed to the reduced interaction between the deposited species and the background gas, resulting in a higher net particle flux impinging on the substrate. However, with the pressure range 10^{-3} to 1.2×10^{-2} mbar there is a rapid increase in the thickness resulting in a polycrystalline film due to the increasing number of bonding site compared to single phase epitaxial growth (oxygen pressure $\leq10^{-3}$ mbar). They also showed that the conductivity depends on the oxygen partial pressure, which provided an insight for optimizing the performance of devices such as rectifiers, photodetectors and transistor based on the roughness, crystallinity and conductivity of the β-Ga_2O_3 thin films. Furthermore, during growth using PLD, the laser parameters- repetition rate, pulse duration, fluence, sample to target distance can be varied to optimize the plume geometry and the resultant film properties.

2.2 Pulsed Laser Deposition

Pulsed laser deposition (PLD) is a versatile method for the deposition of high-quality functional materials. This represents one kind of physical vapor deposition (PVD) process carried out in vacuum that can deposit a wide range of thin film materials, including multicomponent, heterostructures and complex oxide films. It was first discovered by researchers at Bell Labs to deposit high temperature superconducting materials [137]. A schematic diagram of PLD system is presented in figure 2.1.

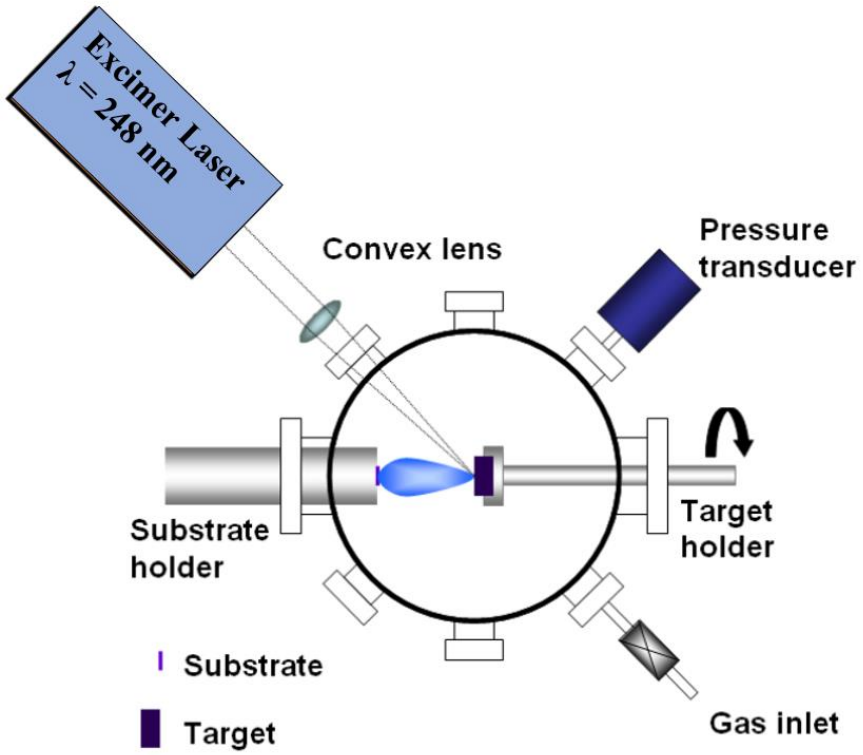

Figure 2.1. Schematic diagram of pulse laser deposition system [138].

The primary part of this system is a coherent laser source having wavelength 248nm (KrF excimer laser) or 308nm (XeCl laser). The laser beam is focused onto a

target of the material to be deposited using lens and mirrors. High energy laser pulses ablate the target material and create a plasma plume; this ablation plume provides the material flux for film growth. Unlike electrons or ions, transport and manipulation of laser beam are much easier, as laser interactions with the gaseous phase is relative weak. Principally, the ablation species or plume is comprised of energetic atomic, diatomic ions, clusters, molecules, and species of low mass. PLD has been able to capitalize on the technological advancements realized such as a significantly improved excimer laser capability in terms of power, stability and reliability and the continual development of new shorter pulse length lasers with high power which has been important for PLD applications [137],[139].

There are some interesting features that makes PLD versatile. First, a unique feature of PLD is the stoichiometric preservation of composition from the target to the substrate. This is because the absorption of a short laser energy pulse by a small part of target produces the ablated material plume. Therefore, this removes the requirement to control the evaporation rate of individual elements of a compound as the stoichiometry of any multicomponent film is same as the target. Secondly, PLD has the capability of introducing background reactive gases such as nitrogen, oxygen, or inert gas such as argon etc. for controlling film quality. Indeed, dynamic range of growth pressure during deposition is the largest in contrast to virtually any deposition system. This also allows for the flexibility to adjust for a broad range of gas pressures in the chamber to further optimize the growth process. Thirdly, the deposition of heterostructures using programmable target rotation system is straightforward to accomplish [140] . Furthermore, substrate temperature can also be varied from room temperature to 1200^{o} C.

The crucial components of PLD system are a high vacuum growth chamber, load-lock, pumping systems, wafer transport system, substrate manipulator, optics, and laser.

Possible growth chamber geometries are usually spherical or cylindrical. The growth chamber used in this research can handle substrates up to 2 inches in diameter. It features a differentially pumped reflection high energy electron diffraction (RHEED) system that can be used to monitor the surface, gas inlets, pressure gauges, viewpoints, ports for pumping and special viewport through which the laser beam enters the chamber onto the target, substrate holder, heater, and targets. The base pressure of chamber is usually maintained at 10^{-9} with the use of turbo molecular pump.

The load lock chamber separates the growth chamber by manual gate valve for sample loading and unloading purposes without breaking the vacuum of main chamber. The load lock chamber consists of a small vacuum chamber with turbo pumping, ion gauge, view ports and magnetically coupled manual transfer arm assembly.

The substrate manipulator consists of a substrate holder and heater assembly as shown in figure 2.2. It can hold substrates up to 2 inches in diameter. To maintain the temperature uniformity the radiatively heated substrate is located just below the heater and rotated during growth. The temperature of the substrate can reach just below 1200^{o} C based on the heater specifications. The substrate manipulator can be moved vertically as well as rotated 360^{o} . The optimal target and substrate distance typically depend on the energy delivered to the target and the material to be grown.

Figure 2.2. PLD substrate heater.

In a PLD system, to guide and focus the laser light into the deposition chamber, special lens and mirrors should be used. The incident window of the chamber should be transparent to the laser beam; usually fused quartz is the preferred material for the window due to the short wavelength. The alignment mirror and lens also need to have proper specifications to work with energetic nano-second short pulses of UV irradiation. In addition, target, plume geometry, substrate rotation speed, as well as distance from the substrate to target plays a substantial rule to achieve high quality film deposition. Typically, depending on the geometry, the substrate to target distance is 2 to 5 cm.

The basic arrangement of the excimer laser includes capacitors, inductor coils and electrodes. A typical layout of an electric discharge laser model is shown in following figure. In this system, the storage capacitor is charged to high voltage around 40 kV, after which a thyratron switch is closed to transfer energy to the peaking capacitors in a

very short period (approximately 100ns). When the peaking capacitor is sufficiently charged the energy is transferred to the discharge medium with a time duration of 20~50 ns.

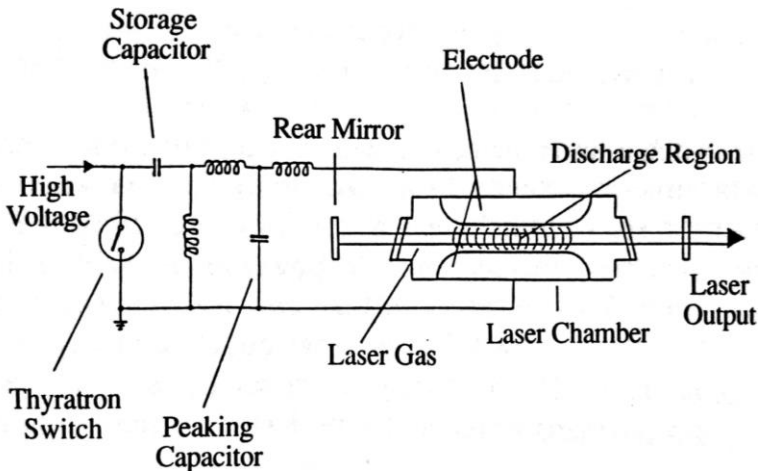

Figure 2.3. Schematic diagram of an excimer laser [140].

In addition, the target preparation plays an important role to achieve high quality films, as the physical properties of the target has an impact on the surface morphology of the deposited films. To avoid droplets on the film surface, a high-density target should be prepared. In addition, to have a uniform target erosion and consumption the most common practice to rotate the target

Fig. 2.4 shows the PLD system which was used to carry on this research. In this system, the KrF excimer laser was used with a wavelength of 248nm and a nominal pulse duration of 25ns. The laser repetition rate and pulse energy were 5Hz and 250mJ (energy density 2-3 J/cm^2 on the target surface) per pulse, respectively.

Figure 2.4. Installed PLD system at Prof. Ravi Droopad's lab, Texas State University.

2.3 Thin Film Growth Modes

The growth process involves complex mechanisms of nucleation, thermodynamics, surface energies of films and substrate and film substrate interface energy. The formation (nucleation) of a thin film of atoms on a substrate involves several processes as shown in following figure 2.5. The rate of arriving atoms depends on the deposition parameters. These adatoms can diffuse across the substrate or film surface and encounter other mobile adatoms to form clusters or to attach to pre-existing thin film atom clusters. Adatoms can also re-evaporate from the substrate or detach from a cluster. The stable clusters will have a critical size that depends on deposition parameters including temperature and bonding energy to the substrate or thin film. The formation of

stable clusters is called the nucleation process which depends on the total free energy of the materials system.

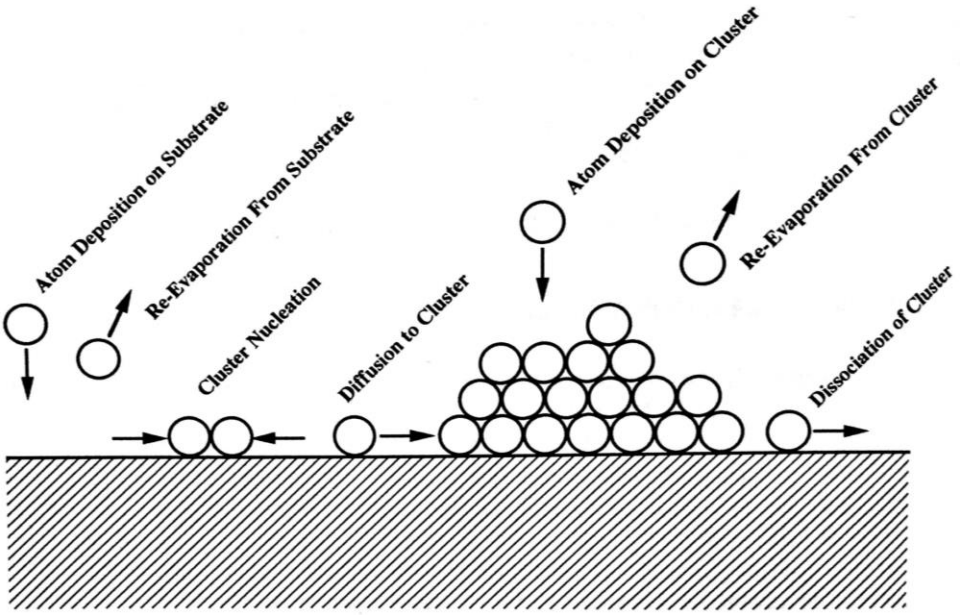

Figure 2.5. Schematic representation of atomic processes in the nucleation of three dimensional clusters of deposited atoms on substrate [140].

There are several possible thin film growth modes depending on the surface energy of the thin film material, the interface energy between the thin film material and substrate, and the lattice mismatch between substrate and thin film. Three main thin films growth mechanisms are observed- (a) Frank-van der Merve growth mode (layer-by-layer); (b) Volmer-Weber growth mode (island); and (c) Stranski-Krastanov (layer-by-layer followed by--island) growth mode, shown in below figure 2.6.

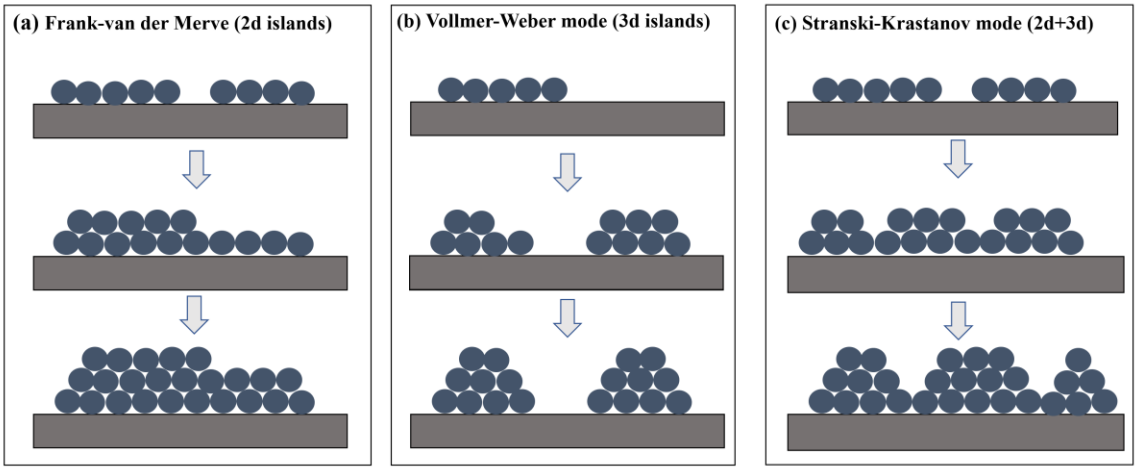

Figure 2.6. Growth modes of thin films: (a) Frank-van der Merve growth mode (Layer by layer), (b) Volmer-Weber growth mode (Island) and (c) Stranski-Krastanov growth mode (Layer-by-Layer followed by Island).

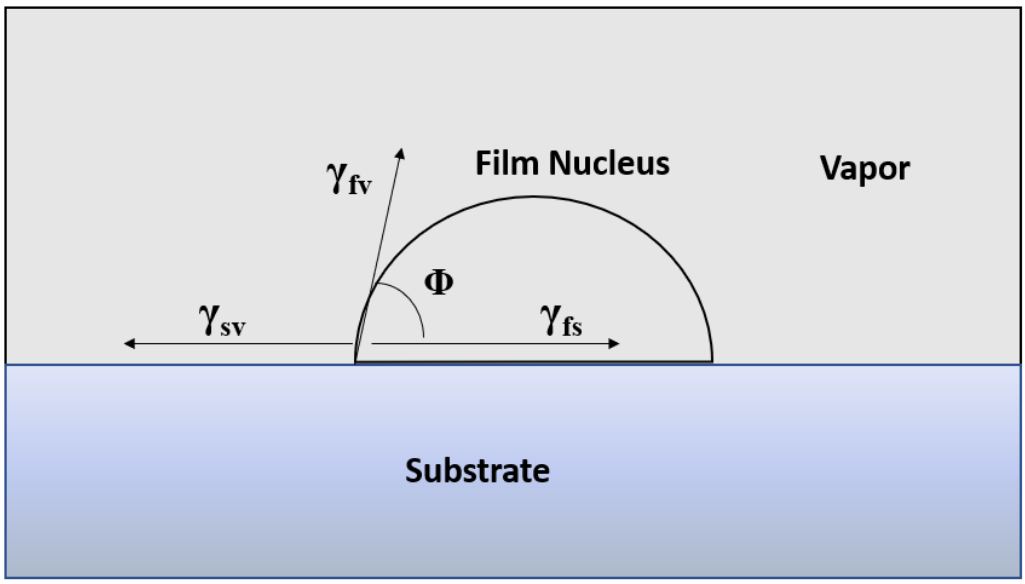

Figure 2.7. A schematic diagram of surface tension during growth [141], [142].

The nucleation and growth process can be described by the Young's equation (1) of capillarity droplet theory of heterogeneous nucleation[141], [143]–[145] . For a thin

film growth process, the surface tension or interfacial tension γ, represents the work required to build a surface of unit area.

$$\gamma_{sv} = \gamma_{sf} + \gamma_{fv} * cos\phi \quad (1)$$

where, s, f, v stands for substrate, film, and vapor respectively and ϕ is the wetting angle or contact angle. When the total free energy of the film surface (γ_{fv}) and the interface (γ_{sf}) is less than the free energy of the substrate surface (γ_{sv}), then layer by layer or 2D growth takes place [146]. In contrast, for island growth, i.e. a wetting angle θ>0, the bonding between substrate and film is not sturdy, the interfacial free energy will be higher. For such case the total free energy of the film surface and interface will be greater than the substrate free energy, which leads to island or a 3D type growth mode [147]. In case of Stranski-Kranstanov growth, since $\gamma_{sv} \geq \gamma_{sf} + \gamma_{fv}$ is satisfied the first layers growth in layer by layer mode which is then followed by an island mode growth process due to buildup of strain energy from the lattice mismatch between the thin film and the substrate. This strain is relaxed by the formation of islands which serves to reduce the total energy of the system. Combination of layer by layer and island modes mechanism is known as Stranski-Krastinov growth [148], [149].

2.4 Target Preparation

For thin film deposition using the PLD technique, it is essential to prepare a target of the material that is to be deposited. For this purpose, the oxide target was prepared using a standard solid-state reaction or ceramic sintering method. First, highly pure oxide powders were taken as starting materials, and were mixed according to the proper weight/atomic ratio for the desired mole fraction in the case of alloys. To mix the powder homogenously, an ultrasonic ball milling was used for 30-40 minutes. Later, the mixed

powder was pressed for 24 hours at 400^{o}C and 15000 lb./in.^{2} pressure in a hydraulic press machine to create 1-inch ceramic disks that have the dimensions for use as the sources in the PLD system. Since the solid mixture does not usually react together at room temperature the ceramic disk was then sintered in a high temperature furnace at 1000-1200^{o} C for 12-20 hours in an argon environment. Density, porosity, and grain size of the ceramic pellets are dependent on the sintering process. Afterwards, the targets were polished and evaluated using XRD measurement before finally loaded for deposition into the PLD chamber.

3. CHARACTERIZATION METHODS

3.1 Introduction

Characterization is essential for evaluating thin films for varieties applications. In this study, crystalline properties and phases were analyzed on a Rigaku SmartLab x-ray diffractometer. Cu-Kα radiation was passed through a Ge (220) monochromatic crystal to probe the materials. The diffracted light intensity distribution was collected using a high energy resolution detector HyPix-3000. Surface topology and roughness were investigated using a Bruker Dimension Icon AFM system. Optical properties (bandgap, refractive index) and roughness were examined using a J.A Woollam M-2000 ellipsometer. Optical transmission of thin films was studied using a UV-2600 Shimadzu, UV-vis spectrometer. A Scienta Omicron X-ray photo electron spectroscopy (XPS) system was used to analyze surface states and chemical composition of the samples. Energy dispersive x-ray photoelectrons spectroscopy (EDS) was used to determine the atomic percentage of each element in the films. Finally, magnetic properties were probed using vibrating sample magnetometer on MicroSense system.

3.2 X-Ray Diffraction

X-ray diffraction (XRD) is a fundamental nondestructive technique that is used to probe structural properties– lattice parameters, crystalline phases, unit cell dimensions, alloy compositions, defects, etc. In this process, high energy x-ray radiation hit the probing materials and is scattered in all directions. Under normal circumstances, x-rays scattered by atomic planes interfere destructively and no x-ray intensity comes out from the materials. However, in special directions constructive interference occurs resulting in an intense beam of diffracted x-rays that can be detected at certain angles. By analyzing

the beams diffracted from a sample, the underlying sample's crystal properties can be obtained. In a crystal, constructive and destructive interference can be determined from the Bragg's law (equation 1), which is explained in figure 3.1.

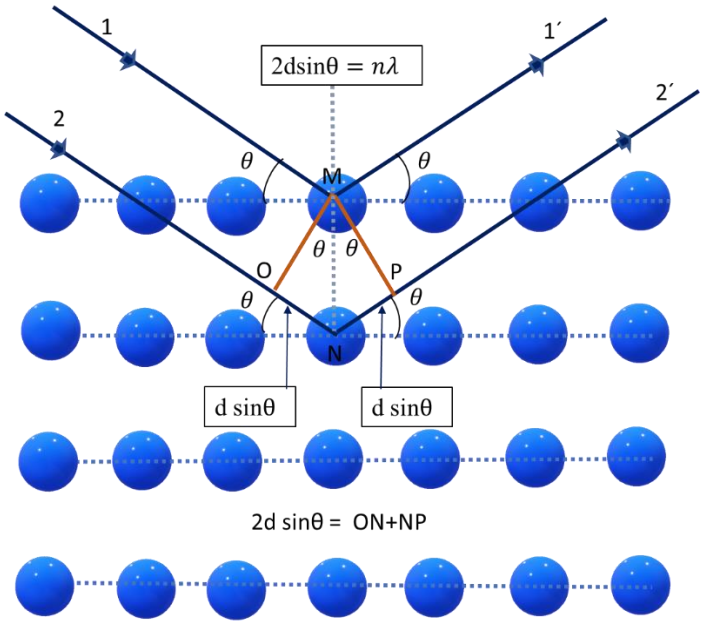

Figure 3.1. Schematic diagram of demonstrating Bragg's law.

In the figure, line 1 and 2 represent the incident rays and line 1' and 2' represent the diffracted rays from the crystal structure. The condition for constructive interference is:

$$2d\sin\theta = n\lambda \qquad (2)$$

Here, d is the lattice spacing between diffracting planes, θ is the incident angle, λ is the X-ray's wavelength, n is an integer that defines the order of diffraction. A crystal is basically a periodic arrangement of atoms. A parallel highly monochromatic x-ray beam incident on the crystal array at an angle θ is scattered by the atoms in all direction. As the diffracted rays have path differences, constructive interference occurs only when two rays

satisfy the Bragg's condition (equation), with n being an integer representing a multiple angle at which constructive interference can occur. Rewriting the Bragg's law, we get again:

$$2d_{hkl}\sin\theta = n\lambda \quad (3)$$

Where h, k, l are the Miller indices and d_{hkl} is the interplanar distance of plane (hkl). In case of a cubic lattice, the lattice parameter a = b = c then,

$$1/d_{hkl}^2 = (h^2 + k^2 + l^2)/a^2 \quad (4)$$

Using Bragg's equation,

$$\sin^2\theta_{hkl} = (\lambda^2/4a^2)\,(h^2 + k^2 + l^2) \quad (5)$$

In above equation, the sum $(h^2 + k^2 + l^2)$ is always an integer while $\frac{\lambda^2}{4a^2}$ is a constant for any pattern. The equation further suggests that for a cubic crystal, the diffraction takes place at all possible values of Bragg's angle from the (hkl) planes.

In this study, all thin film measurements were carried out on a Rigaku Smart-Lab X-ray diffractometer operating at 40kV, 44mA with a Cu-Kα source having a wavelength λ = 1.540562 Å. Figure 3.2 shows the X-ray diffraction measurement system.

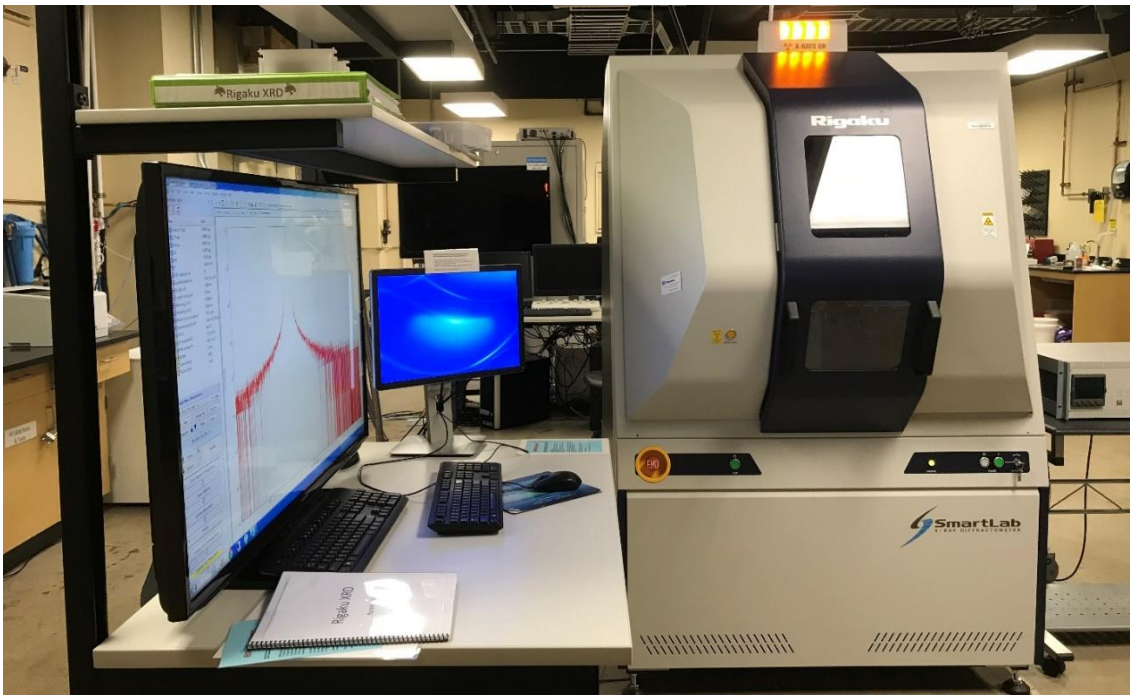

Figure 3.2. Rigaku Smart-Lab XRD system at Texas State University.

3.3 Ellipsometry

Ellipsometry is one of the most popular non-destructive experimental techniques that does not require sample preparation or a special measurement environment for determining the thickness, roughness, and optical properties (refractive index, extinction coefficient) of a thin film. Ellipsometry can thus measure optical constants, as well as thicknesses ranging from 0.1 nm to 0.01 mm with a high degree of accuracy. It is often used in the development and manufacturing process of semiconductor devices, flat panel displays, protective layers, biological and medical coating, and optical coating stacks as it is a non-contact technique that reduces sample contamination issues. The technique uses polarized light which undergoes changes in polarization upon reflection of light from the sample. The change in polarization is characteristic of the optical properties of the sample. Hence information about the material can be obtained by analyzing the reflected

light. Ellipsometry does not measure optical constants or thickness directly but rather a change in polarization expressed as ψ (relative amplitude change) and Δ (relative phase change). These parameters represent the differential changes in amplitude and phase, respectively, experienced upon reflection by the perpendicular and parallel components of the polarized light relative to the plane of incidence [150], [151]. With light obliquely reflected from a sample the incident and reflected beams define a plane of incidence. Light with its electric field vector oscillating in the plane of incidence is called *p* polarized light, and light with the electric field vector oscillating perpendicular to the plane of incidence is called *s* polarized light. The enabling principle of ellipsometry is that *p* and *s* polarized light reflect differently i.e. $R_p \neq R_s$. Hence ellipsometry measures the complex reflectivity ratio of *s* and *p* polarized light expressed in terms of ψ and Δ parameters.

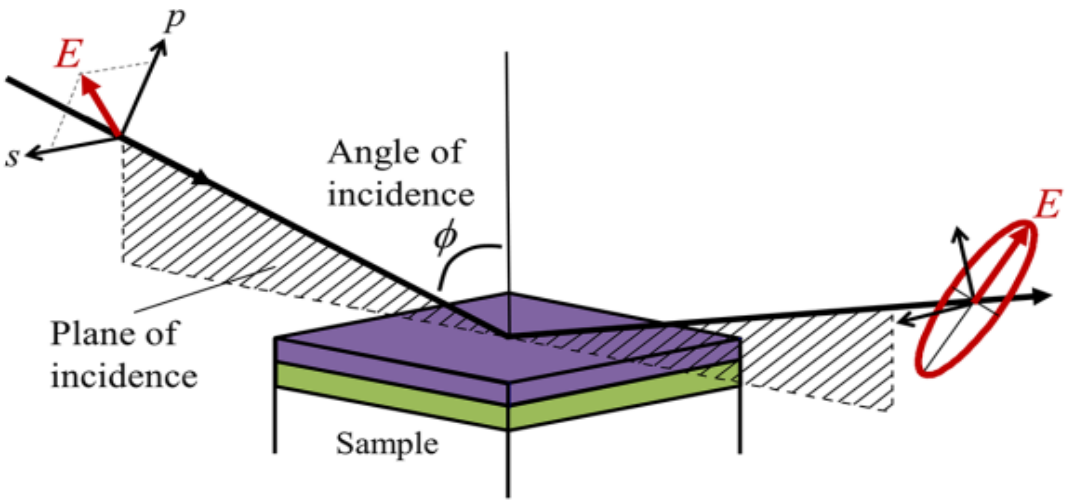

Figure 3.3. Ellipsometry measurement using linearly polarized light with s and p components. The interaction with the sample leads to different amplitudes and phase changes upon reflection [151].

$$R_p/R_s = \tan(\Psi) \times e^{i\Delta} \quad (6)$$

$$\text{where } \tan(\Psi) = \frac{(E_p/E_s)_{\text{Reflected}}}{(E_p/E_s)_{\text{Incident}}} \text{ and } \Delta = \Delta_p - \Delta_s$$

$\tan(\psi)$ is a measure of the change of absolute value of R_s and R_p and it is a very reproducible measuring method, whereas, Δ is the phase difference between *p* and *s* direction of the complex Fresnel reflection coefficients (R_p, R_s) for a given wavelength and angle of incidence, and E_p and E_s are electric field of p and s polarized light. To analyze multiple layers, the materials must be transparent or semi-transparent [152]. However, working with transparent substrates can cause unwanted reflections, such as from the back surface. In most cases the substrate is thick enough to spatially separate the reflected light beams from the front and back surfaces, but for thin glass or plastic sheets the two beams can overlap, giving incorrect information. So, it is essential to remove backside reflections. This can be done by roughing the backside of the substrate or putting black absorbing tape that scatters the light as demonstrated in figure 3.4.

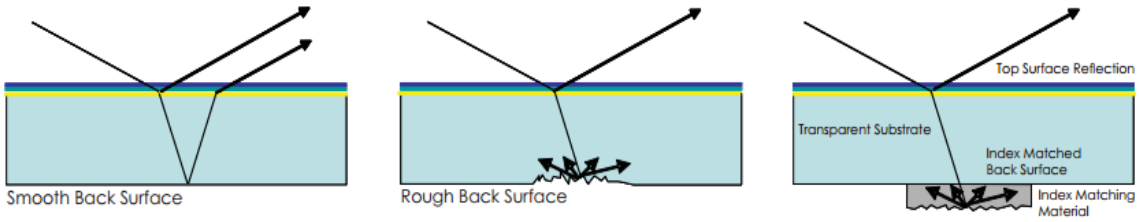

Figure 3.4. Unwanted reflections from the back surface suppressed by roughening or index matching [153].

In this study, an M-2000 Woollam spectroscopic ellipsometer was used to probe the samples. With this spectroscopic measurement, optical properties can be explored

over the photon energy range from 6eV to 1.2eV. Measurements can be done for different angles of incidence (55~90^{o}).

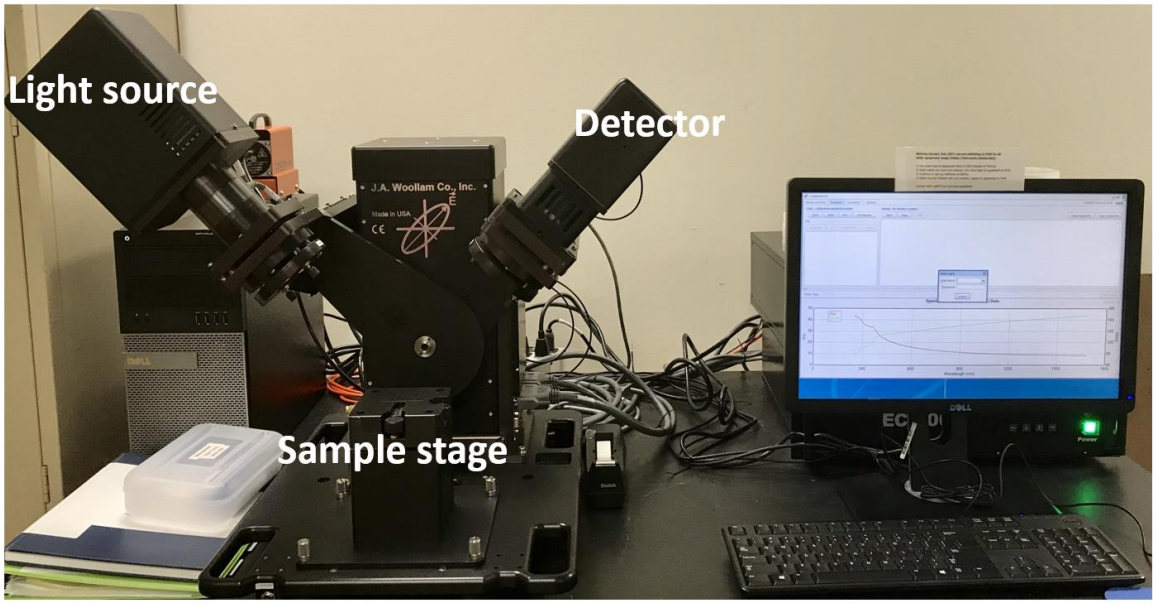

Figure 3.5. M-2000 J. A. Woollam spectroscopic ellipsometry system.

3.4 X-Ray Photo-electron Spectroscopy

X-ray photoelectron spectroscopy (XPS) is a powerful nondestructive method widely used to determine elemental composition, chemical formula (empirical nature), and chemical or electronic state of the elements that make up the thin film. It is highly dependent on the electronic state of the elements. The principle of this technique is based on the photoelectric effect, where a monochromatic x-ray beam, impinges upon the sample surface and ejects core shell electrons from the sample atoms. These emitted electrons are called photoelectrons that get detected producing a spectrum of binding energy versus number of electrons per unit time. Since each element has a unique set of core levels, the emitted electron's KE is used as a fingerprint of that element. The kinetic

energy (KE) of the electron which is coming out from the sample will be high if the binding energy (BE) is low and vice versa. The emitted electrons can also be Auger electrons, which represent a different process for the emission of a photoelectron. Once an electron from a higher shell (L shell) falls to fill core level vacancy (K shell) created by the x-ray beam another electron from the L shell absorbs the energy difference, and enough absorbed energy can cause an electron to be emitted as an auger electron. In this case the photoelectron is referred to a KLL Auger electron as illustrated in figure 3.6. The kinetic energy of the emitted photoelectron during the photoemission process is expressed by following equation.

$$K.E = h\nu - (BE - \phi) \qquad (7)$$

where, K.E is the kinetic energy of the ejected electron, BE is the binding energy of the shell, hv is the x-ray photon energy and Φ is the instrument's work function.

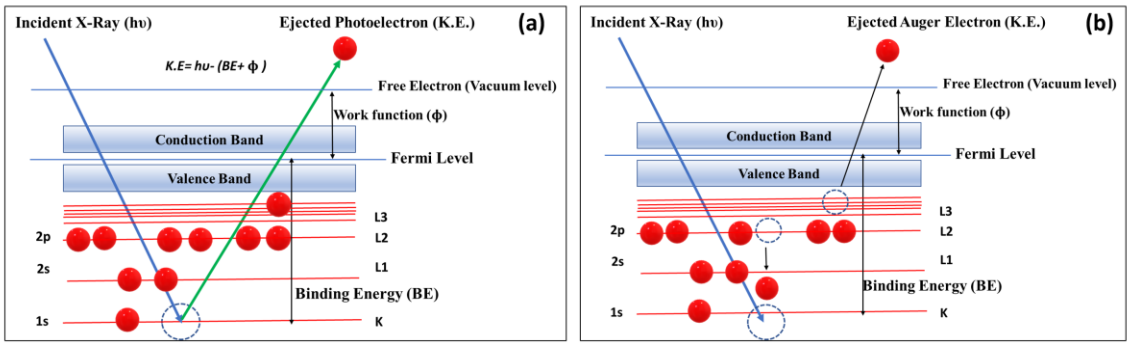

Figure 3.6. A representation of (a) photoelectron emission and (b) Auger relaxation effect [154].

Carbon is the most prevalent element in nature, and most samples that have been exposed to the atmosphere will have a detectable quantity of adventitious carbon contamination. These carbon contaminations are commonly used as charge reference for

XPS spectra or calibration purpose during the measurement. In case of nonconductive samples, charges build up causing all peak of the XPS spectra to shift to higher binding energy. This can be reduced by exposing the surface to a neutralizing flux of low energy electron. A good reference peak such as the C peak is essential for correction of the charging effect as shown in figure 3.7 where a buildup of charges on the surface causes a shift in the spectrum either to lower or higher binding energy depending on the type of charges

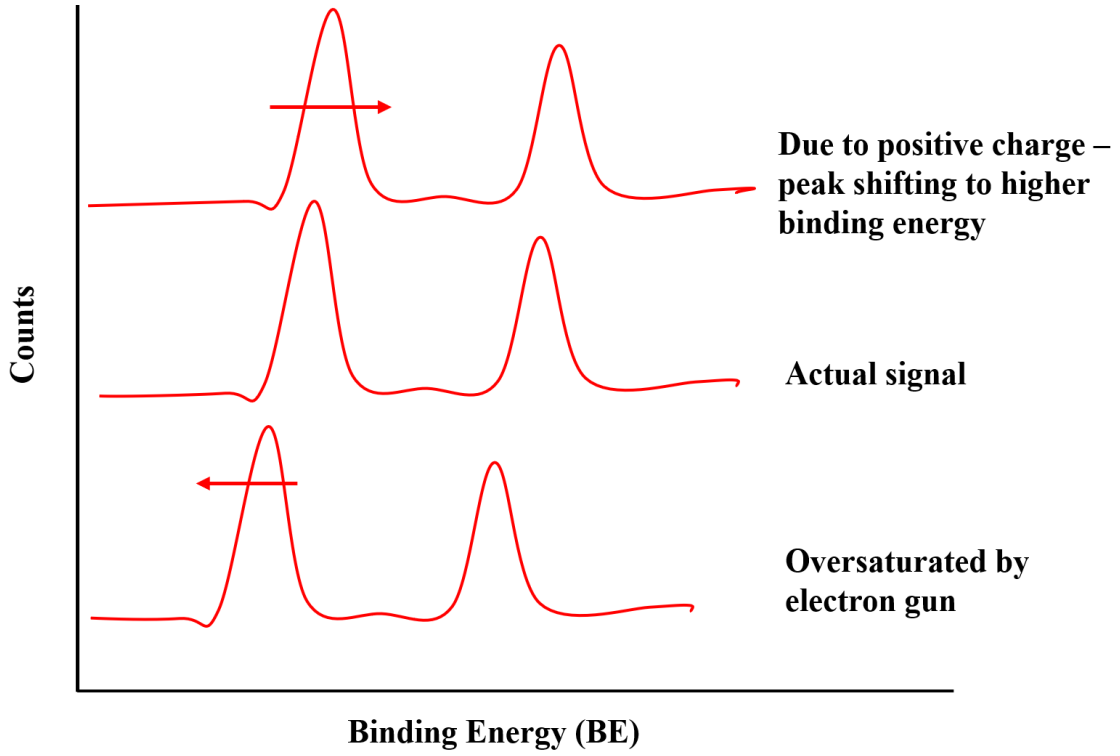

Figure 3.7. Peak correction using reference peak C 1s.

XPS spectra (number of electrons per unit time normalized by electron energy versus BE) contains characteristics of a stepped background, which is due to the inelastic process or extrinsic losses from deep in the bulk as well as peak splitting. Electrons close

to the higher shell escape without energy loss while electrons deeper into the surface lose more energy and emerge with reduced kinetic energy. The electrons very deep in the sample far from the surface can lose all their energy and cannot escape. Note that electrons with a large BE such as 1s electrons emerge with a very low kinetic energy and have a much lower probability to escape from the sample than lower binding energy 2p, 3s, 3d electrons.

A Typical XPS instrument, shown in figure 3.8 includes:

1. Vacuum chamber
2. Load-lock
3. X-ray source
4. Energy analyzer
5. Vacuum pump
6. Neutralizer

(1) Vacuum chamber:

In the vacuum chamber probing of the sample is carried out. It has a primarily spherical shape, usually made of nonmagnetic materials to avoid photoelectron deflection due to the magnetic field. It includes viewports, sample stage and at a minimum an electron flood gun x-ray source, manipulator, and vacuum pumps, together with the analyzer. This chamber has its own associated pumping stage. The XPS chamber is furnished with a load lock by a manual gate valve which allow independent pumping. An XPS chamber's base pressure is usually in the range of 1×10^{-10} mbar.

(2) Load Lock:

The load lock chamber permits quick pump down for sample loading and unloading purpose. This chamber is isolated from the main chamber via a manual UHV gate valve. A turbomolecular pump is used to evacuate the load lock chamber creating an ultimate pressure $<5x10^{-8}$ mbar. The magnetically couples transfer arm connected to the load lock is used to transfer samples into and out of the main chamber.

(3) X-ray source:

The main integral part of the X-ray photoelectron spectroscopy is a monochromatic X-ray source of Al to provide photons of known energy. To produce X-rays, electrons are accelerated toward Al with a typical applied anode voltage around 15kV. The X-rays emitted from the Al anode is the Kα radiation with an energy of 1486.6 eV. When the produced X-rays fall on the sample surface photoelectron are created, which are focused into the energy analyzer.

(4) Energy analyzer:

The energy analyzer is an essential part of the system for measuring the kinetic energy (or binding energy) of electrons during the XPS experiments. A multi-element electrostatic lens around 30mm working distance is used to gather photoelectrons and focus the electron beam into the hemispherical energy analyzer, which sorts the electrons according to their kinetic energy, i.e. that is faster electrons will reach the detector further outside than slower electrons. The lens may accelerate or retard the electrons relative to the energy at which they leave the sample surface, which offer adjustable magnification and angular acceptance. The lens and aperture can be changed, which allow collection of photoelectrons from the sample surface, that is smaller than the illuminated area.

(5) Neutralizer:

The XPS technique depends on the emitted electrons from the sample that find their way into the analyzer. If these emitted electrons do not leave the surface, the sample will be charged creating a retarding electric field at the sample surface. For conducting samples, the charging effect is easily solved if the sample is connected to the instrument ground. However, in the case of a highly insulating sample that is electrically isolated from the instrument charge accumulates at the sample's surface which hinders the collection of photoelectrons and distorts the spectra resulting in binding energies shifted from their original position. To have a good stable signal it is essential to maintain a steady state surface potential at the sample surface. An electron gun neutralizer is used to maintain a constant surface potential by minimizing the charging effect. The measured C 1s peak position is used for determining charge compensation and perform corrections to the spectrum.

(6) Pumping systems:

Each vacuum chamber includes its separate pumping system. A turbo molecular pump with a two-stage rotary pump is used to pump the chamber down from atmospheric pressure. For example, the first entry lock chamber (load-lock) is pumped via a separate turbo molecular pump with a two-stage rotary pump. The turbo pump is separated from the vacuum chamber by an electro-pneumatic gate valve, which is interlocked to avoid unintentional venting of the vacuum chambers by closing automatically if the turbo or main power fails. The turbo pump cannot run independently; first the roughing pump starts pumping down up to certain pressure then turbo pump is switched on.

(7) Pressure readings:

The chamber pressure is measured using an ion gauge, a Pirani gauge as well as combination of ion-Pirani gauge and a cold cathode gauge. The ionization gauge uses thermionic electrons emitted from a hot filament (emission current) to create ions in a defined volume. These thermionic electrons ionize gas molecule, and they accelerate toward the collector electrode and create a current in a detection circuit. The measured current is proportional to the gas molecule density in the chamber [155]. The ion gauge can be used to measure pressure in the range of 10^{-4} to 10^{-11} mbar. The Pirani gauges rely on the principle that a hot wire, placed in a vacuum chamber, will change its resistivity as the thermal conductivity and pressure of the residual gas surrounding changes, i.e. change in resistance due to pressure is observed [155]. The operating range of a Pirani gauge is typically 3 to 10^{-3} mbar. Finally, a cold cathode ionization vacuum gauge uses two electrodes (cathode and anode) and high voltage is applied between them via a series of resistor. Due to the high voltage between the electrodes, electrons travel from the cathode towards the anode the presence of a magnetic field to create confined electron plasma, resulting in a gas discharge. This gas discharge current is a measure of the pressure in the vacuum chamber [155]. For full a range gauge, two separate measurement systems (Pirani and cold cathode) are used to measure pressures in the range of 1000 mbar to 1×10^{-9} mbar.

In this research, XPS measurements were performed using a Scienta Omicron as shown in figure 3.8. The measured data were analyzed using a Casa XPS analysis package. A Shirley background was used during the analysis of the measured data and the acquired peak intensities. Gaussian line shapes which define individual components

of the measured peaks with detailed information of the chemical interaction properties were used to deconvolute the peaks in the measured XPS spectra.

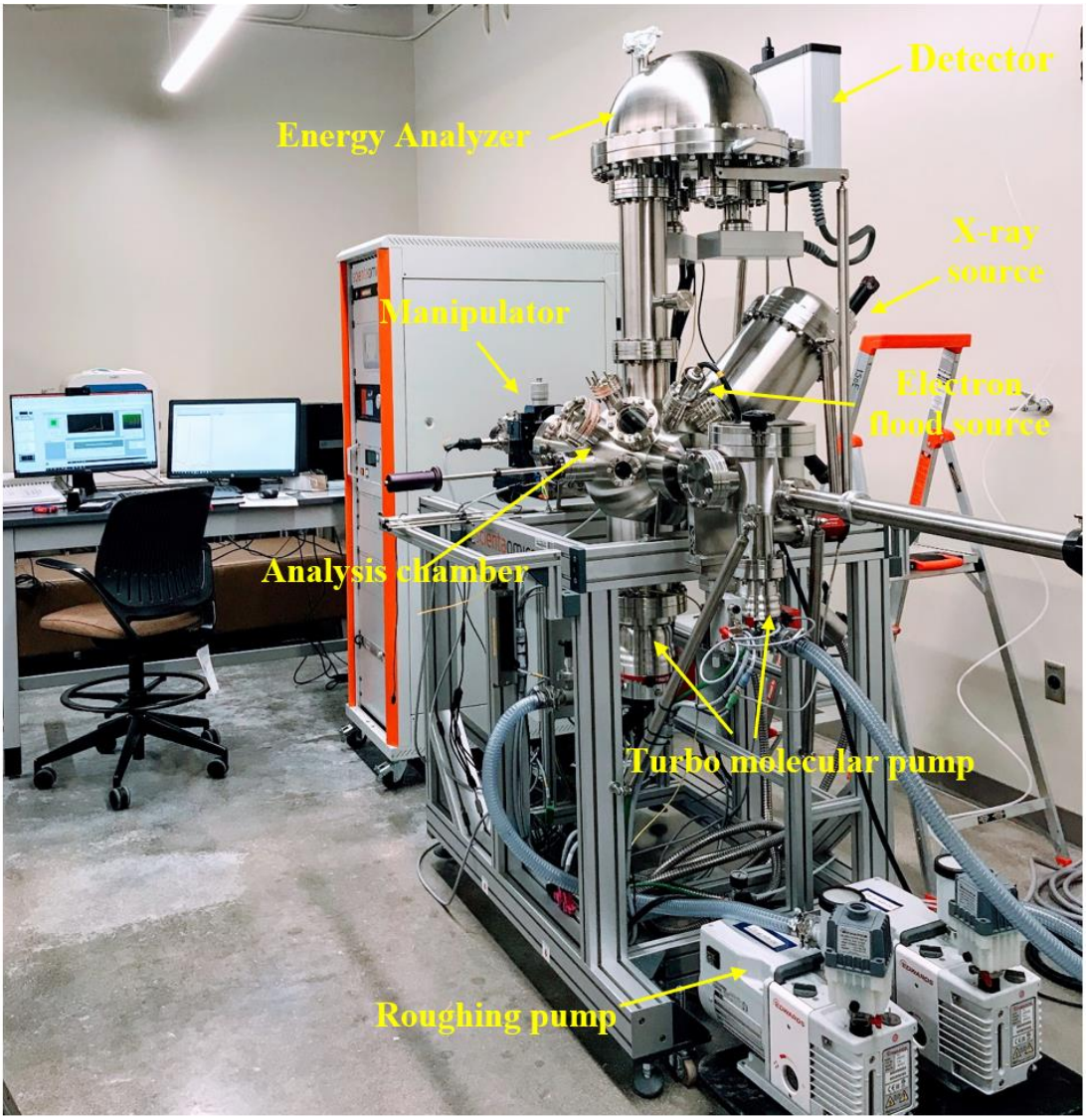

Figure 3.8. Omicron XPS system installed at Texas State University.

3.5 UV-Vis Spectroscopy

Spectroscopy in the ultraviolet (UV), visible (Vis) and near- infrared (NIR) region of the electromagnetic spectrum is often called electronic spectroscopy because electrons are transferred from low-energy to high-energy atomic or molecular orbitals when the material is irradiated with light [156]. Since the energy levels of matter are quantized, only light with the precise amount of energy can cause transitions from one level to another will be absorbed [157]. Figure 3.9 demonstrates the basic layout of a double beam spectrometer used in this measurement.

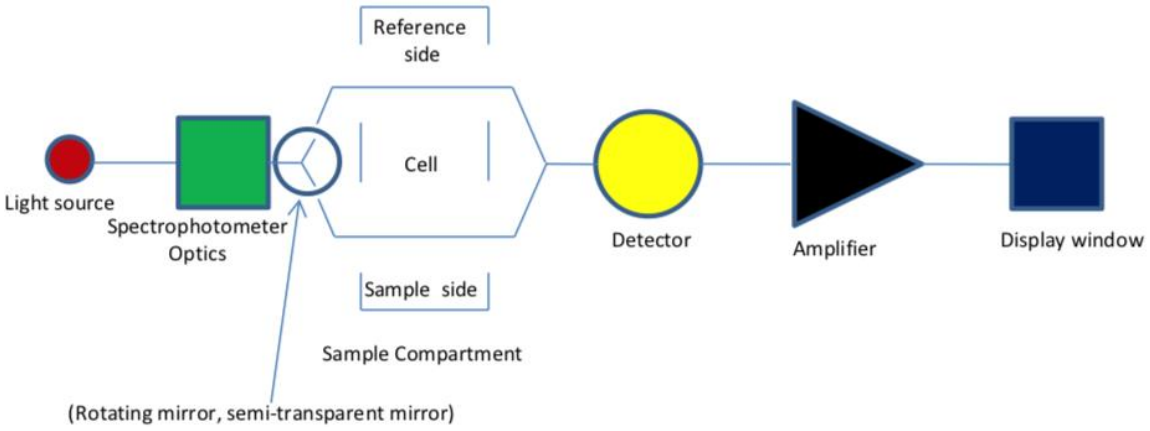

Figure 3.9. Dual beam configuration UV-Visible spectrometer [158].

Light incident on a sample can be reflected, absorbed, or transmitted. Transmittance (T) is defined as the ratio of intensity of light passing through both a reference cell (Io) and the sample cell (I).

$$\% \, T = (I/I_o) * 100 \qquad (8)$$

And absorbance can be obtained from

$$A = -\log(\mathrm{T}) = -\log\left(\frac{\mathrm{I}}{\mathrm{I_o}}\right) = \mathrm{kcb} = \varepsilon\mathrm{bc} \quad (9)$$

The proportionality constant k is unique for a material. When the optical path length is 1 cm and the sample concentration is 1 mole/L, then k becomes molar absorptivity (ε). The absorption coefficient can be determined using following equation:

$$\alpha = A/\lambda \quad (10)$$

λ is the wavelength (nm), multiplied by 10^{-7} to express α in terms cm^{-1}. Alternatively, the optical absorption coefficient can be calculated from

$$\alpha = \frac{1}{t} \times \ln\left[T/(1-R)^2\right] \quad (11)$$

where, R is the reflectance, and t is the film thickness.

The bandgap of the materials can be deducted from the absorption spectra as one expects very little absorption for photons with an energy smaller than the bandgap. The bandgap follows a power law for direct and indirect bandgap materials given by the following expressions:

$$\alpha h\upsilon = \mathrm{B}(h\upsilon - \mathrm{Eg})^{1/2}, \text{for direct} \quad (12)$$

$$\alpha h\upsilon = \mathrm{B}(h\upsilon - \mathrm{Eg})^{2}, \text{for indirect} \quad (13)$$

Here B denotes the absorption edge width parameter, E_g denotes the bandgap, and hυ is the incident photon's energy. By plotting, $(\alpha h\upsilon)^2$ versus hυ, and extrapolating the linear part of that curve E_g can be calculated for direct bandgap materials; this technique is known as Tauc plot analysis. To measure the optical properties of the oxide thin films a UV-2600 Schimadzu optical spectrometer with wavelength ranging 200-900nm (figure 3.10) was used.

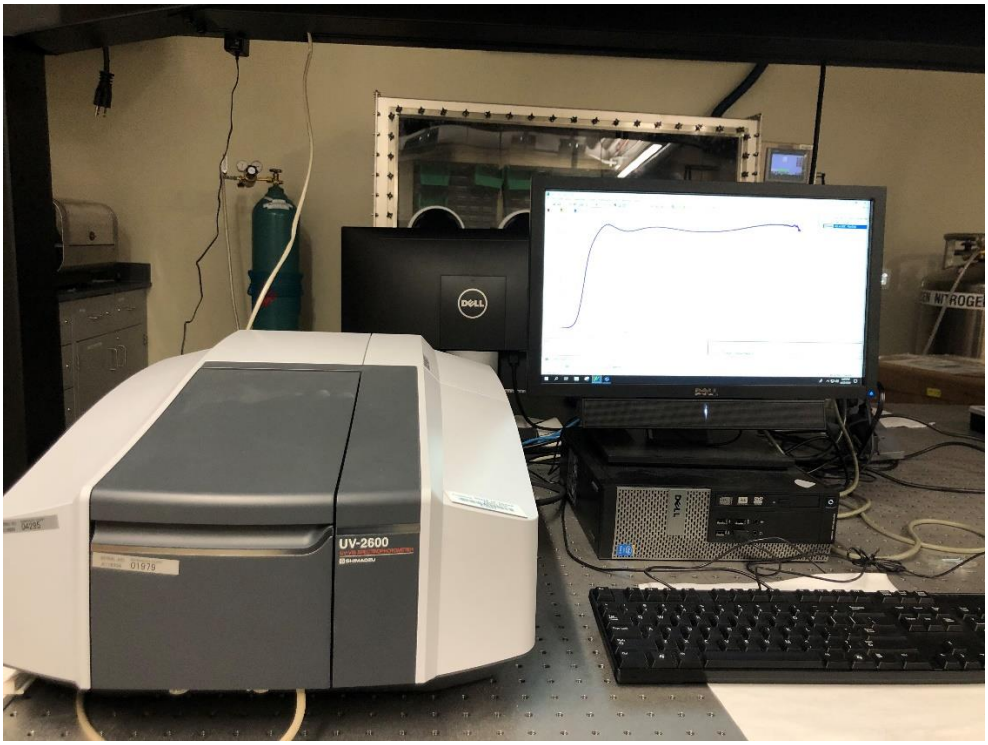

Figure 3.10. UV-2600 SHIMADZU UV-Vis spectroscopy

3.6 AFM

Atomic force microscopy is a technique that allows for the measurement of the surface morphology with unprecedented resolution and accuracy. In this technique, a cantilever with a sharp tip is systematically scanned across a sample surface to produce a nm resolution topographic map [159]. Figure 3.12 is a diagram showing the operational principles of an atomic force microscope.

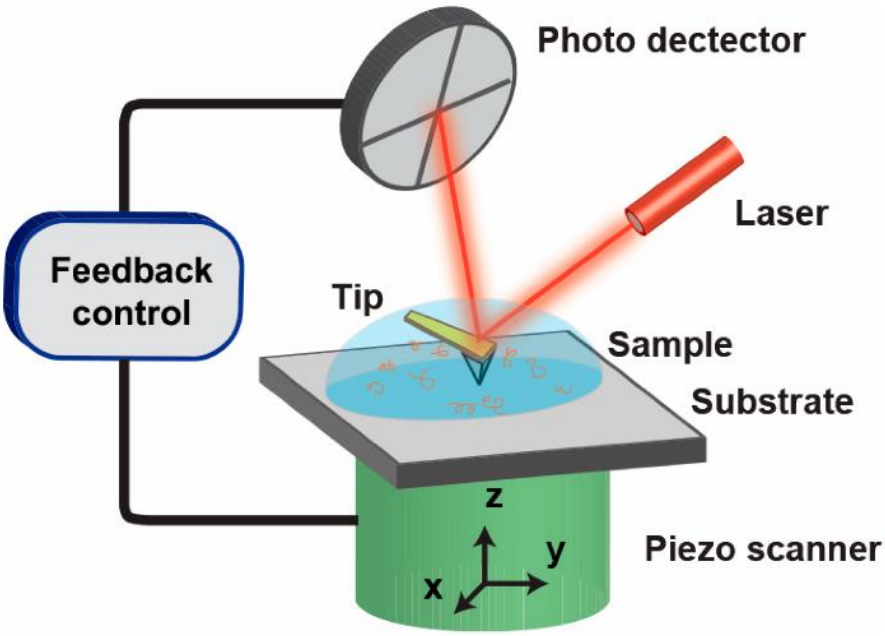

Figure 3.11. A schematic illustration of atomic force microscopy (AFM) [160].

Interactions between the sample and the tip gives rise to either attractive or repulsive forces, these forces give information about the topography of the sample. If the tip and sample are close to each other, the attractive force deflects the cantilever toward the sample, and when the tip is bought into the contact with the sample, the repulsive force deflects the cantilever away from the sample as illustrated in figure 3.13.

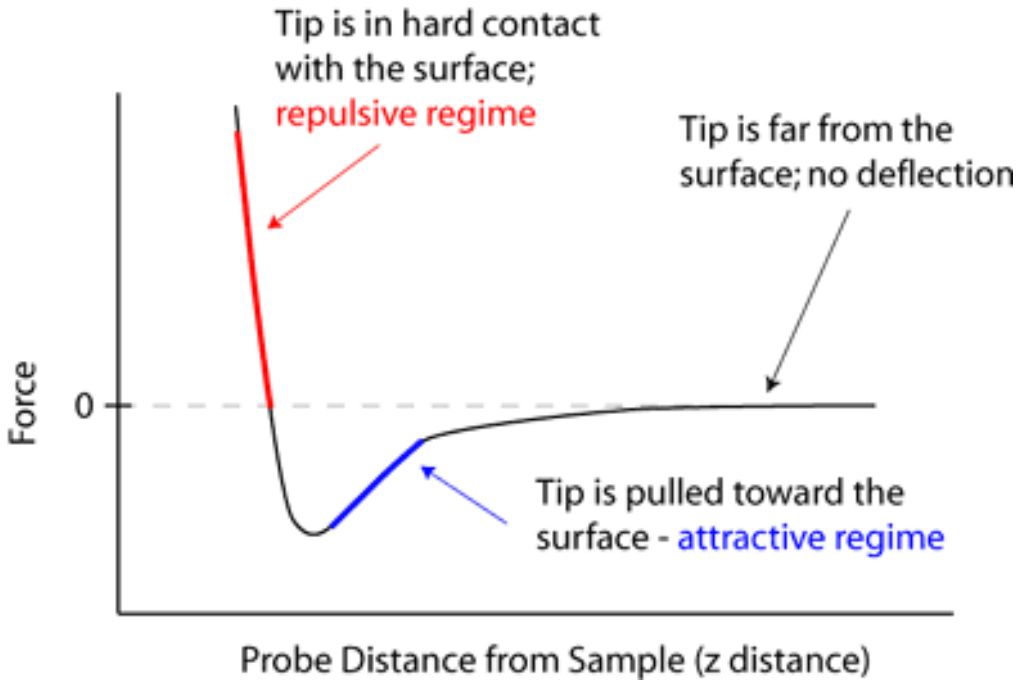

Figure 3.12. Force-distance curve for atomic force microscopy [161].

Basically, the cantilever in an AFM system works as a force sensor. The cantilever deflection is very sensitive, due to a laser beam being used to detect these deflections. This happens when the incident laser beam is reflected off the surface of the cantilever, any deflection will cause changes of the direction of the reflected beam. A detector is used to monitor these changes. Laser position on the photodetector is exploited in the feedback loop to track the surface for imaging and measuring [162]. In this research a Bruker Dimension Icon Atomic Force Microscope (figure 3.14) was used.

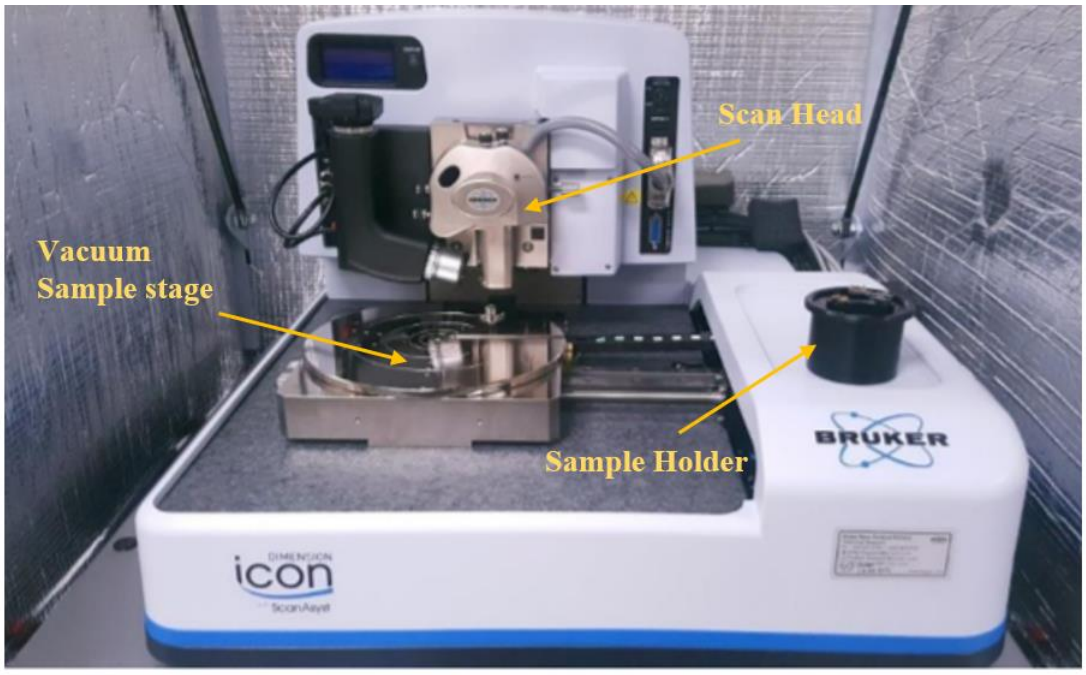

Figure 3.13. Bruker Dimension ICON atomic force microscope, installed at Texas State University.

3.7 VSM

A Vibrating Sample Magnetometer (VSM) is used to explore the magnetic properties of thin film samples. The goal of this technique is to measure the magnetization (M) or the magnetic moment (m) as a function of the applied magnetic field, field angle and sample temperature. When the sample is placed between the pole pieces of an electromagnet it becomes magnetized. The magnetic moment of the sample creates the sample's own magnetic field: this magnetic field is also known as the sample's magnetic stray field. This magnetic stray field is measured by placing pickup coils strategically around the sample and vibrating the sample up and down. This results in a changing magnetic field inside the coils. Consequently, this changing magnetic field produces an induced emf according to Faraday's law in the sensing coil which is fed to a

lock-in amplifier to get a measure of the magnetization. The output signal from the sensing coil goes to the lock-in amplifier, gets amplified and enhanced to extract the magnetic signature of the sample. This is the basic working principle of the VSM, and schematic diagram as shown in the figure 3.14.

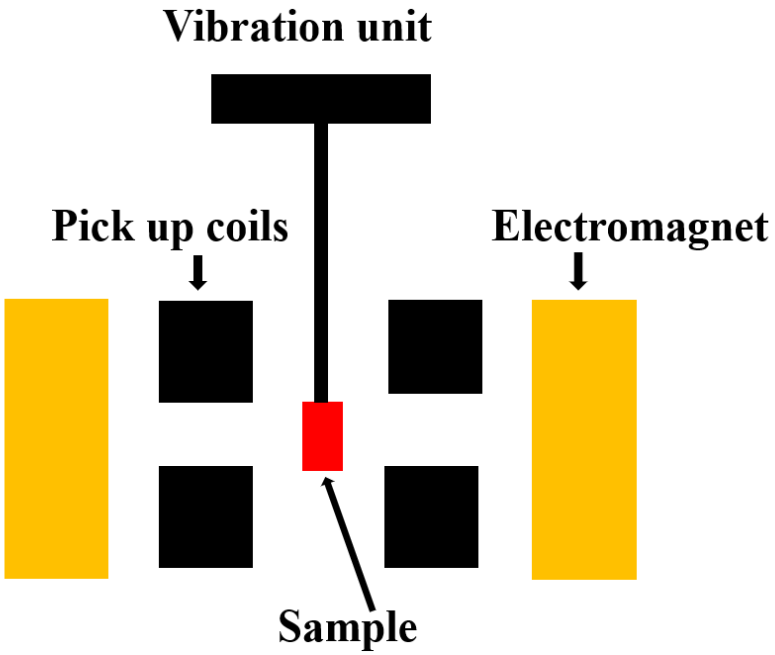

Figure 3.14. Schematic diagram of a vibrating sample magnetometer.

In this study, a MicroSense vibrating sample magnetometer (VSM) was used to explore the magnetic properties of samples. Figure 3.15 shows the installed VSM which can apply magnetic fields up to 2.2 tesla when using the vector coils. The temperature range is -195^{o} C to 725^{o} C.

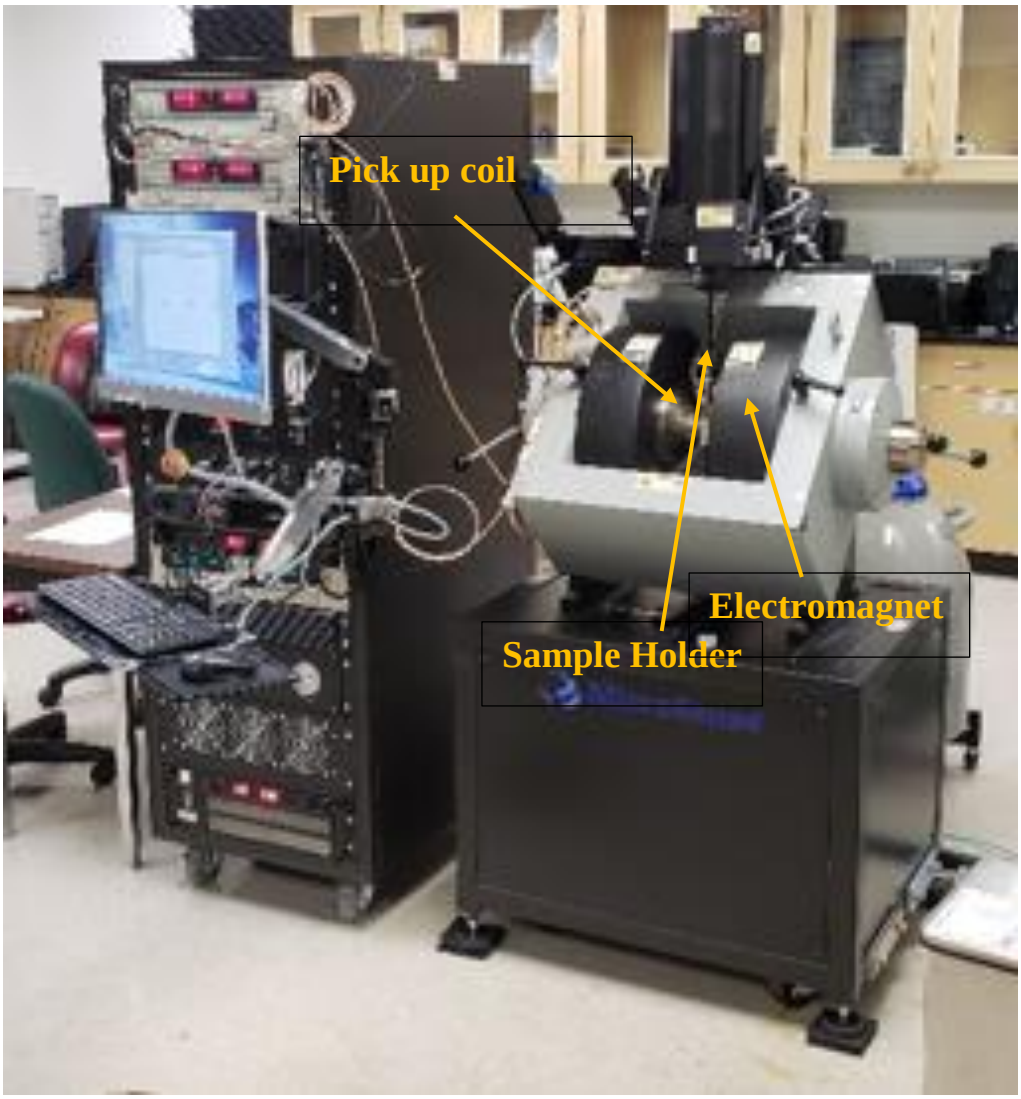

Figure 3.15. Installed VSM system at Texas State University.

3.8 EDS

An object irradiated by the incident electrons can produce various electromagnetic waves and electrons. When a incident electron knocked out the inner shell electron of the constituent atoms in the object, the vacant orbital is filled by the outer shell electron by releasing X-ray, whose energies equal to the energy difference between the outer shell electrons and inner shell electrons. These X-ray are called characteristic X-rays as their

energies are characteristic of distinct elements, which is used for elemental analysis. Characteristic X-rays emitted from the excitation of K-shells, L-shells, M-shells electrons are called “K lines”, “L lines”, and “M lines”, respectively. The characteristic X-rays from heavier elements are higher, therefore, high incident energy is required to excite the heavier element to emit characteristic X-ray radiation. In contrast, different X-rays are produced while incident electrons are deaccelerated by the atomic nucleus. These emitted X-rays are called “background X-rays” or “white X-rays” or “continuous X-rays”.

The energy dispersive X-ray spectrometer (EDS) analyzes characteristic X-ray radiation by measuring the energies of the X-rays. At first, X-rays emitted from the object hit the analyzing crystal, which diffracts the X-rays, and finally the radiation enters the detector, electron hole pairs are generated and their energies are measured to determine the elements in the substance. In this research a JEOL SEM system equipped with a EDS detector were used for elemental analysis as shown in figure 3.16.

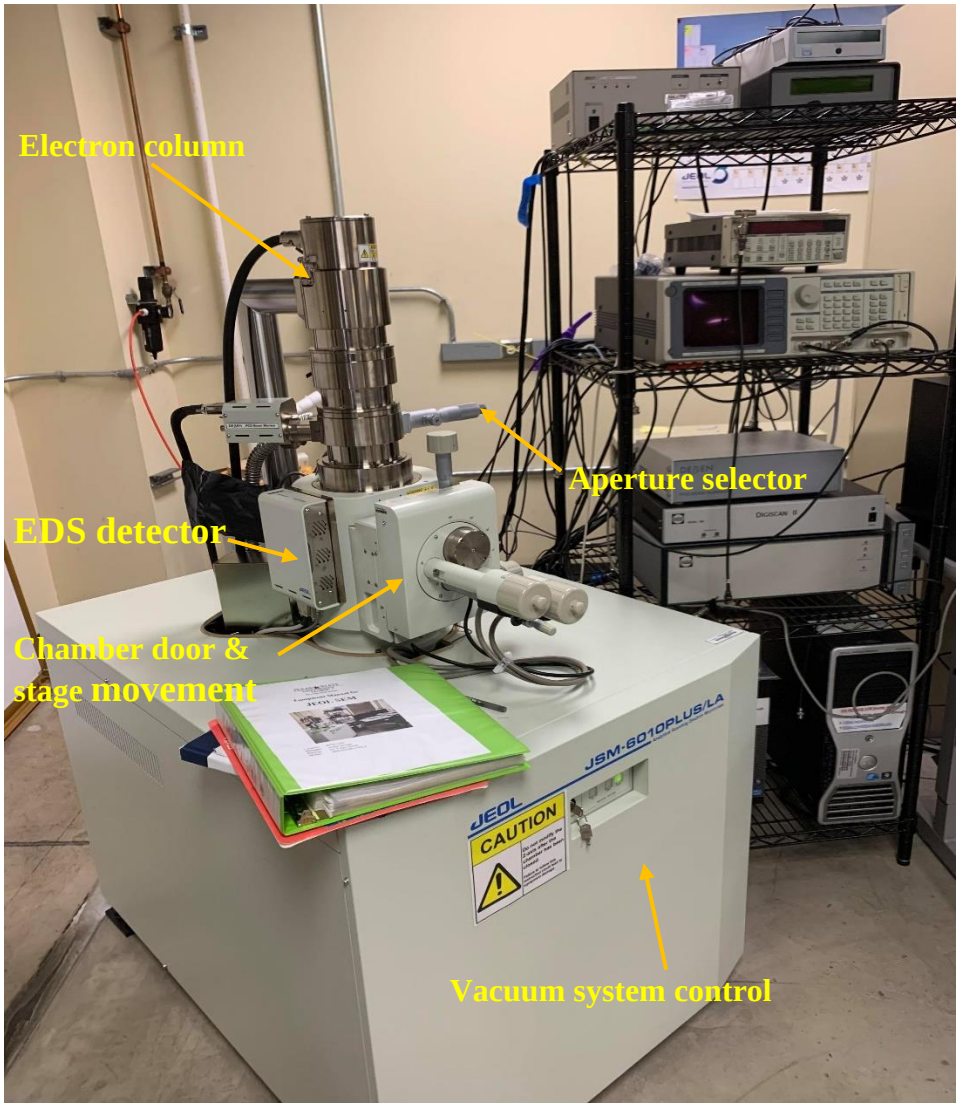

Figure 3.16. Installed JEOL SEM system equipped with EDS detector at Texas State University.

4. GROWTH AND CHARACTERIZATION OF Ga_2O_3 & $(Ga_{1-x}Gd_x)_2O_3$

4.1 Introduction

Thin film wide bandgap Ga_2O_3 based alloys are important for applications in high power electronics and deep UV photonic devices and detectors. Ga_2O_3 exists in five different polymorphs, i.e. α, β, γ, δ and ε. Among them, the most studied and promising is β-Ga_2O_3, which development has been further accelerated due to the availability of high-quality substrate material. Different techniques were used to grow β-Ga_2O_3 and its alloys, for example, PLD[163]–[167], Radio frequency sputtering[168], MBE[169]–[176], MOCVD [177], LPCVD[178], ALD[179], halide vapor phase epitaxy (HVPE)[180] and solution processes[181].

Optical and electrical properties can be modified by n-type doping and bandgap engineering alloying with Al and In. Incorporation of Si[18], Sn[182],[183] and Ge has been successfully used to realize n-type Ga_2O_3. In addition, the bandgap modifications of $(In_xGa_{1-x})_2O_3$ [91], $(Al_xGa_{1-x})O_3$ [184]–[187] with In and Al contents have been reported, providing great flexibility for device design.

Investigations of alloys of Ga_2O_3 deposited by pulsed laser deposition on c-plane sapphire substrates with compositions that maintain the monoclinic phase would be useful. This would open opportunities for the development of heterostructures with Ga_2O_3 creating bandgap adjustable device structures with an array of applications. For example, incorporation of Gd in the higher bandgap material can be used as a gate dielectric in MOSFET devices and due to the high nuclear cross section of Gd for radiation detectors.

An ideal wide bandgap semiconducting material should possess high electron mobility, excellent thermal conductivity, high electrical breakdown voltage as well as the presence of a two-dimensional electron gas (2DEG) in heterostructure either due to a polarization effect or at heterointerfaces. Ga_2O_3 has been attracting a lot of attention because of its promise for application in future electronic and photonic devices. Its optical bandgap is tunable over a large range by alloying with either In or Al. Furthermore it has a high electrical breakdown voltage (V_{br}), has a large physical and chemical stability in extreme environments, and shows more promise for mass production as compared to their SiC and GaN counterparts [8]. Ga_2O_3 possesses high density, a predicted high breakdown voltage (8 MeV/cm^{-2}) as well as a wide bandgap (4.9eV) [188], which are vital features for ionizing solid state radiation detectors. In addition, Gd has the largest nuclear cross section (48000 barn, 1 barn=10^{-28} m^{-2}) for neutron capture and emission of internal conversion electrons in an energy range from a few tens to hundreds of keV [189]. Alloys of Ga_2O_3 with Gd, can replace the currently dominated and costly semiconducting materials CdZnTe used in neutron detection.

Recently, J. Kim et al. investigated radiation hardness in Ga_2O_3 [190]. The preliminary data on the effect of electron, proton, x-ray, gamma, and neutron radiation on β- Ga_2O_3 demonstrate comparable radiation resistance to conventional wide-bandgap semiconductors under similar conditions.

However, the properties of $(Ga_{1-x}Gd_x)_2O_3$ thin films are still unknown, though theoretical studies have been reported elsewhere[191]. In this chapter, we will focus on the growth parameters, structural, and optical properties of $(Ga_{1-x}Gd_x)_2O_3$ for (x = 0-13.63 %) and provide guidelines for future experimental work.

4.2 Experiment

Ga_2O_3 is first deposited at various temperatures at a fixed pressure (2.2×10^{-2} torr) to optimize the properties of the thin films. Various targets were fabricated from Ga_2O_3 (99.999%) and Gd_2O_3 (99.999%) powder with different Gd (mole ratio of Gd/(Ga+Gd)) concentration. Single side polished c-plane sapphire crystals which were cleaned ultrasonically using acetone, isopropanol, deionized water and finally dried with nitrogen gas, were used as substrate. A krypton fluoride (KrF) laser source having a wavelength of 248nm was used to ablate the target onto the substrate. A laser pulse frequency of 5Hz and a laser beam energy density of $2J/cm^2$ were used to deposit the films. The rotation of substrate and target, and the distance between them were carefully controlled to maintain uniformity and avoiding crater formation on the target. After growth, each film was annealed in situ at 50°C above the growth temperature for 15 min without oxygen.

4.3 Results and Discussions

Figure 4.1 shows the XRD 2θ scans of films grown at 400, 500, 650, 750, and 850°C at a fixed oxygen pressure of 2.2×10^{-2} torr on (0001) oriented α -Al_2O_3 substrates. The X-ray spectra confirm the formation of (-201) oriented single phase of β-Ga_2O_3 films. The peaks for the set of {-201} planes of ß-Ga_2O_3 are positioned around the 2θ angles 18.92°, 38.31°, 59.97°, and 82.03°, corresponding to the reflection planes of (-201), (-402), (-603), and (-804). The peaks labeled with (0001), (0006) and (0009) at the 2θ angles around 20.52 °, 41.66 °, and 64.47 ° are attributed to the reflection of the sapphire substrate. A single crystalline phase was observed for all growth temperatures except for the lowest temperature. The spectra measured on the film grown at 400 °C shows extra diffraction peaks representing the (110), (600), and (113) diffraction peaks of

β-Ga_2O_3. These results indicate a polycrystalline nature of the film grown at 400 ºC. The lowest full width half maximum (FWHM) of 0.21 deg was obtained at a growth temperature of 850ºC suggesting that growth at high temperatures facilitates the formation of a high-quality single crystal ß-Ga_2O_3 phase. To determine the optimum temperature for the growth of $(Ga_{(1-x)}Gd_x)_2O_3$, thin films for x=2.62% and 9.32% were grown at different temperatures and the crystal quality of the alloy was investigated using XRD. The XRD spectra are summarized in figure 4.2. From the figure it can be clearly seen that at 400º C, the films are amorphous but, as the temperature increases there is a gradual increase in the crystalline quality of the deposited films. However, for the lowest composition of 2.62% the (110) and (600) peaks appear below 750º C, indicative of a polycrystalline nature of the grown films. Based on the crystalline quality inferred from XRD, a temperature of 850º C for the growth GaGdO alloys was used. This high temperature is needed to provide enough thermal energy for molecules and atoms to increase the surface mobility that would lead to a crystalline (-201) monoclinic alloy structure.

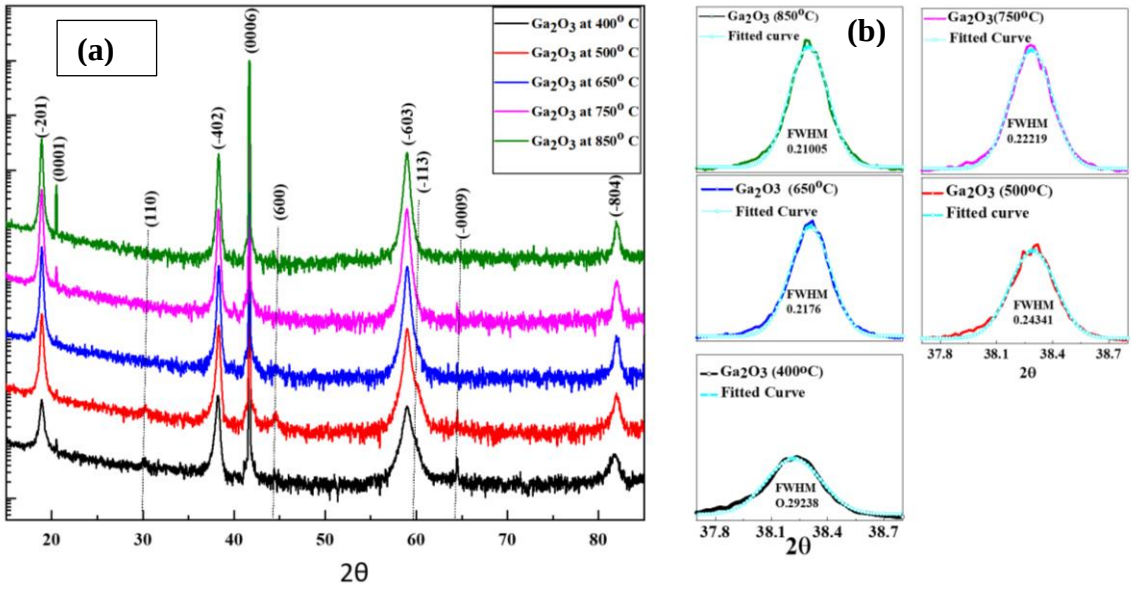

Figure 4.1. (a) XRD measurement of undoped Ga_2O_3 grown at different temperatures and (b) corresponding FWHM measurement of (-402) plane.

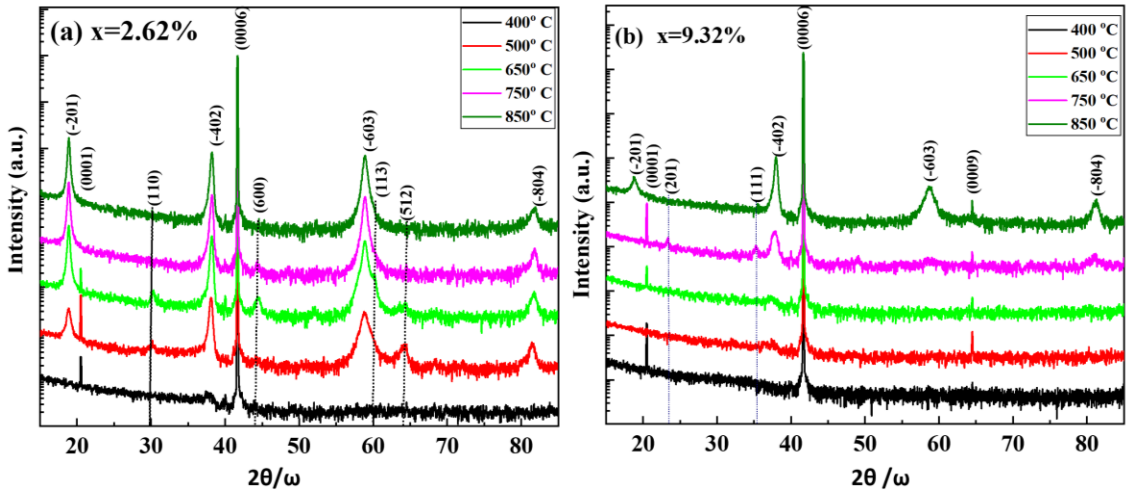

Figure 4.2. 2-theta-omega scans of temperature dependent $(Ga_{(1-x)}Gd_x)_2O_3$ thin films for (a) x=2.62% and (b) x=9.32%.

Finally, $(Ga_{(1-x)}Gd_x)_2O_3$ thin films for x= 0 -13.63% were grown at a fixed temperature of 850° C and oxygen pressure of 2×10^{-2} torr. The XRD 2θ/ω scans of the composition series are shown in figure 4.3. Exclusively observed sharp peaks at 18.89,

38.23, 59.00 and 81.83° caused by Bragg reflection planes (-201), (-402), (-603) and (-804) of epitaxially grown layers has a monoclinic structure similar to β-Ga_2O_3. Figure 4.3(b) shows an extended view of 2 theta-omega XRD scans around angle 38°, where the diffraction peak (-402) is located. The shift to lower 2-theta angle with increasing Gd content suggests an expansion of lattice constants caused by the inclusion of Gd into Ga ion lattice sites [192]. This can be explained due to the larger Gd ions (radii of Gd^{3+} is 0.938 Å) compared to the Ga ions (radii of Ga^{3+} is 0.62 Å) [193]. While crystalline films were obtained for Gd content up to 9%, further increase of the Gd concentration tended to deteriorate the structural quality leading to an amorphous film for Gd content ≥10 % when grown at 850°C. It may be possible to improve the crystallinity by increasing the substrate temperature during deposition for these high Gd content films.

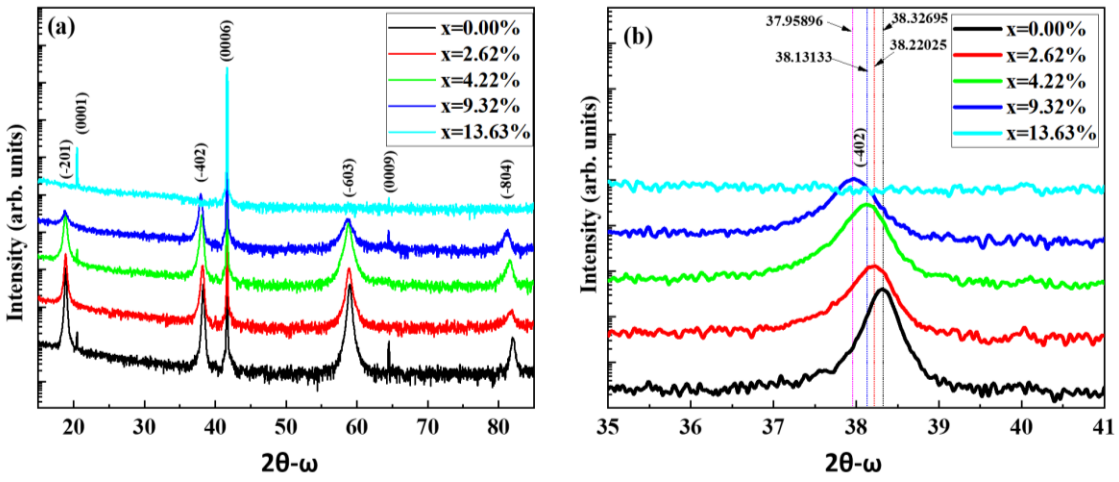

Figure 4.3. XRD patterns of $(Ga_{(1-x)}Gd_x)_2O_3$ thin films for x= 0, 2.62%, 4.22%, 9.32%, 13.63%, grown at 850 °C and 2×10^{-2} torr.

To investigate the epitaxial relationship, we performed XRD Φ scans of the (111) plane of the $(Ga_{(1-x)}Gd_x)_2O_3$ thin films and the (104) plane of the sapphire substrate

respectively, as shown in figure 4.4 (a) and (b). Six peaks separated by 60^{o} are obtained for the Gd-Ga_2O_3 alloy as shown in figure 4.4(a), while in figure 4.4(b) three peaks separated by 120^{o} apart represent the symmetry of the sapphire substrate. Hence, it can be concluded that the grown thin films have 2-fold in-plane rotational symmetry representing 2 domains. Furthermore, the substrate has 3-fold rotational symmetry. This implies 2-fold $(Ga_{(1-x)}Gd_x)_2O_3$ thin films epitaxially grown in three different axis at a constant rate, resulting in a 6 fold symmetry [194], [195].

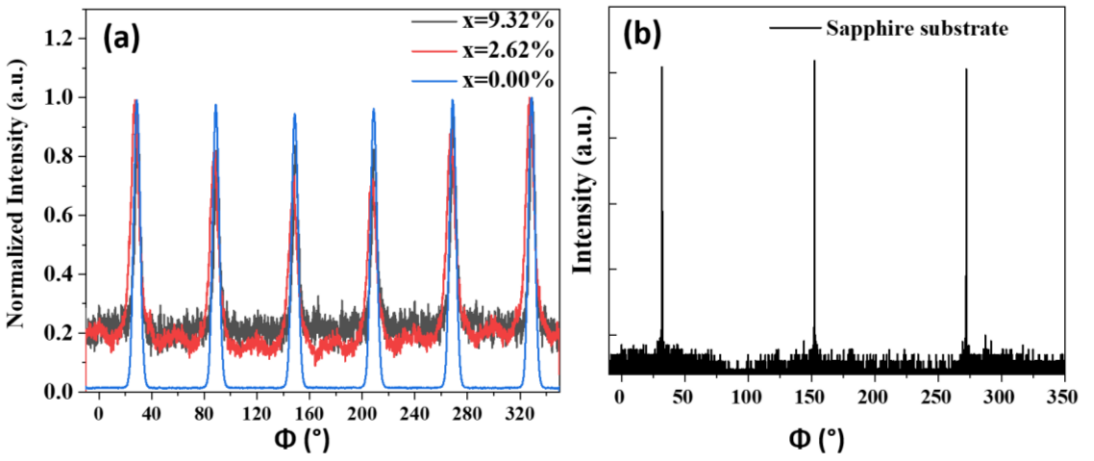

Figure 4.4. (a) XRD phi scan of (111) plane of $(Ga_{(1-x)}Gd_x)_2O_3$ thin films for x= 0, 2.62%, 9.32% (b) phi scan of (104) plane of Al_2O_3 substrate.

To examine the surface topography and roughness, AFM images were taken using an atomic force microscope (Bruker Dimension ICON) using the soft tapping measurement mode. Results are shown in figure 4.5. The scan size of the AFM images was (1×1) μm^2 and a scanning frequency of 1 Hz was used. From the images no significant void or breakage was observed. Noticeable surface change was observed with the increasing Gd concentration, with relatively low root mean square (RMS) roughness

ranging from 1.828nm – 0.256nm as the Gd content was increased from 0 to 13.9%. It is observed that grains size having conical shapes decreases with increasing Gd concentration. The x=13.63% film showed the lowest grain size and roughness and its XRD spectra showed that it is amorphous.

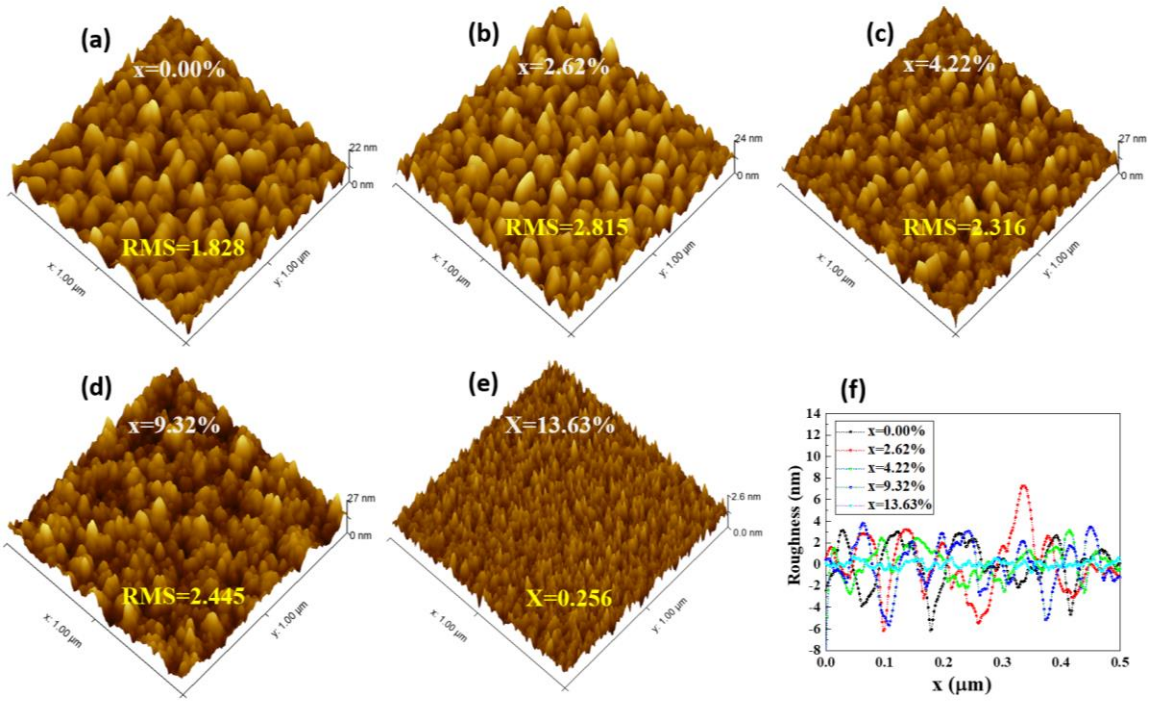

Figure 4.5. AFM images of $(Ga_{(1-x)}Gd_x)_2O_3$ thin films for (a) x= 0.00%, (b) 2.62%, (c) 4.22%, (d) 9.32%, (e) 13.63%, and (f) is corresponding roughness.

For optical applications, for example a solar blind photodetector, a knowledge of the optical properties of the films is essential. Transmission measurements were taken using a Shimadzu UV-2600 spectroscopy UV-Vis system. All samples exhibit high transparency from the visible to the ultraviolet regions as shown in figure 4.6(a). Pure β-Ga_2O_3 shows a sharp optical absorption edge around 250nm, while the Gd doped sample shows a slight red shift suggesting a slight decrease in the bandgap. The optical bandgap

is obtained by fitting the linear region (inset) using the Tauc equation $(\alpha h\nu)^{1/n} = B(h\nu - Eg)$, where α is the absorption coefficient, hυ is the irradiation energy, B is constant, Eg denotes bandgap. The n is a constant and is a 1/2 for a direct bandgap material and 2 for an indirect bandgap material [196]–[198]. The optical absorption coefficient α of the film were evaluated using relation [199], $\alpha = (\frac{1}{t})ln\,[T/(1-R)^2]$, where T is transmittance, t is the film thickness, and R, the reflectance. The analysis showed that the material possesses a direct bandgap that showed a slight linear decrease with increasing Gd concentration up to 4% and appears to stay constant with further increase in the Gd concentration. This can be due to the formation of defects in the crystal or the presence of unoccupied electronic state below the conduction band, in accordance with a theoretical study performed by Cheng et al. [191].

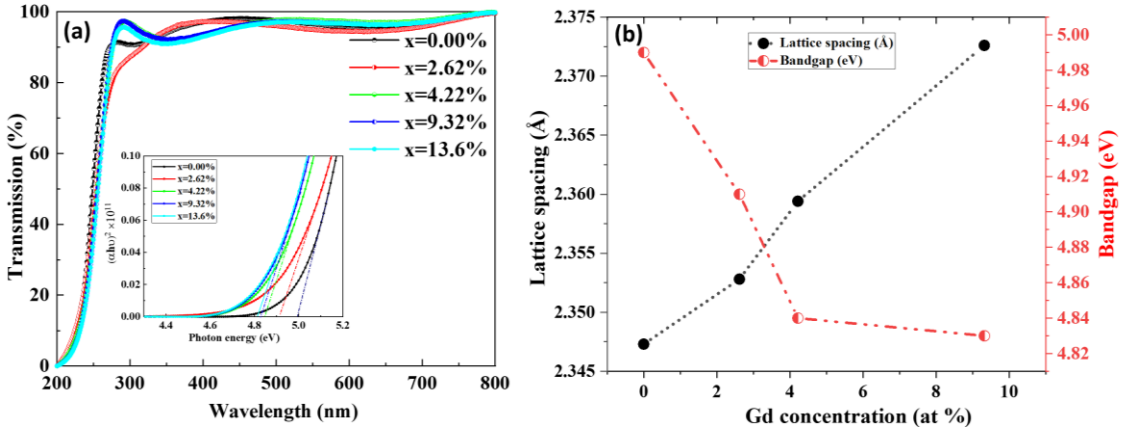

Figure 4.6. (a) Optical transmittance (inset Tauc plot) and (b) concentration versus interplanar distance and bandgap of $(Ga_{(1-x)}Gd_x)_2O_3$ thin films for x= 0, 2.62%, 4.22%, 9.32%, 13.63%.

To investigate further the compositional dependent optical properties of $(Ga_{(1-x)}Gd_x)_2O_3$ thin film, spectroscopic ellipsometry measurements were carried out. With this

spectroscopic measurement, optical properties were studied at room temperature in the spectral range of 1.24eV to 6.2eV for the following three angle of incidence: 55°, 75° and 85°. Standard ellipsometry parameters ψ and Δ are expressed as a ratio of Fresnel reflection coefficients parallel (r_p) and perpendicular (r_s) to the plane of incidence[200],[201]–[203].

$$\rho = \frac{r_p}{r_s} = \tan(\Psi) \times e^{i\Delta} \tag{14}$$

The wavelength dependence ψ and Δ were measured and analyzed to extract the physical optical data. For such analysis, it is a requirement to build a model for the substrate/thin film stack to extract any meaningful information from the measurements. Figure 4.7 shows the model that was used to simulate the experimental data, which contains a top layer modelling the surface roughness, a $(Ga_{(1-x)}Gd_x)_2O_3$ layer and finally the substrate (Al_2O_3). In addition, the accuracy of the model, were determined by Levenberg-Marquardt regression algorithm which was used for minimizing the mean square error (MSE) of the ellipsometry quantities ψ and Δ [204], [205].

$$MSE = \frac{1}{2n-m}\sum_{i=1}^{n}[\{\frac{(\psi_{exp} - \psi_{calc.})}{6_{\psi_i}^{exp}}\}^2 + \{\frac{(\Delta_{exp} - \Delta_{calc.})}{6_{\Delta_i}^{exp}}\}^2] \tag{15}$$

where ψ_{exp}, $\psi_{calc.}$ and Δ_{exp}, $\Delta_{calc.}$ are experimental and calculated ellipsometry parameters, m the number of fitting parameters, n the number of measurements of Δ and ψ pairs, and σ the standard deviation of the experimental measurement results.

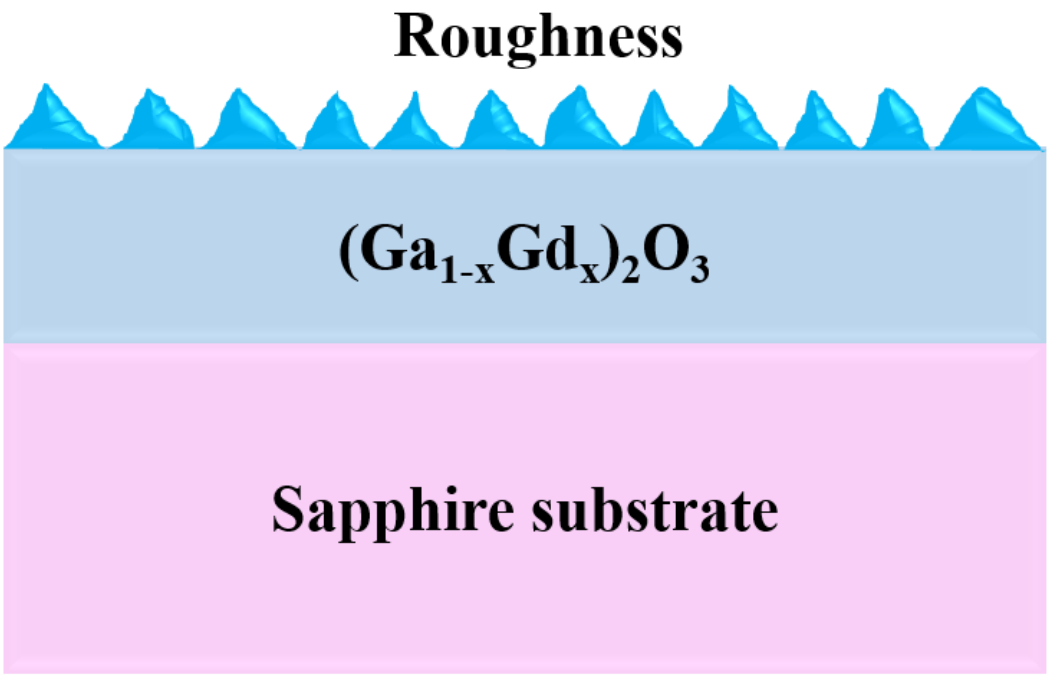

Figure 4.7. Constructed stack model for $(Ga_{(1-x)}Gd_x)_2O_3$ thin films for ellipsometry data analysis.

Typically, all thin films have some region of optical transparency, i.e. vanishing imaginary part where the extinction coefficient, k=0. This transparent region can be analyzed to extract the index of refraction, n, and the thickness of the film by the Cauchy Sellmeier equation (16) [202], the results of which are shown in figure 4.8 for the various films.

$$n(\lambda) = a + \frac{b}{\lambda^2} + \frac{c}{\lambda^4} \qquad (16)$$

where n is refractive index, λ is wavelength, and a, b, c are constants describing the dispersion of the film. At first, multiple data sets were evaluated using the Cauchy function in the transparent spectral region to determine the film thickness. After this a B-spline dispersion model (a mathematical description of dielectric function to interpret semi absorptive thin films) was used then to obtain the optical parameters in the

absorbing spectral range, where Kramers-Kronig (KK) relationship was maintained by evaluating values of the extinction coefficient k and the refractive index n. Finally, the derived data were fitted using a Tauc Lorentz oscillator model and UV pole functions, to obtain the results as shown graphically in figure 4.8(a) and (b). The bandgap for β-Ga_2O_3 was determined to be 4.75eV and decreased to 4.57eV as the incorporation of Gd increases, which is in good agreement with a previous study [202]. While the trend of bandgap variation agrees with that determined by UV-Vis, the values obtained by ellipsometry are slightly lower. One reason could be that the ellipsometry estimates the bandgap considering an isotropic medium. Table 4.1 shows the extracted data from the ellipsometry measurement of $(Ga_{(1-x)}Gd_x)_2O_3$ thin films for x= 0, 2.62%, 4.22%, 9.32%, 13.63%. The index of refraction obtained from all the films is similar with a value of around 1.9 at 632 nm.

Table 4.1: Materials properties of $(Ga_{1-x}Gd_x)_2O_3$ at pressure 2.2×10^{-2} torr and temperature 850°C.

Gd concentration	Thickness (nm)	Bandgap (eV)		Refractive index at 632nm	Roughness from Ellipsometer (nm)	RMS Roughness using AFM (nm)
		Ellipsometry	UV-vis			
0.00%	112.42	4.75	4.99	1.942	2.50	1.828
2.62%	95.54	4.73	4.91	1.938	3.40	2.815
4.22%	141.94	4.72	4.84	1.951	3.00	2.316
9.32%	132.40	4.59	4.83	1.915	2.20	2.445
13.63%	115.00	4.57	4.82	1.909	2.00	0.256

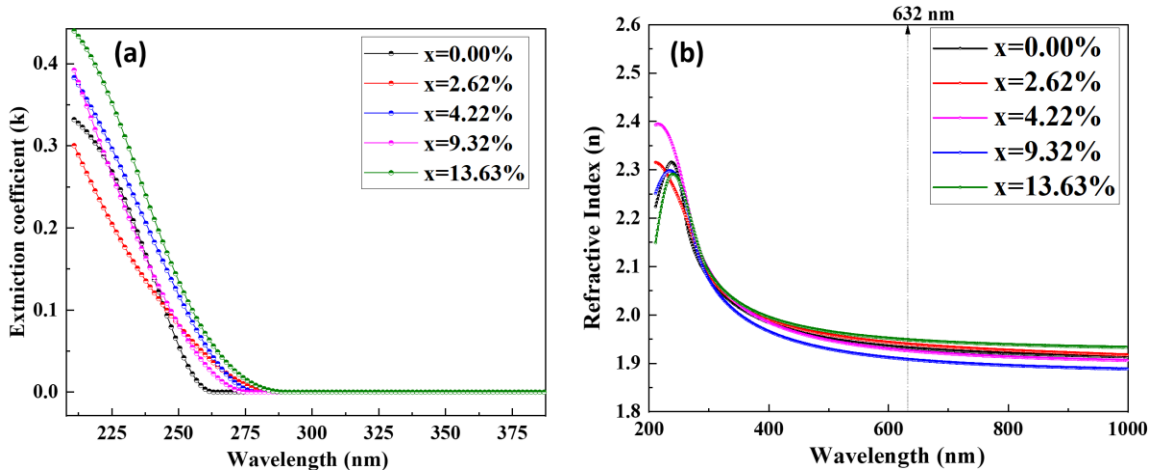

Figure 4.8. (a) Spectra of extinction coefficient (k) and (b) refractive index(n) of $(Ga_{(1-x)}Gd_x)_2O_3$ thin films for (a) x= 0.00%, (b) 2.62%, (c) 4.22%, (d) 9.32%, (e) 13.63%.

The chemical composition of $(Ga_{(1-x)}Gd_x)_2O_3$ thin films for x= 0.00%, 2.62%, 9.32%, 13.63%, was investigated using x-ray photoelectron spectroscopy, with all peaks referring to the C 1s peak at the binding energy of 284.8eV. From survey spectrums, photoelectron lines Ga2p, Ga3p, Ga3d, C 1s, Gd 4d, Gd 3d, O KLL, and Ga LMM Auger lines were detected. The Gd 4d spectrum can be deconvoluted into two components at a binding energy about 141.60 and 147.13 eV which can be attributed to the spin orbit sublevels of Gd $4d_{5/2}$ and Gd $4d_{3/2}$ as plotted in figure 4.9 (g). The emission peaks Gd $4d_{5/2}$ and Gd $4d_{3/2}$ were superimposed illustrating multiplet splitting due to electrostatic interaction between the 4f and 4d shells [206], [143], [207]. The difference between Gd $4d_{5/2}$ and Gd $4d_{3/2}$ of nearly 5.53eV and the presence of Gd 4d peaks confirm the existence of Gd in the form of the Gd^{3+} oxidation states [208],[209].

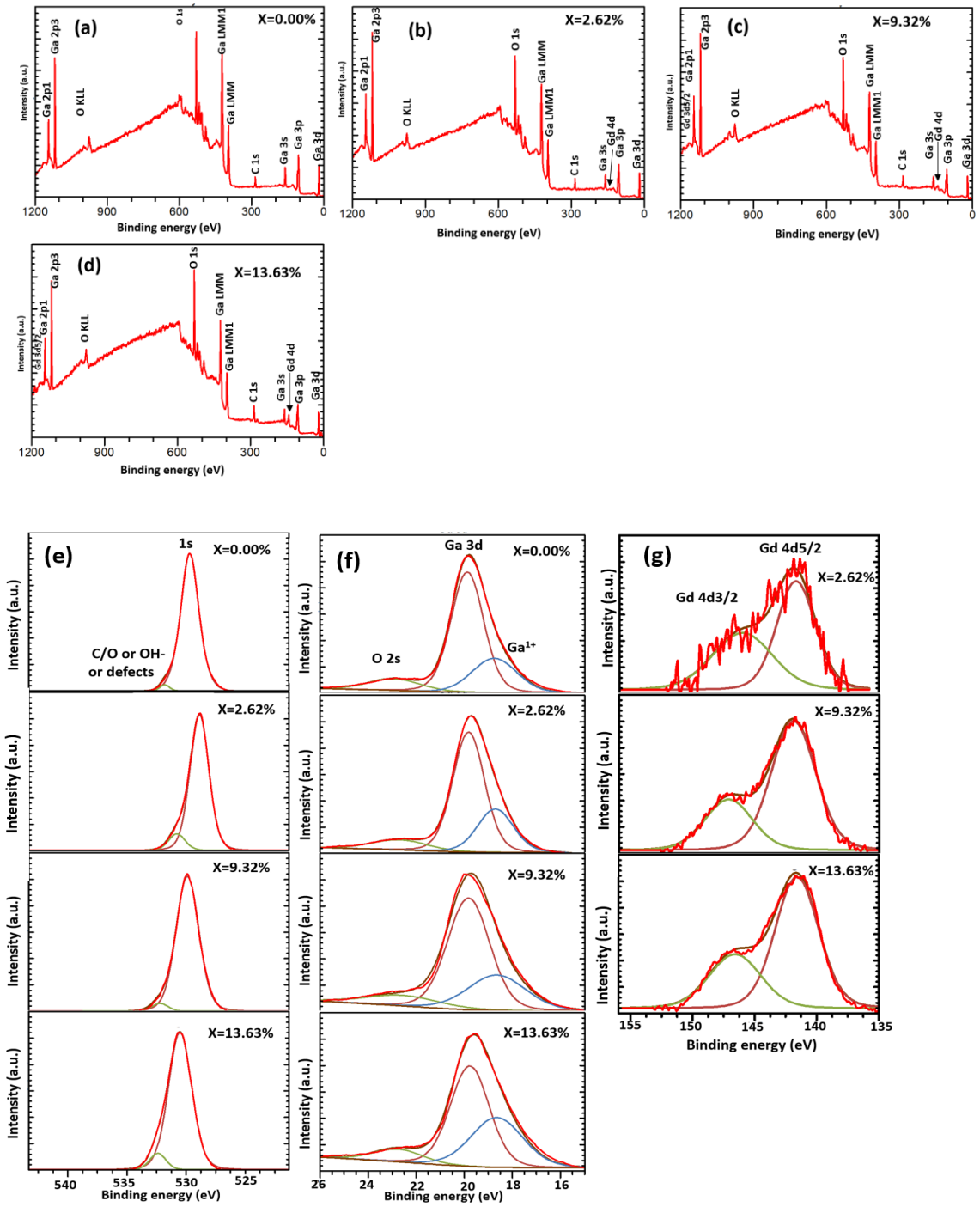

Figure 4.9. (a), (b), (c), (d) Represent survey spectrum and (e), (f), (g) represent O 1s, Ga 3d, Gd 4d, core levels spectra of $(Ga_{(1-x)}Gd_x)_2O_3$ thin films for x= 0.00%, 2.62% 9.32%, 13.63%, respectively.

In the O 1s spectra, the dominant peak is centered at about 530.50 eV (associated with shoulder peaks due defects or C-O or C=O bond or OH^-[210], [211]) for x=0.00, 2.62, 9.32 and 13.62%, respectively. From the area under the shoulder peaks, it is seen that the defects increase with Gd concentrations. The deconvoluted XPS spectra of Ga 3d reveal 3 peaks linked to O 2s, Ga 3d (related to the lattice oxide of Ga_2O_3) and Ga $^{1+}$. The main Ga 3d peak shown in figure 4.9(f), centered around 19.85eV, is shifted slightly to lower binding energy for the samples with increasing Gd concentration, which is associated with the presence higher Ga^{1+}. which is supported by the greater observed area 24%, 26%, 27%, 36.29% under the curve of the Ga^{1+} peak as the Gd concentration increases.

The elemental composition of the $(Ga_{(1-x)}Gd_x)_2O_3$ thin films was measured by energy dispersive spectroscopy (EDS). Figure 4.10 shows the EDS spectrum of thin films for different Gd content (x), where Ga, Gd, O, C are observed. It is clearly seen from the graph that the intensity of the Gd/Ga ratio increases with the Gd content x of $(Ga_{(1-x)}Gd_x)_2O_3$ and estimated atomic percentage of Gd are shown in the inset.

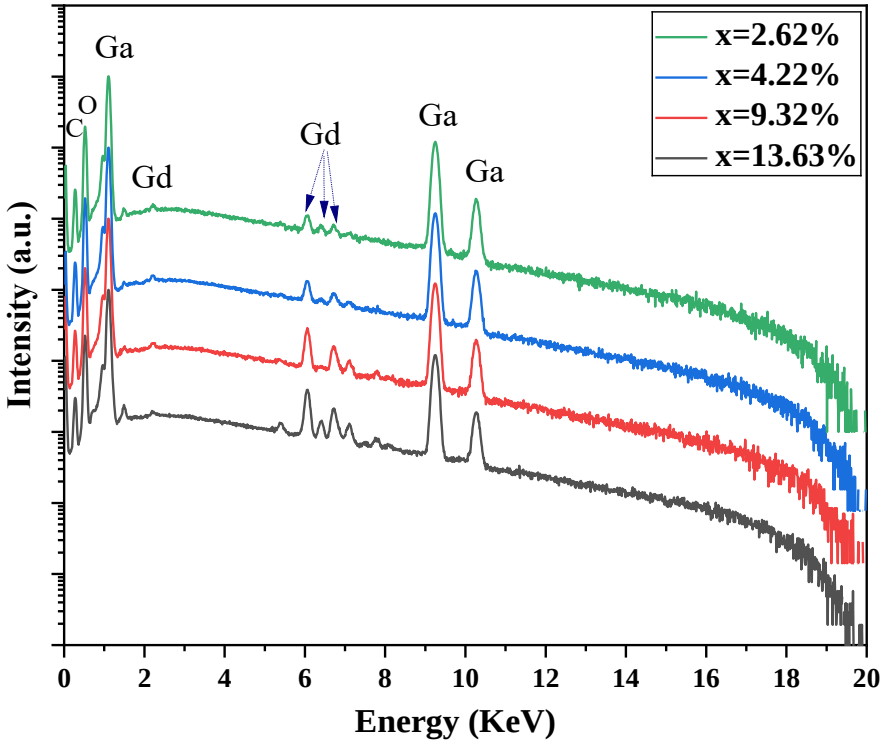

Figure 4.10. EDS measurement of $(Ga_{(1-x)}Gd_x)_2O_3$ thin film for x=2.62%, 4.22%, 9.32%, 13.63%.

5. GROWTH AND CHARACTERIZATION OF $(Ga_{1-x}Fe_x)_2O_3$ TERNARY ALLOY

5.1 Introduction

Semi insulating Ga_2O_3 and its alloys having ultra-wide bandgap (4.6~4.9eV), predicted high breakdown field (6-8MVcm^{-1}), and high electron saturation velocity (2×10^7 cm/s), have been propelling investigations into versatile applications such as gas sensors, transparent conductive oxides for solar cells, UV detectors, magnetic sensors and devices, and high-power electronic devices (including MOSFETs) [212],[213], [214]. It's proven capability of growing high-quality single crystals from melt, offer huge potential for cost effective large scale manufacturing[215]–[217].

Intrinsic β-Ga_2O_3 often suffers from n type conductivity due to the presence of oxygen vacancies or defects in the crystal, consequently, absence of a sharp pinch of current, and high off state drain leakage current [218] in electronic devices is problematic. In lateral field effect transistor application (FET), a key building block is the formation of a high resistivity buffer. Therefore, a highly insulating β-Ga_2O_3 layer achieved through either by doping or alloying for power application is needed. The most common way to achieve highly resistive Ga_2O_3 material is through doping by divalent atoms (Mg^{2+}, Be^{2+}, Zn^{2+} and Fe^{2+}) into the lattice by substituting into trivalent Ga sites [219]–[222]. There have been few studies of the effect of Fe in β-Ga_2O_3. Fe is believed to form deep level acceptor levels which increase the resistivity of the material [223]–[226]. Hence, Fe doping of Ga_2O_3 can be a good candidate for the formation of a homoepitaxial highly insulating crystalline buffer layers or gate dielectrics.

Furthermore, there has been growing interest in Fe doped Ga_2O_3 to achieve diluted magnetic semiconductor oxides for spintronic applications [227]–[231]. The properties of bulk $(Ga_{(1-x)}Fe_x)_2O_3$ prepared by the float zone, sol gel, ball milling, and solid state reaction method have been reported [232], [233], [233]–[236], showing the presence of magnetic properties. In contrast, very few reports of thin films of $Ga_{(1-x)}Fe_x)_2O_3$ are seen in the literature dealing with the magnetic properties [229], [237]–[243]. In addition, most of the past studies of $(Ga_{1-x}Fe_{x)2}O_3$ thin films are presented for high values of x concentration (typically x>0.5). Daoyou Guo et al.[242] showed ferromagnetic properties of monoclinic $Ga_2O_3/(Ga_{1-x}Fe_x)_2O_3$ (x=2.44%) thin film on sapphire substrates. Yuanqi Huang et al. demonstrated ferromagnetism in the cubic structure of Fe stabilized γ-Ga_2O_3 thins film grown on c-plane sapphire substrate and suggested possible application in nonvolatile magnetic storage devices [49]. In addition, ferromagnetism in orthorhombic GaFeO thin films were studied on ITO buffered YSZ(001) [239], $SrTiO_3$(111)[228], and $SrRuO_3$(111) [229]. Ferromagnetism in combination with a transparent semiconductor oxide is promising since ferromagnetic property can be tuned by light [244]–[246]. Furthermore integrating ferromagnetism in optoelectronics devices might be attractive for novel magneto-optical devices[247], [248].

However, extensive studies of $(Ga_{1-x}Fe_x)_2O_3$ thin film alloys as a function of growth conditions and Fe concentration have not been explored in the literature. In this chapter, a systematic investigation of $(Ga_{1-x}Fe_x)_2O_3$ thin films as function of growth parameters will be presented as well as the structural, optical and magnetic properties will be presented and discussed.

5.2 Experiment

Firstly, $(Ga_{1-x}Fe_x)_2O_3$ thin films for x=0.15 were grown at various growth temperatures (400-750^o C) and oxygen pressures (1.3×10^{-5} torr ~2.2×10^{-2} torr) to study the effect of temperature and pressure on the crystallinity and the structure of the thin film. Single sided polished c-plane sapphire substrates were used, which were cleaned ultrasonically using acetone, isopropanol, deionized water and finally dried with nitrogen gas prior to loading them in the deposition system. After growth, each film was annealed at a temperature 50^{o}C above the growth temperature without the presence of oxygen. The targets were fabricated from Ga_2O_3 (99.999%) and Fe_2O_3 (99.999%) with varied Fe (mole ratio of Fe/(Ga:Fe)) concentration. The details of the target fabrication are given in chapter 2(2.2). A krypton fluoride (KrF) excimer laser source having a wavelength 248nm was used to ablate the target onto the substrate. During deposition, the laser pulse frequency was set at 5Hz and the beam was set to an energy density of 2J/cm^2. The rotation of the substrate, target, and the distance between them were carefully controlled to maintain film uniformity and to prevent crater formation on the target.

5.3 Results and Discussions

Figure 5.1 shows the XRD 2θ/ω spectra of $(Ga_{(1-x)}Fe_x)_2O_3$ thin films for x=0.15 as a function of temperature and pressure. Figure 5.1(a) represents partial oxygen pressure dependency, and 5.1(b) is the enlarged regions around the diffraction angle of 38^o. All sample peak positions were compared with the baseline pure β-Ga_2O_3 grown at T=700^{o}C and P=2.2×10^{-2} torr. The peaks at 20.5°, 41.7° and 64.5° correspond to the diffraction peals of the (0003), (0006) and (0009) planes of the sapphire substrate. It is clearly observed that with the decrease of oxygen pressure, the peaks related to the thin

film shift towards lower 2 theta angle, without any degradation of the crystal quality. In addition, the lowest full width half maxima (FWHM) were observed for an O_2 pressure of 1.5×10^{-6} torr. This implies the formation of the gamma (γ) phase, and is confirmed by the pole figure measurement, shown in chapter 6. Calculated FWHM with partial pressure are shown in the figure 5.2 (b) and table 5.1. The peak's positions at 18.59º, 37.81 º, 58.18 º and 80.70 º are due to the diffraction plane of γ (111), γ (222), γ (333) & γ (444) of gamma $Ga_{2-x}Fe_xO_3$, respectively. Similar observations were made by Y. Huang *et al.* [49] who deposited $Ga_{2-x}Fe_xO_3$ thin film for x =0, 5.38, 9.62 at% on (0001) plane of sapphire substrate at a O_2 pressure ~7.5×10^{-8} torr and temperature of 750ºC using PLD. Their films were annealed at 750º C for 1 hours. Figure 5.1 (c) and (d) show the temperature dependence of the XRD spectra of $(Ga_{(1-x)}Fe_x)_2O_3$ thin films for x= 0.15 grown at a O_2 pressure of 2.2×10^{-2} torr. It is seen that for higher growth temperature there is improvement in the crystallinity which is confirmed by calculating FWHM (Table 5.1 and figure 5.2(a)). Interestingly, a low deposition temperature causes the peak to shift to smaller angles having a decreased FWHM, representing an increase of lattice constant. This can be explained by the increasing Fe^{2+}/ Fe^{3+} ratio, because Fe^{2+} (0.74 Å) has larger ionic radius than Fe^{3+} (0.64 Å) and Ga^{2+} (0.62 Å) [66], [249], [250]. This is in good agreement with the results of Y. Huang et al. [226], who studied the temperature and oxygen pressure dependence of $Ga_{1.95}Fe_{0.05}O_3$ thin films and demonstrated using XPS measurements that the presence of Fe^{2+} is higher in low temperature grown samples as compared to the temperature grown samples resulting in the increasing lattice constant. Similarly, the authors also found from X-ray diffraction measurements that with increasing partial oxygen pressure, peaks shift to smaller angle, which was explained by

the XPS measurement. They showed that the increase in the O_2 partial pressure during growth, the main Fe $2p_{3/2}$ peak shift to higher binding energy due to the increase of Fe^{3+} concentration, i.e. increase oxygen pressure causes Fe^{2+} ions to be oxidized into Fe^{3+}. Consequently, the smaller ionic radius shrinks the lattice constant causing the peak position to gradually shift to higher angles. Thus, to estimate the ratio of Fe^{3+}/Fe^{2+} XPS spectra of Fe $2p_{3/2}$ core level were fitted in figure 5.3, for Fe content x=0.15 at partial oxygen pressures 1.0×10^{-1} torr and 1.50×10^{-6} torr. The XPS peak positions were calibrated using C 1s at the binding energy of 284.8eV. It is evident that the Fe $2p_{3/2}$ main peaks can be deconvoluted into Fe^{3+} and Fe^{2+} peaks [251], corresponding to the binding energy around 710.42eV and 709.06 eV for pressure 1.0×10^{-1} torr , and 710.10 and 709.0eV for 1.50×10^{-6} torr, respectively. The ratio of Fe^{3+}/Fe^{2+} is about 2.37 and 1.95 for partial oxygen pressure 1.0×10^{-1} torr 1.50×10^{-6} torr, which confirms that the concentration of Fe^{3+} is higher than the Fe^{2+} , when oxygen pressure increases. In addition to core level peaks Fe $2p_{1/2}$ and Fe $2p_{3/2}$, the satellite peaks observed due to the spin orbit coupling which are indicated by Sat. in the figure 5.3. Satellites (shake down or up) are due to a sudden change in Coulombic potential as the emitted electron passes through the valence band. The differences in satellites peaks in figure 5.3 appears due to the presence of Fe^{3+} [252], [253], [254].

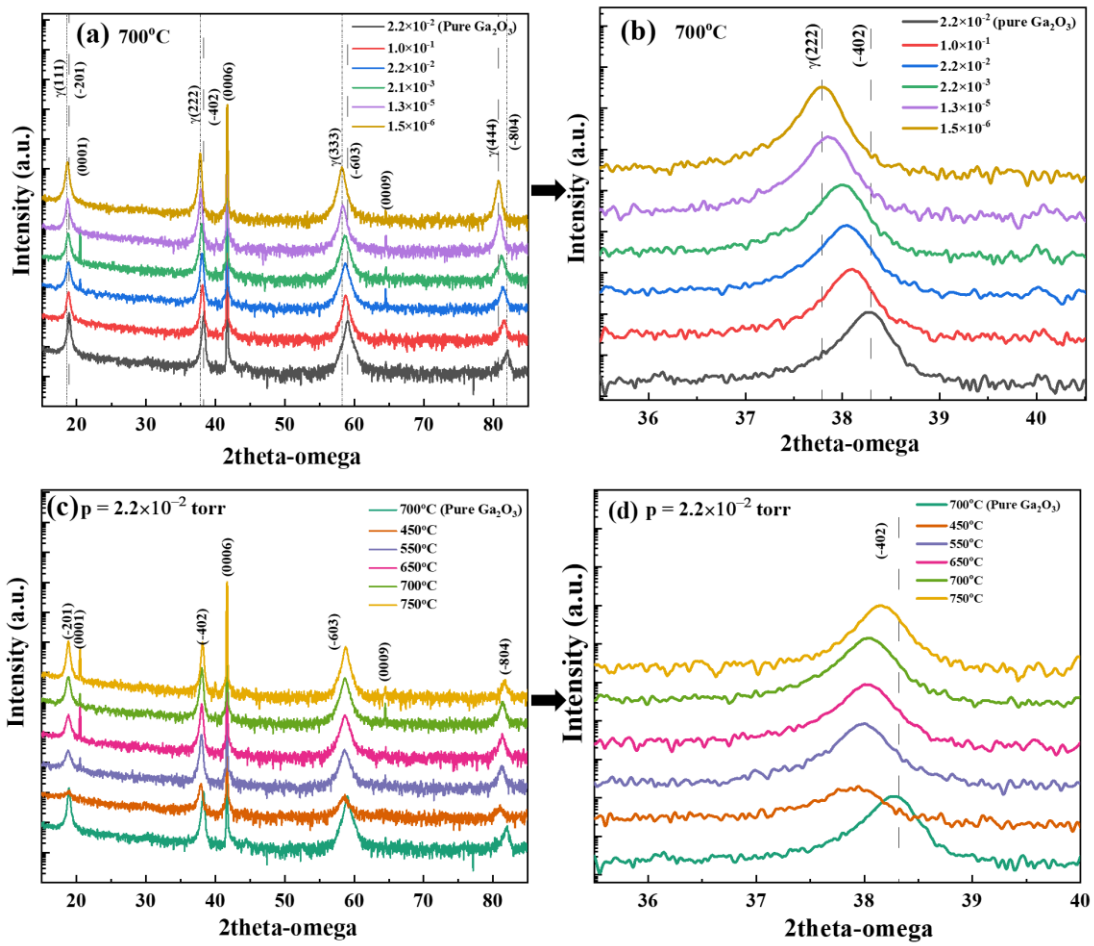

Figure 5.1. 2-theta-omega scan of $(Ga_{(1-x)}Fe_x)_2O_3$ thin films for x=0.15 (a) pressure dependent and (b) corresponding extended region around angle 38°; (c) temperature dependent and (d) corresponding extended region around angle 38°.

Table 5.1. Calculation of FWHM and position of 2 theta around angle 38 degree as function of temperature (left) and pressure (right) for Fe content x=0.15.

Concentration of Fe	Temperature (oC)	2theta	FWHM
x=0.15	450	37.8811	0.4424
x=0.15	550	37.9853	0.3671
x=0.15	650	38.0239	0.3151
x=0.15	700	38.0372	0.3106
x=0.15	750	38.1535	0.2809
x=0.0 (Baseline)	700	38.2654	0.2859

Concentration of Fe	Pressure (torr)	2theta	FWHM
x=0.15	1.00E-01	38.0877	0.2844
x=0.15	2.20E-02	38.0371	0.3144
x=0.15	2.10E-03	37.9882	0.3026
x=0.15	1.30E-05	37.8524	0.2776
x=0.15	1.50E-06	37.7868	0.2455
x=0.0 (Baseline)	2.20E-02	38.2655	0.2836

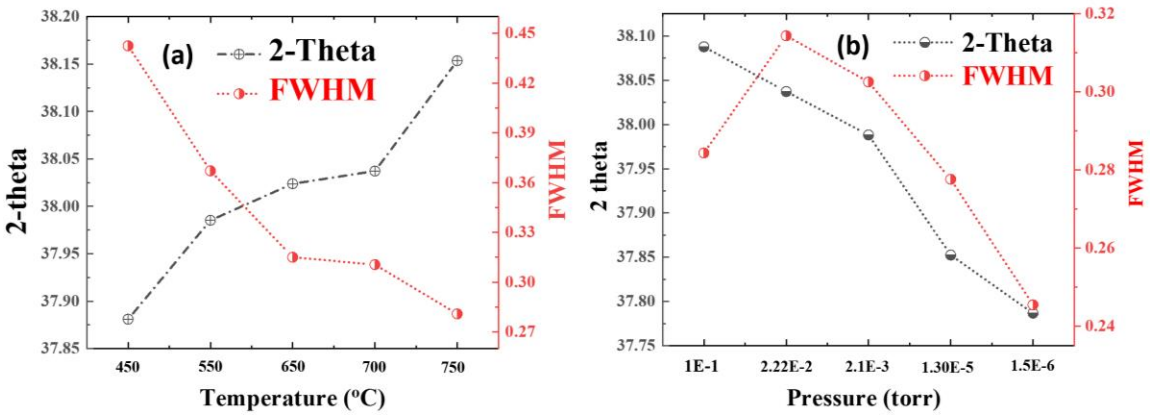

Figure 5.2. (a) Temperature versus FWHM and 2-theta, (b) pressure versus FWHM and 2-theta of $(Ga_{(1-x)}Fe_x)_2O_3$ thin films for x=0.15 .

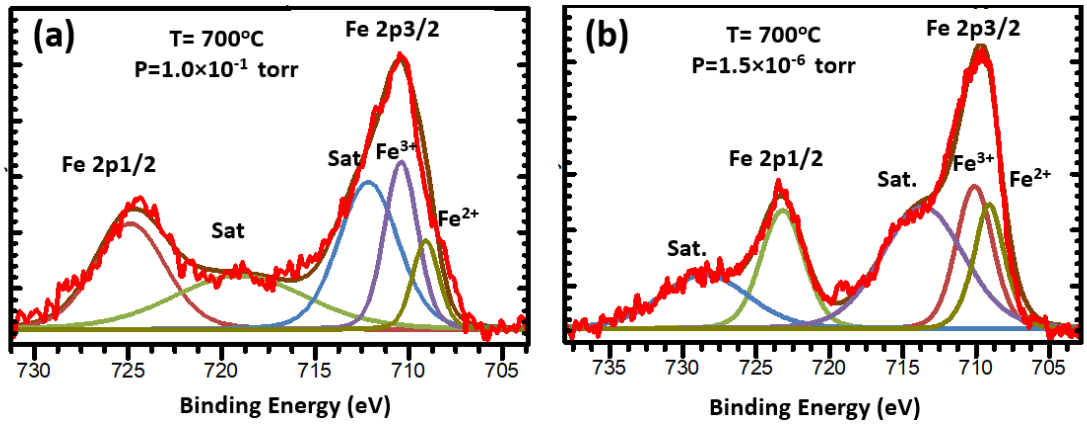

Figure 5.3. Core level Fe 2p XPS spectrum of $(Ga_{(1-x)}Fe_x)_2O_3$ thin films for x=0.15 at a pressure of (a) pressure 1.0×10^{-1} torr (b) 1.50×10^{-6} torr.

From the above assessments, a growth temperature of 700°C and pressure 2.2×10^{-2} torr was chosen for the concentration dependent $(Ga_{(1-x)}Fe_x)_2O_3$ thin film growth. Samples were grown for x= 0.0- 0.50. All samples were subjected to a post deposition annealing at 750° C in the PLD growth chamber after having stopped the flow of oxygen. The XRD plots for these samples are shown in figure 5.4. For x=0.00, the prominent sharp peaks located at 18.90, 38.28, 58.98 and 81.97° represent the Bragg

reflections of the (-201), (-402), (-603) and (-804) planes. The measured spectra confirm for a monoclinic β-Ga_2O_3 thin film that is epitaxially grown on the substrate. Figure 5.4 (b) shows an enlarged view of the patterns around the diffraction angle of 38º for the various samples. This figure shows that with increasing Fe concentration, the (-402) diffraction peak gradually shift to smaller angles, suggesting an expansion of the lattice constants due to an increasing amount of Fe inclusion into Ga_2O_3 lattice sites [255], [256]. However, as clearly seen, increasing Fe content degrades the structural quality of the host materials at these deposition conditions. XRD pole figure measurements (chapter 6) were carried out on $(Ga_{(1-x)}Fe_x)_2O_3$ samples to confirm the crystalline structure. However, it is expected that the spinel phase of the alloys at x=0.40 and 0.50 will co-exist since diffraction peaks appeared at 37.687º, 58.43 º,80.55 º for x=0.40 and 37.617 º , 58.58 º , 80.40 º for x=0.50, matched well with those for the crystal structure reported elsewhere [42], [49], [257] and were indexed as (222), (333) and (444) diffractions plane of the gamma phase of Ga_2O_3, representing the spinel phase of the $(Ga_{(1-x)}Fe_x)_2O_3$ alloy. Missing (111) peaks might be due to the degraded crystal structure, i.e. this temperature and pressure may not be ideal for growing high quality spinel phase. Formation of the gamma phase will be discussed further in section 6 (6.3).

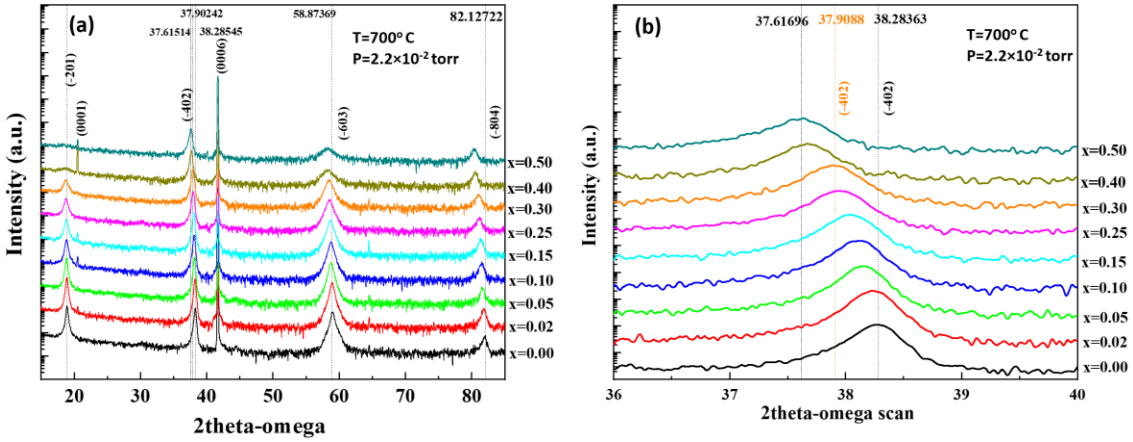

Figure 5.4. X-ray diffraction patterns (a) concentration dependent and (b) expanded view of around angle 38° of thin films $(Ga_{(1-x)}Fe_x)_2O_3$ for x= 0.0,-0.50, grown at 700°C and 2.2×10^{-2} torr.

Figure 5.7 shows the optical transmission spectroscopy spectrum of the $(Ga_{(1-x)}Fe_x)_2O_3$ thin films for x= 0.0~0.50, deposited at 700°C and 2.2×10^{-2} torr. β-Ga_2O_3 shows a high transparency over 90% with no intermediate absorption and the transmission rapidly decreases around 250nm. However, with increased Fe content (x), the absorption edge moves towards longer wavelength with a reduced transmission near the band edge. Films for x=0.40 and x=0.50 showed the lowest optical transparency. In addition, unlike β-Ga_2O_3, intermediate absorption appears in the alloys of $(Ga_{(1-x)}Fe_x)_2O_3$, which implies indirect transition at this thermodynamic condition, consistent with the first principle study done by Hao He et al. [258], who used density functional theory (DFT) and local density approximation (LDA) to calculate the band structure of Fe doped β-Ga_2O_3 to show presence of an intermediate band. The presence of an intermediate bands has potential applications in designing solar cell capable of absorbing photons with lower energy than the bandgap of the original host semiconductor utilizing electron transition from valence band or deep level defect to intermediate band, as well as the conventional

process of transition from valence band to conduction band. In addition, the presence of an intermediate band can be beneficial over the single gap solar cells, as well in application of multi-wavelength photodetectors [259]–[262].

In addition, the structural and electronic properties with Fe content were studied by employing first-principles calculation based on density functional theory (DFT) [263]. The calculated band structure and density of states (DOS) of the pristine β-Ga_2O_3 under Generalized Gradient Approximation (GGA) + modified Becke-Johnson potential (mBJ) are shown in figure 5.5. The bandgap obtained from this calculation is about 4.25eV (direct) and 4.19 eV (indirect). The band structure of β-Ga_2O_3 consists of a flat valence band, indicating a large hole effective mass, which implies a low hole mobility and poses a challenge to fabricated p type β-Ga_2O_3. From the density of state (DOS) result, the bandgap consists of contributions from Ga(s), Ga(p), Ga(d) and O(s) orbitals. To check the electronic properties of the monoclinic β-Ga_2O_3 alloy, Fe atoms were added in the $(Ga_{(1-x)}Fe_x)_2O_3$ structure from 0.0 to 50%. The results suggest that the incorporation of Fe into the lattice causes the volume of the unit cell to increase while at the same time the bandgap shrinks. Figure 5.6 shows the effect of a 50% Fe incorporation on the electronic structure resulting in a calculated bandgap of 3.84 eV. The reduction of the bandgap is consistent with the experimental optical transmission data shown in figure 5.7.

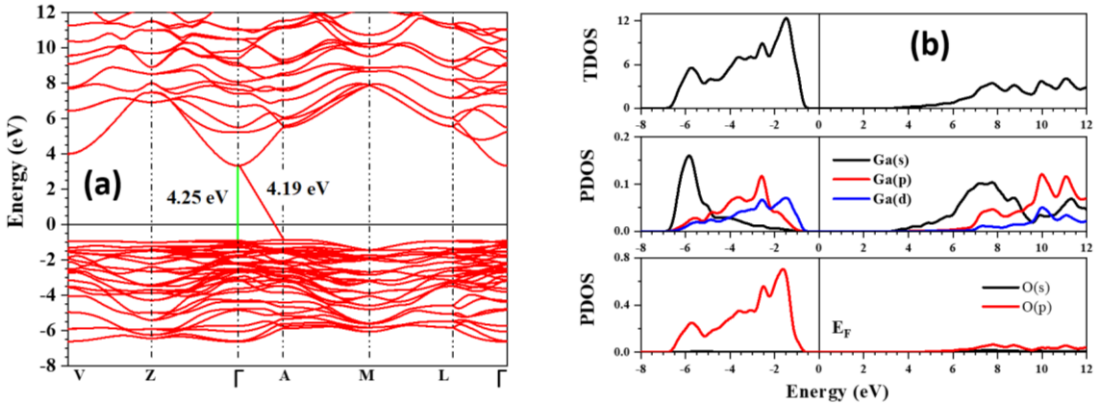

Figure 5.5. Band structure (a) and Total (T) and Partial Density of States (PDOS) (b) of pristine monoclinic Ga_2O_3 along high symmetry lines of the Brillouin zone, as obtained using first principles DFT simulations (with the GGA+mBJ approximation for the exchange-correlation functional) [263]. Fermi energy is placed at zero of energy. Direct and indirect band gaps are indicated in (a).

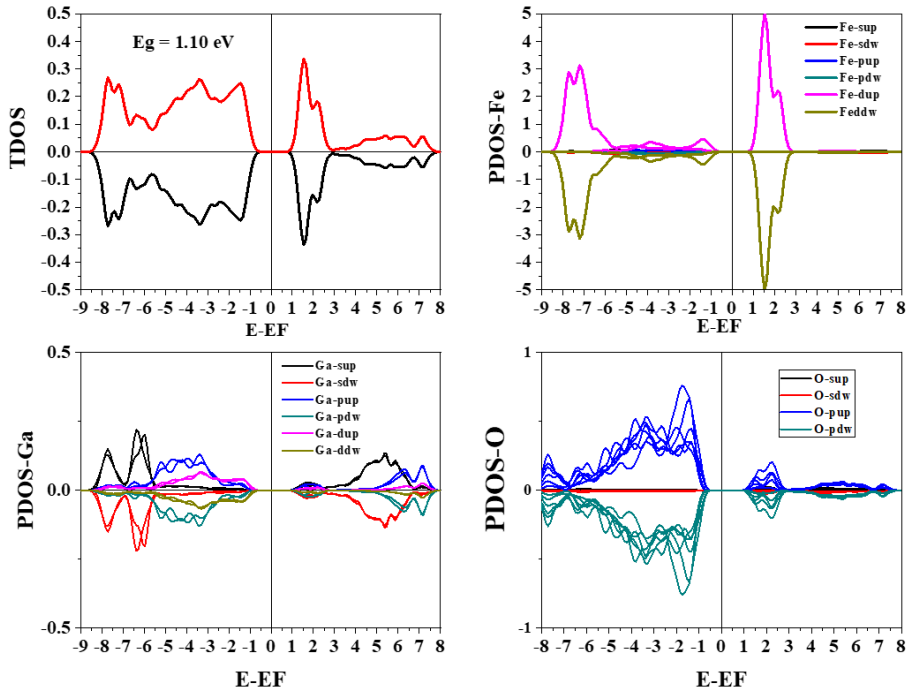

Figure 5.6. Total (T) and Partial Density of States (PDOS) per atom for Fe-doped monoclinic Ga_2O_3, with Fe concentration of 50 %, as obtained using first principles DFT simulations (with the GGA+U approximation for the exchange-correlation functional) [263]. Fermi energy is placed at the energy zero. Arbitrary units for density of states and energies are in eV.

To estimate the direct and indirect bandgap the Tauc equation $(\alpha h\nu)^{1/n} = B(h\nu - Eg)$ was used, where n=1/2 and 2 for determining the direct and indirect energy band transition, hυ is the photon energy, α is the absorption coefficient and B is a constant.

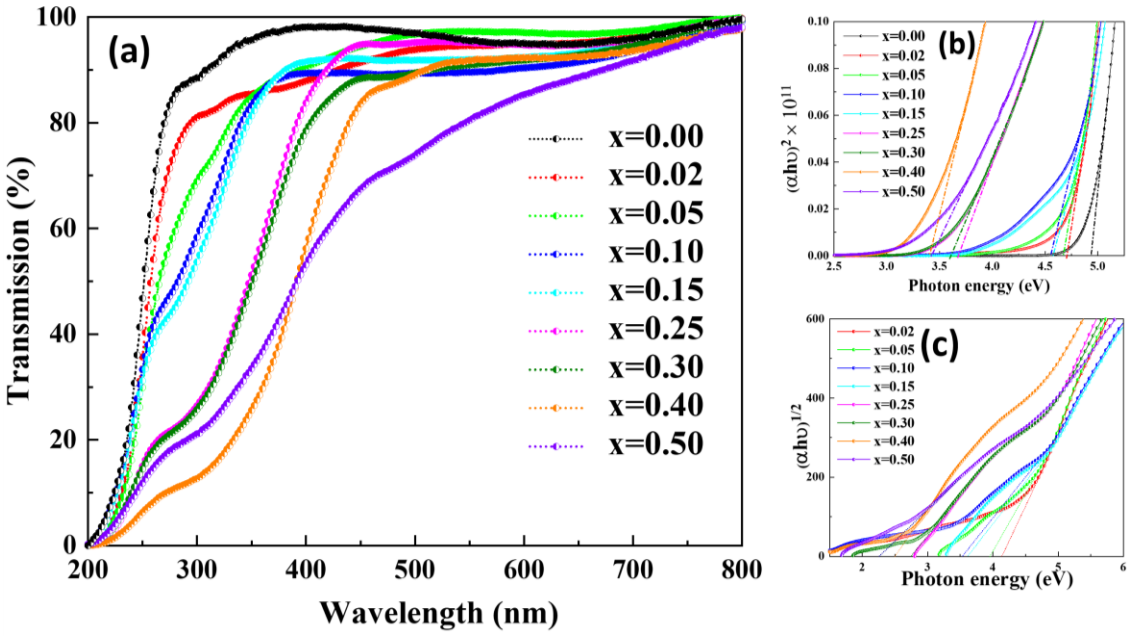

Figure 5.7. (a) Optical transmission spectroscopy, (b) and (c) are Tauc plots for direct and indirect transition for $(Ga_{(1-x)}Fe_x)_2O_3$ thin films for x= 0.0-0.50, respectively.

To calculate thickness and roughness and investigate further the optical properties of the thin films, spectroscopic ellipsometry was carried out on the as-grown samples. The extracted parameters are shown in table 5.2 and figure 5.8. In general, the thin films have some region of optical transparency, i.e. vanishing imaginary part where the extinction coefficient approaches k=0. This transparent region can be analyzed to extract n and the thickness of the film by the Cauchy Sellmeier equation (17) [202].

$$n(\lambda) = a + \frac{b}{\lambda^2} + \frac{c}{\lambda^4} \quad (17)$$

where n is refractive index, λ is wavelength, and a, b, c optical constants. Therefore, to determine the thickness and refraction index (at 632nm), data sets were evaluated using the Cauchy function in the transparent spectral region. After that a B-spline analysis was used to obtain the optical parameters of the absorbing film for x=0.40 and x=0.50, (as the absorption edges shifted above 400nm) where Kramers-Kronig (KK) relationship were maintained by evaluating values of extinction coefficient k, refractive index n. From figure 5.6, it is seen that the extinction coefficient is almost zero for all sample up to 400nm but for x=0.40 and 0.50 strong absorption appears at shorter wavelength, indicating bandgap shrinkage. The appearance of a dip in the spectrum around 450nm can be attributed to absorption due to the defects or intermediate band. It is also evident that the refraction index increases with Fe content. For x= 0.4 and 0.5 the estimated refraction index at 632nm are 2.1857 and 2.2494 respectively These values are greater than the refraction index (1.89~1.95) [264]–[267] of ß-Ga_2O_3. However, the refraction index of gamma gallium oxide in the visible region which is reported to be 2.0~2.1[268], closely matches the value obtained from the ellipsometry data, confirming the alloy structure is most likely the gamma phase.

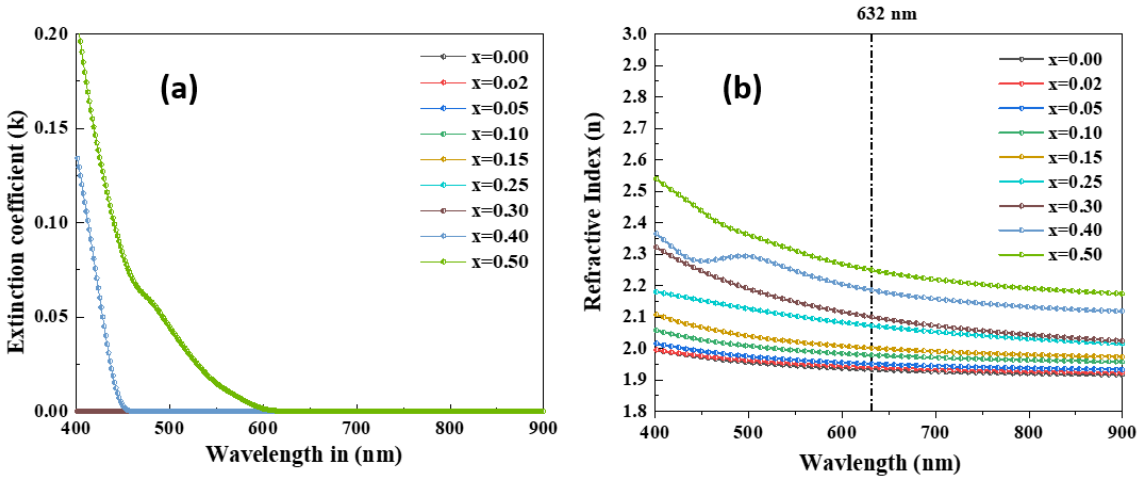

Figure 5.8. (a) Extinction coefficient and (b) refractive index as function of wavelength for $(Ga_{(1-x)}Fe_x)_2O_3$ thin films for Fe content x= 0.0-0.50.

The influence of Fe content on the surface morphologies and roughness of the films was examined using scanning atomic force microscopy (AFM). Results are shown in figures 5.9 and 5.10. The films appearance is granular in nature with the high densities on the sapphire substrate, which made it uniform in appearance. The surface topologies or grains size are likely related to Fe content and changes from circular to elongated rice like granules as the Fe content increases suggesting a directional dependence ad-atom migration on the surface. Thus, the changing the surface morphologies with Fe content is most likely related to a change of mobility or energy of ad-atoms at this growth temperature. Increasing the growth temperatures will most likely increase the migration of the species and will probably decrease the surface roughness. The decrease in the rms values and the grain size with increasing Fe content is probably due to a decrease in the surface adatom migration in the presence of Fe and/or lack of oxygen with the increasing Fe content which pins the grain boundaries and limits the adatom mobility.

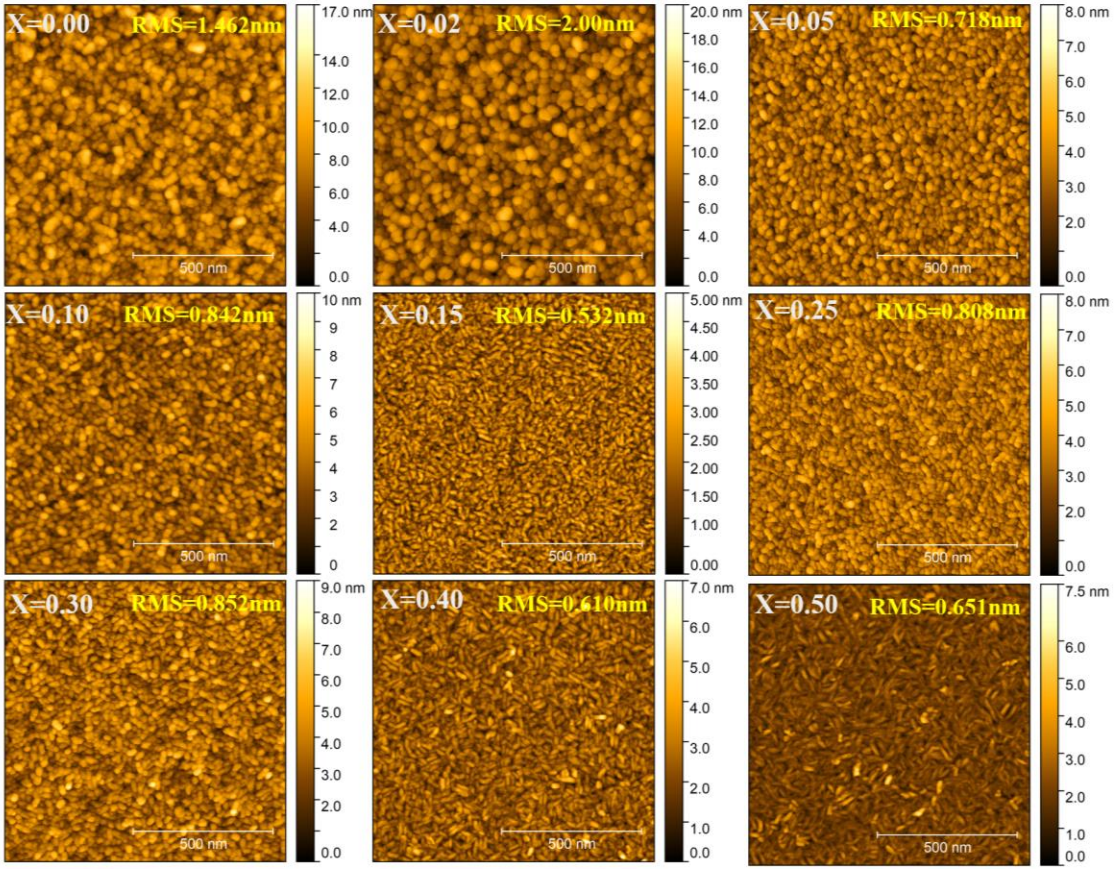

Figure 5.9. AFM (1um×1um) surface images for different Fe content in the $(Ga_{(1-x)}Fe_x)_2O_3$ alloy grown at 700ºC and 2.2×10^{-2} torr.

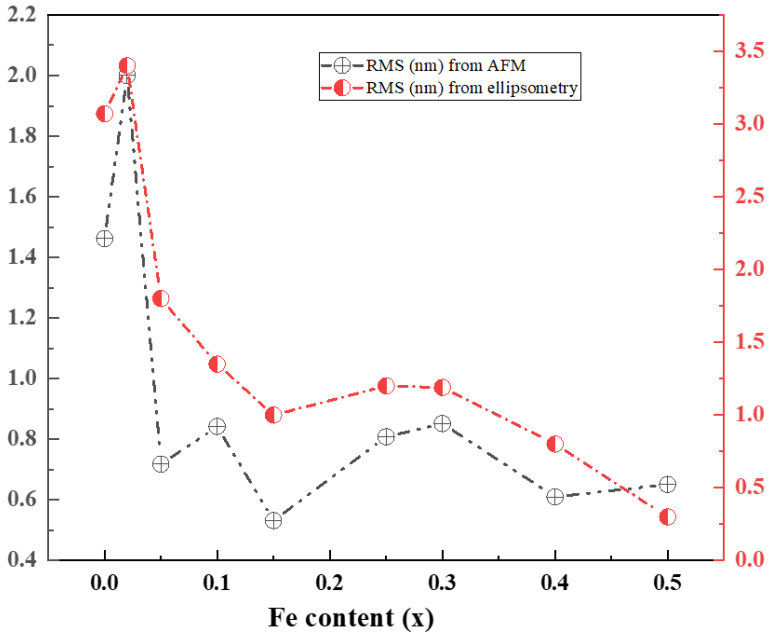

Figure 5.10. Dependence of roughness of $(Ga_{(1-x)}Fe_x)_2O_3$ thin films on Fe content (x) determined from ellipsometry and AFM.

Table 5.2. Materials properties of $(Ga_{1-x}Fe_x)_2O_3$ at pressure 2.2×10^{-2} torr and temperature 700°C.

Fe content (x)	Thickness (nm)	Bandgap (eV) from UV-vis		Refractive index at 632nm	Roughness from Ellipsometer (nm)	RMS Roughness using AFM (nm)
		Direct	Indirect			
0.00	106.48	4.93	4.39	1.9330	3.070	1.462
0.02	131.22	4.71	4.14	1.9406	3.400	2.000
0.05	143.19	4.67	3.96	1.9508	1.800	0.718
0.10	96.930	4.56	3.54	1.9790	1.350	0.842
0.15	82.920	4.58	3.62	2.0012	1.000	0.532
0.25	94.640	3.68	2.78	2.0724	1.200	0.808
0.30	80.540	3.60	2.75	2.1001	1.190	0.852
0.40	95.070	3.40	2.50	2.1857	0.800	0.610
0.50	52.770	3.43	2.25	2.2494	0.300	0.651

Finally, to investigate the magnetic properties of the $(Ga_{(1-x)}Fe_x)_2O_3$ alloys, a vibrating sample magnetometer (VSM) was used. Figure 5.11 shows the magnetization versus magnetic field (M-H) of $(Ga_{1-x}Fe_x)_2O_3$ for the x = 0.0, 0.02 thin films having thicknesses of 106.48nm and 131.22nm, respectively. Diamagnetic contributions due to

the sapphire substrates and sample holder rod were subtracted from the raw data. β-Ga_2O_3 demonstrates paramagnetic behavior, while for an Fe content x=0.02 the alloy shows ferromagnetic behavior at room temperature as conclude from the observed hysteresis. The calculated magnetic saturation, remanence and coercivity are 4.67 emu/cm^3 , 0.8769 emu/cm^3 and 56.159 (Oe) respectively. Fe doped magnetic properties of multilayer $Ga_2O_3/(Ga_{1-x}Fe_x)_2O_3$, (x=2.44%) thin films were studied by Daoyou Guo et al [242]. They found a much larger magnetic saturation (32.8 emu/cm^3) than our experimental values (4.67 emu/cm^3). The origin of the magnetic properties is not clearly understood. Besides, the magnetic properties in thin films Ga_2O_3 with other element doping, for example Mn, Cr, has been reported elsewhere [257], [269]. This study presents $(Ga_{1-x}Fe_x)_2O_3$ as a potential candidate for future spintronic applications capable of working at RT.

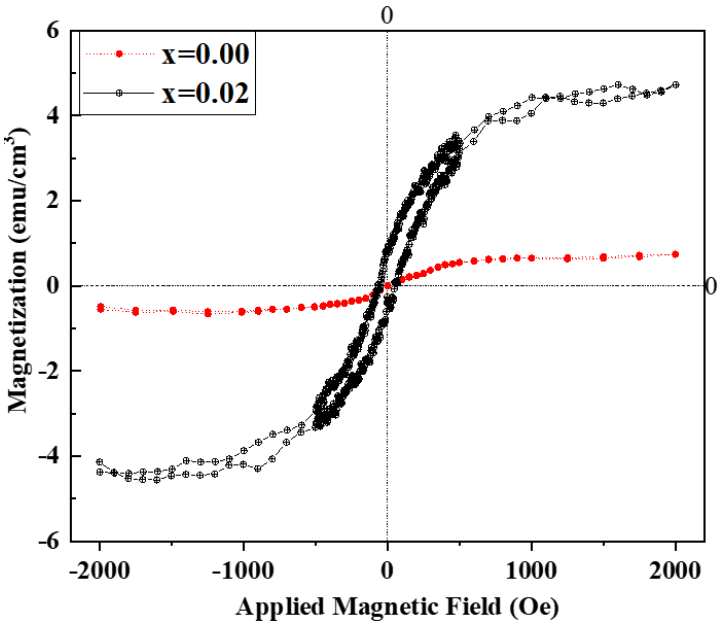

Figure 5.11. M-H Curve of $(Ga_{(1-x)}Fe_x)_2O_3$ thin films for Fe content x=0.00, 0.02 taken at room temperature.

6. SPINEL $(Ga_{1-x}Fe_x)_2O_3$ THIN FILMS: GROWTH AND CHARACTERIZATION

6.1 Introduction

There has been growing interest in the field of wide bandgap diluted magnetic semiconductor oxide (DMS) to increase the versatility of its application for example magneto-optics, spintronics etc. through dopant-spin, carrier spin interaction and defects [270]–[272]. With a reported electrical breakdown voltage of 8 MeV/cm and a bandgap of 4.5~5.3 eV for Ga_2O_3 [273], [274] this material is an ideal candidate for fabricating transparent magnetic optoelectronic devices [66], [257] when alloyed with magnetic elements such as Fe and Co.

There are relatively few reports of this material system exhibiting ferromagnetic properties at room temperature. These include $(Ga_{1-x}Mn_x)_2O_3$ [257], [275] multilayer $Ga_2O_3/(Ga_{1-x}Fe_x)_2O_3$ [66], $(Ga_{1-x}Fe_x)_2O_3$ for $x < 0.1$ [49] as well as epitaxial $Ga_{0.6}Fe_{1.4}O_3$ [276] thin films that was deposited on different cubic substrates using pulsed laser deposition.

H.J. Van Hook et al. [277] have also studied the thermal stability of gallium orthoferrite in the system Fe_2O_3-FeO-Ga_2O_3. They found this compound demonstrates a wide range Ga:Fe ratio on both sides of the stoichiometric $GaFeO_3$, with oxygen losses being extensive in the spinel structure.

Though, β-Ga_2O_3 has been extensively explored, research into the other phases including γ- Ga_2O_3[278], ε- Ga_2O_3 [116], [279], δ- Ga_2O_3[280] and α-Ga_2O_3[278]are scantily studied as they are metastable . Recently these phase are being investigated for their versatility in applications since they may possess wide-bandgap and other properties

that makes them conducive for applications in optoelectronics (solar blind photodetectors, phosphor and electroluminescent devices, solar cell), power electronics (MOSFET, Schottky barrier diodes), memory devices (resistive random access memory, spintronics application), sensing devices applications (nuclear radiation detector and gas sensor), deep UV transparent conductive oxide electrode and photocatalyst [93], [94]. Various techniques are being explored to stabilize these metastable structures including doping and alloying with various cations. The γ-phase has a spinel structure that is important for ferromagnetic applications. Alloys of Ga_2O_3 with Mn, Fe , Cu have been found to stabilized in the γ-phase which have been studied for potential use in optoelectronics and ferromagnetic applications. For example, Qi Liu et al. [95] studied the metastable γ-phase in Ga_2O_3 thin films by Cu doping through sol gel process followed by annealing at 700°C in a nitrogen atmosphere. The Cu doped γ phase was found to transform into the monoclinic β-phase when a high annealing temperature process above 800° C was performed. They also showed the Cu doped γ-phase bandgap transmission spectrum displays a red-shift indicating that Cu-doping has an effect on the bandgap which varied between 4.90 to 4.38 eV depending on doping concentration. More importantly, they were able to demonstrate that photoluminescence in the UV and blue region of the spectrum was stronger in Cu doped γ- Ga_2O_3 thin films than in pure β-Ga_2O_3. Rong Huang et al. also reported Mn doped spinel γ-Ga_2O_3 grown on sapphire (0001) substrate using PLD at temperature 450°C and partial oxygen pressure of 3.8×10^{-4} torr. demonstrated ferromagnetism at room temperature [43]. Fe doped stabilized γ-Ga_2O_3 thin films were obtained by Yuanqi et al. [49]. They were able to deposit $Ga_{2-x}Fe_xO_3$ thin films for x<10% on the c-plane of α-Al_2O_3 substrate. These authors suggested from

the point of theoretical and experimental studies that stable Fe doped γ-Ga_2O_3 magnetic thin films can be promising candidates for application in spintronics devices operating at room temperature.

By developing a growth technique to grow high quality alloys of Fe_2O_3-Ga_2O_3, the potential for this material system can be fully explored. Therefore, it is meaningful to understand the crystal structure and the growth and characteristics of $(Ga_{1-x}Fe_x)_2O_3$ thin films. In this chapter, the epitaxial growth of $(Ga_{1-x}Fe_x)_2O_3$ thin films on (0001) oriented Al_2O_3 substrate and a systematic analysis of the structural, optical, surface morphology and magnetic properties will be reported. In addition, the effect of deposition conditions that contribute to phase transformation will be discussed. To the best of my knowledge, an extensive study of the $(Ga_{1-x}Fe_x)_2O_3$ system does not exist .

6.2 Experiment

$(Ga_{1-x}Fe_x)_2O_3$ for x = 0 - 0.75 thin films were grown on (0001) plane sapphire substrate with a partial O_2 pressure of 1.5×10^{-6} torr at a temperature 700° C by PLD. After growth, each sample was annealed for 15 minutes at 750° C in the absence of oxygen. Fe doped Ga_2O_3 targets with different concentrations were prepared using the standard solid-state reaction method described previously in chapter 2 (section 2.4). Thin films were deposited by pulsed laser deposition. The laser ablation was carried out using a Krypton Fluoride (KrF) excimer having a wavelength of 248nm with an energy density $2J/cm^2$ and a frequency of 5Hz. The plume on the target was carefully controlled for optimum film quality. Energy dispersive spectroscopy (EDS) was used to determine Fe concentration while XRD and PF-measurements were used to analyze the crystalline properties and phase transformation. Surface morphology was studied using atomic force

microscopy (AFM). The chemical environment and oxidation states of the elements were examined using an Omicron Scienta X-ray photoelectron spectroscopy (XPS) system having a monochromatic Al X-ray source. The optical properties were measured using a Shimadzu UV-2600 spectrometer and a J.A Woollam M-2000 ellipsometer. Finally, the magnetic properties were investigated using a MicroSense vibrating sample magnetometer (VSM).

6.3 Results and discussions

Figure 6.1 (a), and (b) show the high resolution XRD 2ɵ-ω scans of the $(Ga_{1-x}Fe_x)_2O_3$ thin films for different Fe concentrations (x). The peaks at 20.5°, 41.7° and 64.5° corresponds to the (0003), (0006) and (0009) diffraction planes of sapphire substrate. For x=0, sharp peaks at 18.89, 38.23, 59.00 and 81.83^o represent the Bragg reflections planes (-201), (-402), (-603) and (-804) of an epitaxially grown film of β-Ga_2O_3. As the Fe content (x) increases, the diffraction peaks shift toward lower angles inducing remarkable changes in the structural properties. This change can be attributed to Fe incorporation into Ga lattice sites (ionic radius of Ga^{3+}, Fe^{3+} and Fe^{2+} are 0.62, 0.64, and 0.74 Å respectively [66], [249], [250]). Furthermore, the d spacing were calculated by Bragg's equation $2d_{hkl}\sin\theta=n\lambda$ (where d is the lattice spacing, θ is incident angle between the crystal plane and X-ray, λ is X-ray wavelength and n is order) from the position of the (-402) diffraction peak. The calculated values are shown in table 6.1 and plotted in figure 6.7(d), that shows interplanar distance (d) increases almost linearly with Fe concentration. The interplanar distance is defined as the distance of two parallel planes which is shown in figure 6.3 (a). For x=0.1 to 0.75, the observed peaks of the grown films can be attributed to the spinel structure. These films have a (111) orientation along

the growth direction. For x<0.1 the observed peaks can be assigned to a (-201) oriented monoclinic structure. The monoclinic $(Ga_{1-x}Fe_x)_2O_3$ thin film formed on the c-plane substrate with the (-201) plane is parallel to the (0001) plane of sapphire substrate. In contrast, the epitaxial relationship of the cubic or spinel $(Ga_{1-x}Fe_x)_2O_3$ phase is (111) γ-$(Ga_{1-x}Fe_x)_2O_3$ $\|(0001)_{Al2O3.}$ Figure 6.3 shows positional relationship between the monoclinic phase and cubic phase with respect to the hexagonal substrate. Thus, to confirm the phase transformation a semi spherical pole figure measurement is performed by simultaneously rotating the sample across two preferred axes: chi (tilt angle) and phi (in plane rotation) as plotted in figure 6.4. In the pole figure measurement, by changing the chi and phi angles of the sample while setting the incident and detection angles at the diffraction angle of θ, a diffraction intensity distribution is collected. This intensity distribution is projected from the top of the hemisphere as depicted in figure 6.2.

As suggested in the literature [49] there should be only one peak around 2θ=30.5°, which can be assigned to (220) plane of cubic structure, while several diffractions for example (-401), (002) and (-202) for β-$Ga_2O_{3.}$ Before taking measurement, the diffraction angle was optimized at 2θ = 29.5° and then by changing the in-plane rotation angle (0~360°) and tilt angle (0~90°) diffraction intensity distribution was obtained. It is seen that there are six-fold symmetry for x=0.00, and 0.02 at tilt angle 35° and 66°, they can be attributed to the Bragg's plane (-400) and (-401), respectively. For x=0.00, a high diffraction intensity is observed while x=0.02 shows a textured intensity, indicating a deterioration of the crystallinity. For x=0.10, no diffraction peak appeared at angle 35° and 66°, however, diffraction peak begins to be seen at a tilt angle around 55°, which is assigned to the angle for the (220) plane of the of

cubic γ-$(Ga_{1-x}Fe_x)_2O_3$ structure . For higher Fe content (x = 0.15, 0.40, 0.75) clear diffraction peaks are observed at the tilt angle of 55°, which are separated by an angle of 60° confirming the spinel structure. This agrees well with the reported literature elsewhere[49] in which the authors examined the phase transformation, from the monoclinic to the cubic phase during the PLD growth of $Ga_{2-x}Fe_xO_3$ thin films on sapphire substrate, through the use of XRD pole figure measurements for x < 0.10. They set the detector angle 2θ=30.5° and rotated phi angle (0~360°C) and tilt angle (0~90° C) to obtain intensity distribution. They found 6-fold symmetry for Fe doped monoclinic $Ga_{2-x}Fe_xO_3$ (for x=5.38%) at tilt angles of 25° and 55°, as well as observed 6-fold symmetry (for x=9.62%) at a tilt angle of 35° corresponds to (220) plane of the cubic system.

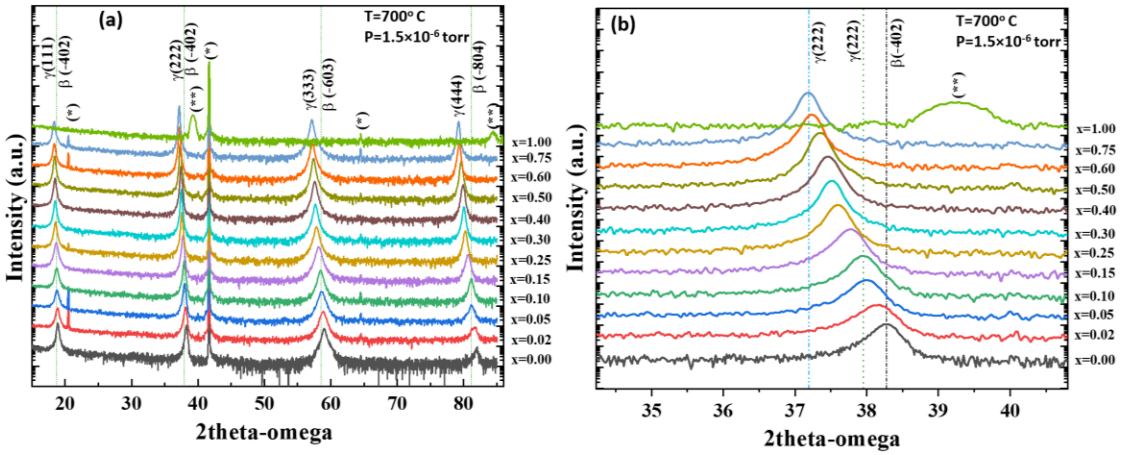

Figure 6.1. **(a)** 2ɵ-ω XRD spectrum of $(Ga_{(1-x)}Fe_x)_2O_3$ for x=0, -0.75 **(b)** Extended view of 2ɵ-ω scan around (-402) plane.

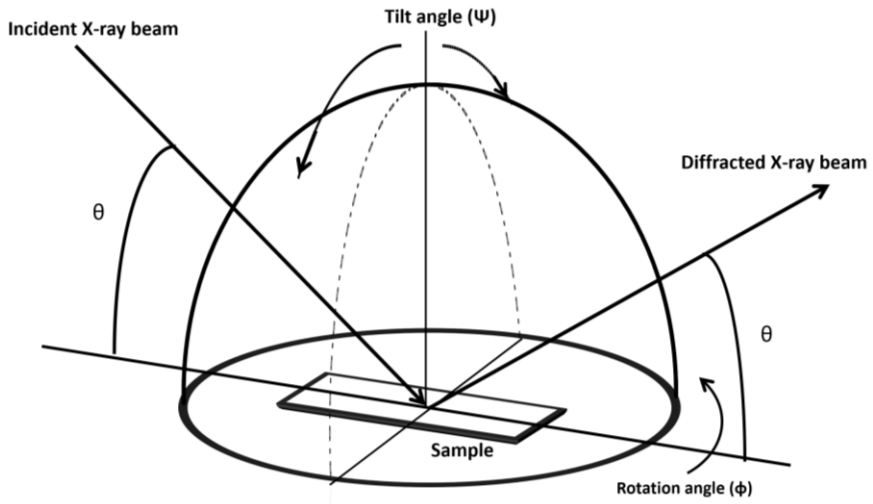

Figure 6.2. Optical arrangement of pole figure measurement for $(Ga_{(1-x)}Fe_x)_2O_3$ thin films.

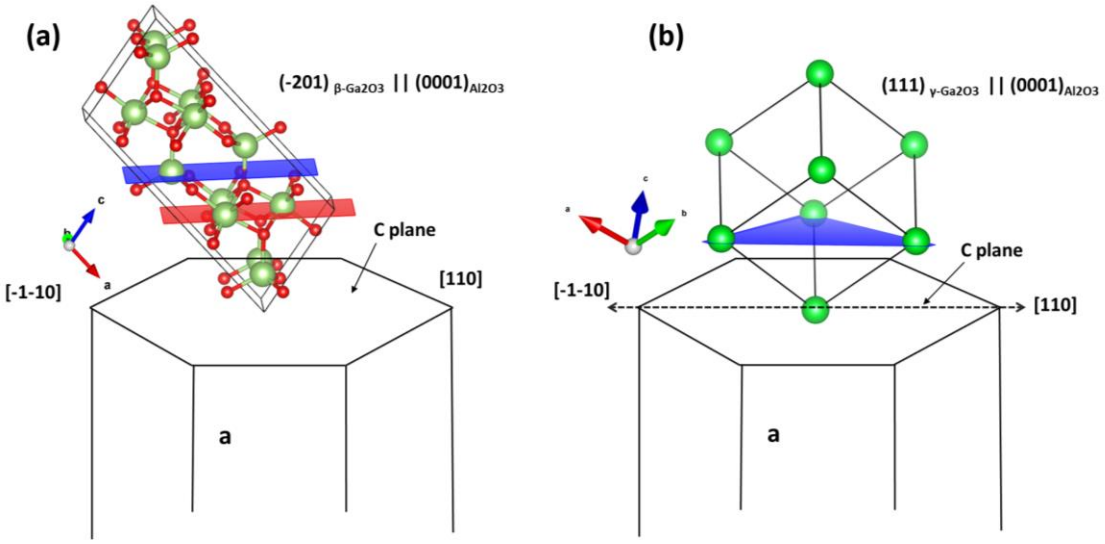

Figure 6.3. Orientation relationship of (a) (-201) oriented monoclinic $(Ga_{(1-x)}Fe_x)_2O_3$ phase, and (b) cubic phase with respect to (0001) plane sapphire substrate.

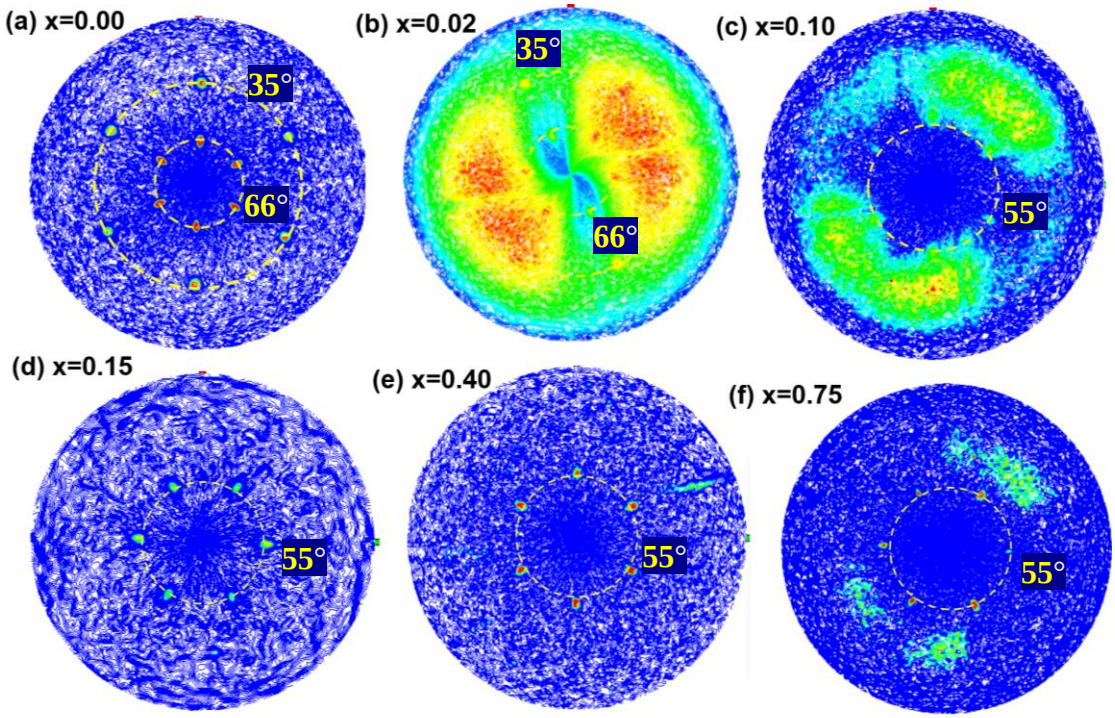

Figure 6.4. X-ray pole figure measurement of $(Ga_{(1-x)}Fe_x)_2O_3$ thin films for different Fe content (x) on (0001) plane of sapphire substrate, all sample were grown at temperature 700^{o}C and pressure 1.5×10^{-6} torr.

It is observed from XRD spectra as well as the pole figure analysis that the spinel structure and crystallinity depend on Fe the concentration. A degraded crystalline quality was detected for films with Fe concentrations from 0.02-0.1, which is obvious from the XRD spectrum, as well as pole figure measurement. Figure 6.4(b) and (c) reveal the presence of texture in the films; an indication of lower quality crystalline films that is probably due to the coexistence of both the monoclinic and spinel phases. Besides Fe, the oxygen pressure also has a substantial impact on the crystallinity as has been shown in chapter 5, figure 5.1(b), where improved crystalline quality is seen with low partial oxygen pressure. Furthermore, the variation of the band structure at this thermodynamic condition for varied oxygen pressure are reinforced by taking the UV vis transmission

measurement of thin films with Fe content of 15% as shown in figure 6.5. It is seen that at high oxygen pressure, the bandgap diminishes, and an intermediate band is observed, which vanishes as the oxygen pressure is reduced to 1.50×10^{-6} torr. This suggest that a deficiency in oxygen during growth facilitates a band structure in the ($Ga_{2-x}Fe_xO_3$) system [277] that does not possess an intermediate band. The reason behind it is the increase of defect density states due excess partial oxygen pressure [281]–[283]. Similar observations were reported for pure ß-(Ga_2O_3) [284].

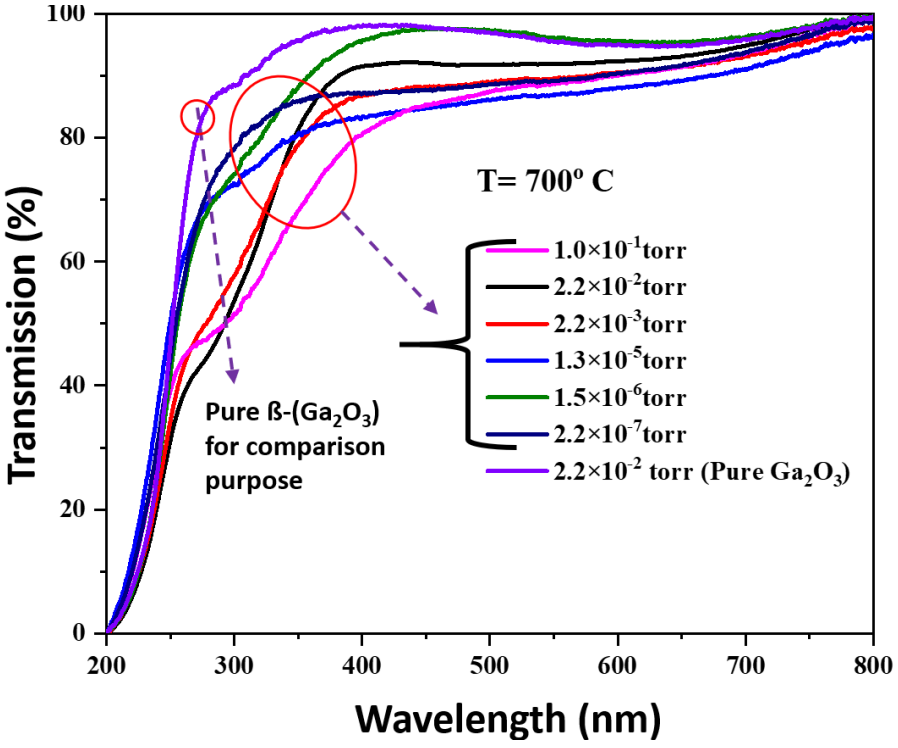

Figure 6.5. Transmission spectroscopy of $(Ga_{(1-x)}Fe_x)_2O_3$ thin films for x=0.15 for variable oxygen pressure, and fixed temperature 700° C.

Table 6.1. Calculated lattice parameter from XRD diffraction scan and FWHM for $(Ga_{1-x}Fe_x)_2O_3$ thin films grown at temperature 700°C and pressure 1.5×10^{-6} torr.

Fe Concentration, x	a (Å)	b (Å)	c (Å)	V (Å^3)	d spacing	FWHM
0.00	-	-	-	-	2.34828	0.2664
0.02	-	-	-	-	2.35627	0.3864
0.05	-	-	-	-	2.36531	0.2805
0.10	8.1347	8.1347	8.1347	538.3003	2.36891	0.2976
0.15	8.1624	8.1624	8.1624	543.8181	2.37886	0.2828
0.25	8.1937	8.1937	8.1937	550.0981	2.39037	0.2316
0.30	8.2062	8.2062	8.2062	552.6196	2.39543	0.2044
0.40	8.2406	8.2406	8.2406	559.5984	2.39848	0.2192
0.50	8.2805	8.2805	8.2805	567.7664	2.40572	0.2059
0.60	8.2980	8.2980	8.2980	571.3737	2.41272	0.2046
0.75	8.3086	8.3086	8.3086	573.5662	2.41549	0.2001

Scanning Probe microscopy (Bruker Dimension ICON) was used in the AFM mode to investigate the surface morphology as shown in figure 6.6. 1×1 μm^2 AFM images were taken at a scanning frequency of 1 Hz. Results show considerable surface changes with increasing Fe concentration, with relatively low root mean square (RMS) roughness for higher Fe concentrations. Formation of some distinct large grains is obvious at higher Fe content (x = 0.25,~0.60) suggesting that Fe can modify the surface migration of the adatoms during deposition. Thus, it is seen that surface morphology and grain size are dependent on the Fe content and thermodynamic conditions. It is possible that high temperature will increase the mobility of adatoms, resulting in coalescence to form larger grains. In addition to the measurement of surface roughness (3.302~0.380nm) using AFM, ellipsometry was also used to measure the surface roughness (4.15~1). Both showed a downward trend of the surface roughness with Fe concentration. From the ellipsometric data (table 6.2) it is also noticeable that the refractive index increases with Fe content due to the formation of the γ- phase. The reported refractive index for γ-Ga_2O_3

was estimated in the range of 2.0~2.1[268], which closely matches with data obtained from that range, i.e. n varies from1.966 to 2.002.

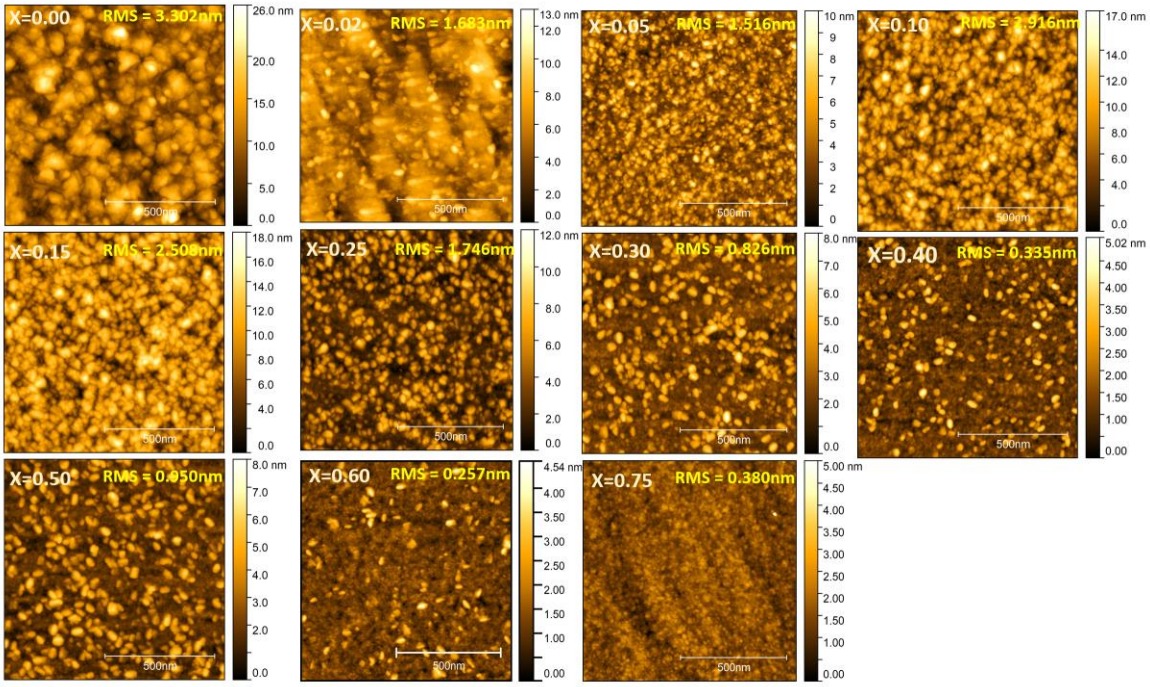

Figure 6.6. AFM (1um×1um) surface plot of $(Ga_{(1-x)}Fe_x)_2O_3$ thin films for x=0.00,-0.75, grown at temperature at 700 ^oC and pressure 1.5 $\times 10^{-6}$ torr.

The optical transmission measurement of Ga_2O_3 and its alloy with Fe were characterized by UV-Vis transmission measurements. Figure 6.7 shows Fe concentration dependent transmission spectroscopy of $(Ga_{1-x}Fe_x)_2O_3$. All samples show good optical transparency from the visible to ultraviolet regions of the spectrum with strong absorption observed around 250nm.

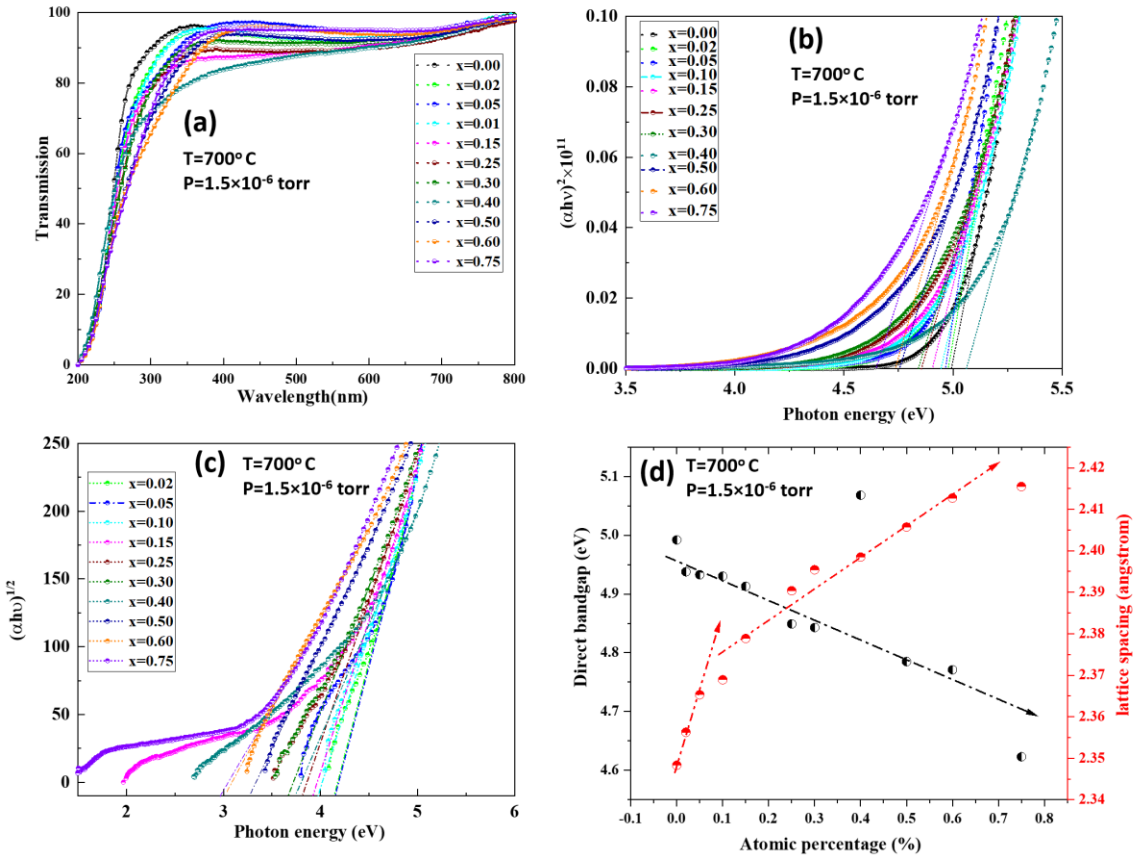

Figure 6.7. (a). Transmission spectrum of $(Ga_{(1-x)}Fe_x)_2O_3$ for x=0~ 0.75 and Tauc plot- $(\alpha h\nu)^2$ versus photon energy (eV) for corresponding these films, (b)Tauc plot for indirect bandgap (c) relationship among the bandgap, Fe concentration and lattice spacing.

The bandgap was obtained by fitting the linear region of the Tauc plot of equation (12) [268], [285], [286], as shown in figure 6.5(b).

$$\alpha h\upsilon = B(h\upsilon - Eg)^n \qquad (18)$$

where α is absorption coefficient, $h\upsilon$ is incident radiant energy, B is constant, E_g denotes bandgap, and exponent n =2 and ½ for indirect and direct bandgap, respectively. Absorption of the film was calculated using following Eq. 19.

$$\alpha = \frac{1}{t} \times \ln \ln \left[\frac{T}{(1-R)^2}\right] \qquad (19)$$

where t is the thickness of the film, T is the transmission and R is reflectance.

The estimated bandgap is presented in table 6.2. As shown in the fig. 6.7(b), the direct bandgap, obtained from the transmission measurement, shrinks with Fe concentration from 4.992 eV for β-Ga_2O_3 to 4.623 eV for $(Ga_{1-x}Fe_x)_2O_3$ for x=0.75. An increase in the Fe concentration is either causing a shrinkage in the bandgap or creating an unoccupied electronic state below the conduction band or above the valence band. In addition, as shown in figure 6.7 (d), the direct bandgap follows a mostly linear relationship with the Fe concentration. Along with the direct bandgap, the indirect bandgap was calculated using the Tauc plot figure 6.7(c) for all Fe concentrations; this indirect band gap energy varies from 4.3481~ 2.9651 eV from Ga_2O_3 to the highest Fe concentration alloy.

Table 6.2. Materials properties of $(Ga_{1-x}Fe_x)_2O_3$ thin films grown at pressure 1.5×10^{-6} torr and temperature 700°C using PLD.

Fe concentration	Thickness (nm)	Bandgap (eV)		Refractive index at 632nm	RMS Roughness using Ellipsometer (nm)	RMS Roughness using AFM (nm)
		direct	Indirect			
0.00	110.0	4.992		1.939	4.150	3.302
0.02	140.0	4.938	4.142	1.941	3.400	1.683
0.05	52.00	4.933	4.148	1.931	0.160	1.516
0.10	78.37	4.931	3.969	1.956	2.140	2.916
0.15	110.0	4.913	3.924	1.957	3.070	2.508
0.25	76.31	4.849	3.810	1.966	0.460	1.746
0.30	74.26	4.843	3.670	2.042	0.500	0.826
0.40	52.00	5.079	3.743	1.975	1.050	0.335
0.50	86.55	4.785	3.271	1.976	1.000	0.950
0.60	97.55	4.771	3.013	1.984	0.830	0.257
0.75	55.00	4.623	2.965	2.002	1.000	0.380

Chemical composition and oxidation states were investigated by XPS. The spectrum charge shift was calibrated using the fortuitous peak C 1s at a binding 284.8 eV. Figure 6.8 shows the evolution of the XPS spectrum of $(Ga_{1-x}Fe_x)_2O_3$ for x=0, 0.15, 0.75.

Photoelectron lines Ga2p, Ga3p, Ga3d, C 1s, Fe2p as well O KLL, Ga LMM Auger lines were observed from the survey spectrum shown in Figure 6.8, without any other element detected, meaning formation of high purity GaFeO thin films. For analysis purposes the Ga 3d, O 1s and Fe 2p peaks were chosen. It is apparent that Ga 3d peaks can be deconvoluted into 3 three peaks, O 2s, Ga 3d (lattice oxide), and Ga^{1+}. O 2s peak could be assigned by the hybridization of O 2s and Ga 3d surface states. As shown in figure 6.8 (e), the peak located at around 19.8eV is assigned to fully oxidized Ga^{3+} state with slight shift due to increasing Fe concentration indicative of the altering of the chemical Ga-O bond or Ga-O-Fe bond or contribution of charge transfer owing to incorporation of Fe into the lattice [287], [288]. The O 1s peaks observed at 530.51, 530.53 eV, 530.54 eV shown in figure 6.68(d) with a small carbon contaminant C-O or OH^- or oxygen vacancies that increases in the gamma structure [49], [286], [289]. Figure 6.8 (f) shows the XPS spectrum of Fe 2p, where Fe $2p_{3/2}$ can be deconvoluted into, I (Fe^{3+}), II (Fe^{2+}) located at 709.10, 710.10 eV for x=0.15 and 710.80, 709.0 eV for x=0.75 respectively, which agree well with the reported studies elsewhere [226], [290], [291] . This suggests the presence of two possible iron states i.e. Fe^{2+} and Fe^{3+} [251]. The ratios of Fe^{3+}/Fe^{2+} for the x=0.15 and 0.75 thin films are 1.95 and 1.48, respectively, which implies that with increasing Fe the concentration of Fe^{2+} ions increase. This is consistent with the increasing lattice constant for x=0.75, because Fe^{2+} (0.74 Å) has a larger radius than Fe^{3+} (0.64 Å).

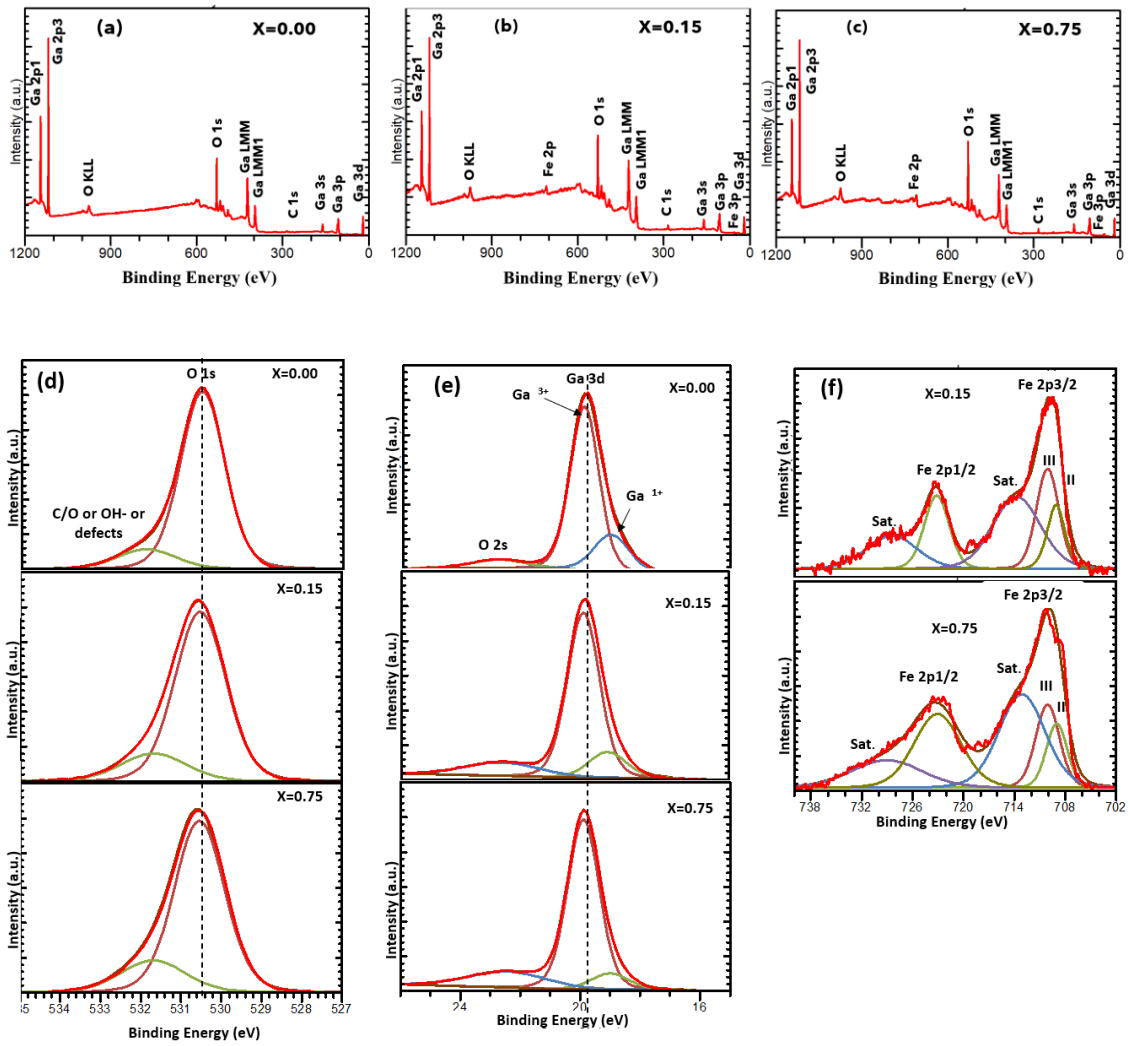

Figure 6.8. (a), (b), (c) Represent survey spectrum and (e), (f) , (g) represent O 1s, Ga 3d, Fe 2p, core levels spectra of $(Ga_{(1-x)}Fe_x)_2O_3$ for x= 0, 0.15, 0.75, respectively.

$(Ga_{1-x}Fe_x)_2O_3$ is known to be multiferroic at room temperature [268], [276], [292]–[294] exhibiting both ferroelectric and magnetic properties. Figure 6.9 shows the magnetization versus magnetic field (M-H) for $(Ga_{1-x}Fe_x)_2O_3$ for x =0.0, x=0.15, 0.75 thin films. The diamagnetic part due to the sapphire substrate (Al_2O_3) was subtracted from the plotted data. The β-Ga_2O_3 exhibits paramagnetic behavior, while $(Ga_{1-x}Fe_x)_2O_3$ for x>0 shows magnetic hysteresis, a signature of ferromagnetism that increases with Fe

content. The calculated magnetic saturation, remanence and coercivity are 5.89 emu/cm^3 , 0.6067 emu/cm^3, 45.76 O_e for x =0.15, while for x =0.75 the values were determined to be 12.63 emu/cm^3 , 1.8102 emu/cm^3 and 83.28 O_e, respectively. The mechanism behind ferromagnetic properties can be attributed spin polarization of the 3d orbital of Fe, overlapping of p-d orbital of the Fe-O bonds and the existence of defects, for example dislocation of cations (Fe^{2+} or F^{3+}) and oxygen vacancies [274], [295]–[298].

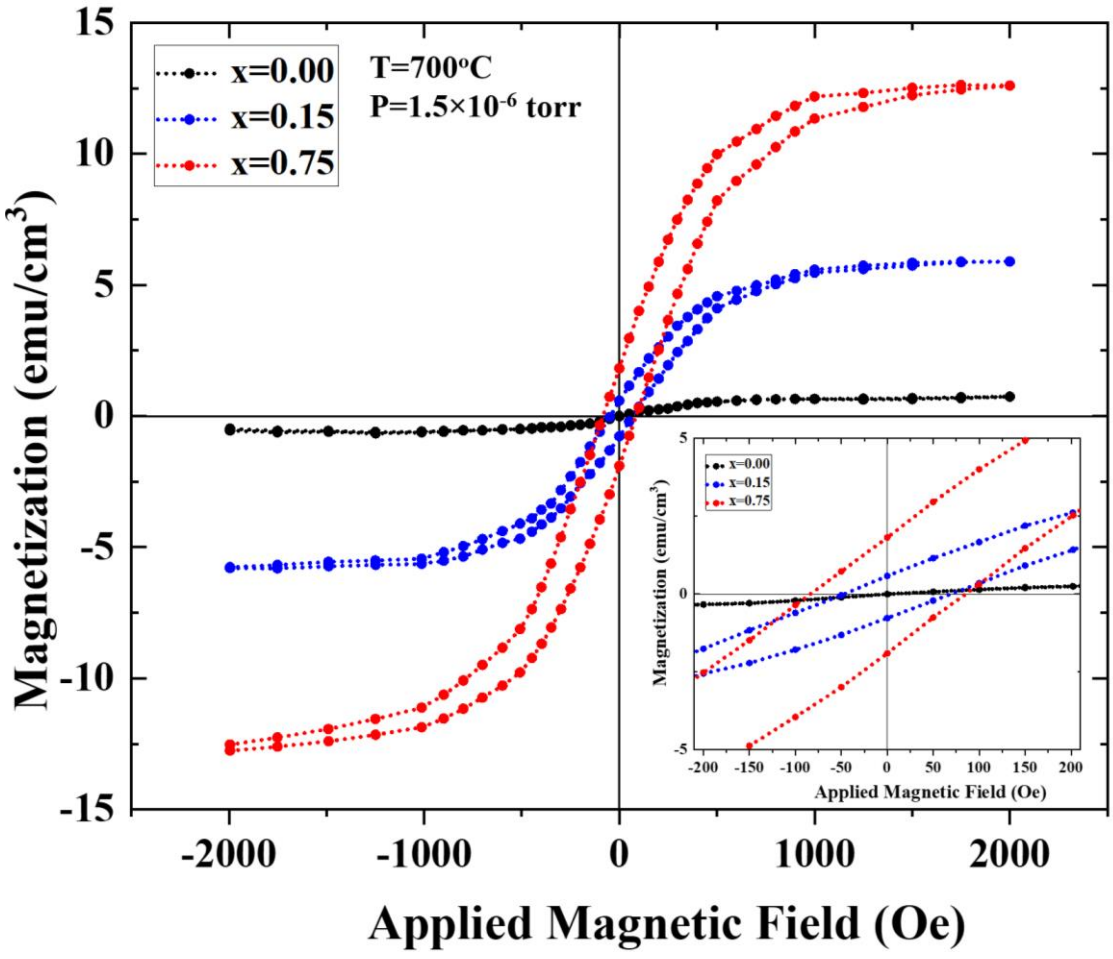

Figure 6.9. Dependence of Magnetization (M) on applied magnetic field (H) of and (inset) corresponding enlarged image $(Ga_{(1-x)}Fe_x)_2O_3$ for x =0.15 and 0.75 at RT (300K).

7. EFFECT OF ANNEALING OF $(Ga_{1-x}Fe_x)_2O_3$ THIN FILMS

7.1 Introduction

Annealing or heat treatment modifies the physical and chemical properties of a material. Usually, annealing carried out above the recrystallization temperature, maintaining a specific temperature, and then cooling. In this process, atoms diffuse and reorient toward an equilibrium state [143]. There are three stages of annealing- recovery, recrystallization, and grain growth. In the first stage, internal stress and dislocation is recovered, followed by the nucleation and growth of strain-free grains that replaces deformed states.

In the final stage of annealing, grains begins to coalesce resulting in an increase of the grain size [299]. To investigate the effect of annealing on the properties of the $(Ga_{1-x}Fe_x)_2O_3$ alloys the samples were placed in a quartz boat which was then placed in the center of a tube furnace. The samples were annealed for 80 mins in an atmosphere of pure O_2 . The annealing conditions are shown in Table 7.1.

Table 7.1. Annealing conditions.

Annealed samples	$(Ga_{1-x}Fe_x)_2O_3$ for x =0.0, 0.10, 0.15, 0.40, 0.60, 0.70
Temperature	950 ^oC
Time	80 mins
Annealing Medium	Pure O_2
O_2 flow rate	5 sccm

Firstly, as grown thin films $(Ga_{1-x}Fe_x)_2O_3$ for x =0.0, - 0.70 that were grown at temperature 700 ^oC and pressure 1.5×10^{-6} were characterized and the structural, optical, and magnetic properties were discussed in the previous chapter. To study the effect of annealing, some of these samples were then annealed with the conditions for annealing

shown in Table 7.1. Figure 7.1 shows the XRD diffraction in 2 theta-omega mode of annealed samples. Before annealing, x=0.10, 0.15, 0.40, 0.75 were determined to be spinel structures, section 6 . However, after annealing the peak positions in the XRD spectra shifted to a higher angle, which suggests a modification of the lattice represented by a decrease in the interplanar distance. The diffraction peaks around 18.89°, 38.34°, 59.00°, 82.14° correspond to the (-201), (-402), (-603), and (-802) diffraction planes of monoclinic $(Ga_{1-x}Fe_x)_2O_3$ phase, respectively. No impurity peak other than mentioned was observed. The peak's positions are in good agreement with the values reported in literature [300]. Crystalline quality was also improved after annealing, which is noticeable from the calculated FHWM (Table 7.2) measurement of the plotted samples. The reason behind the improved crystallinity might be due to the redistribution of atoms and molecules, and the reduction of defects in the structure due to the post deposition annealing.

However, as we have discussed previously, 2-theta-omega scans are not sufficient to determine the crystal structure. To confirm the phase or phase transformation from cubic to monoclinic, X-ray pole figure analysis was measured from all the samples shown in figure 7.2. According to reported literature, for a spinel structure there should be only one peak around $2\theta=30.5°$ corresponding to the diffraction plane of (220). However, there should also be several diffraction peaks at this angle, such as (400), (110), (-401), (002) and (-202) [49] thus it is difficult to determine the crystal structure using only the $2\theta - \omega$ spectrum. To confirm structure, after peak optimization, we set the detector angle at $2\theta = 29.5°$ and by changing the in plane rotation angle Φ (0~360°) and tilt angle ψ(0~90°) the diffraction intensity distributions was obtained. In the measured pole

figures, the observed diffraction intensity distribution projected from the top of the hemisphere clearly demonstrates that $(Ga_{1-x}Fe_x)_2O_3$ for all values of x has a 6-fold symmetry separated by 60° at an inclined angle around 35° and 66° which correspond to diffraction of the (-400) and (-401) planes, respectively. From calculation, the inclined angle (ψ) between (-201) and (-400)/(-401) are 36.041/66.521°, which is consistent with the experimental data and those reported in the literature [49] for the monoclinic structure. Thus, using pole figure analysis, it is clearly seen that annealing the as grown $(Ga_{1-x}Fe_x)_2O_3$ results in a structure transformation back to the monoclinic phase.

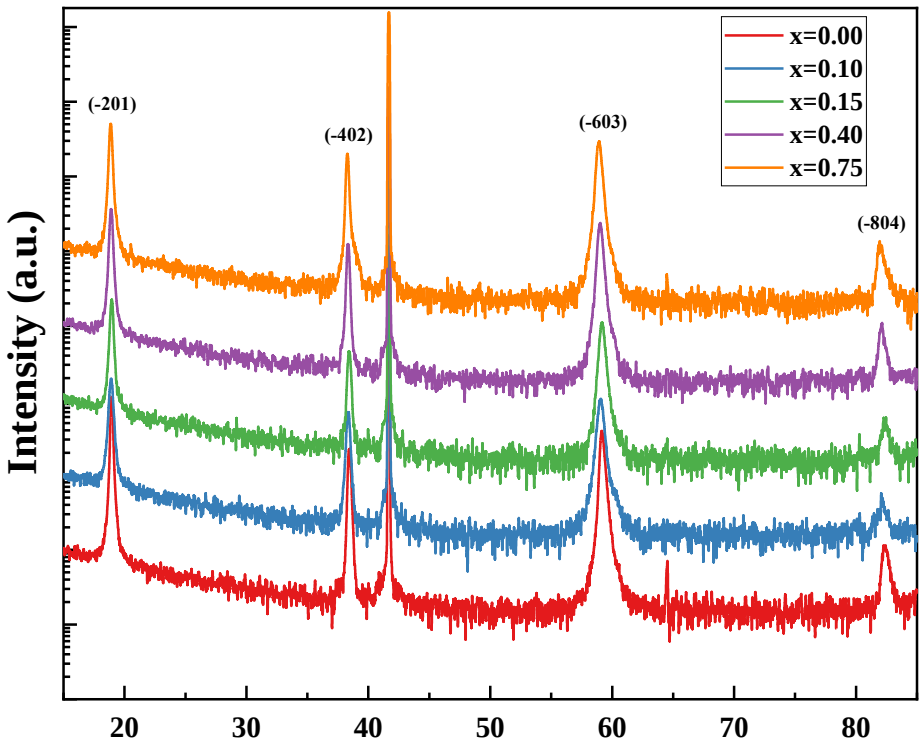

Figure 7.1. XRD patterns of $(Ga_{(1-x)}Fe_x)_2O_3$ thin films for x =0.0,-0.75 annealed 950 °C in an O_2 atmosphere.

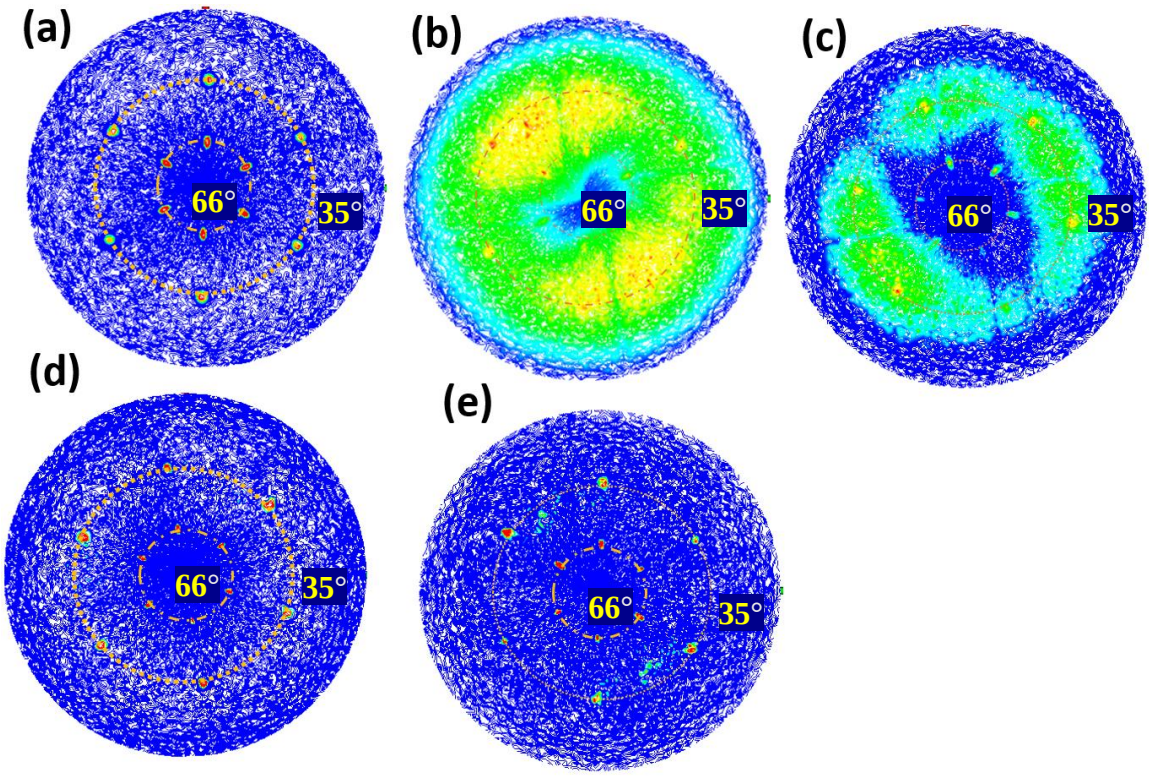

Figure 7.2. X-ray pole figure measurement of $(Ga_{(1-x)}Fe_x)_2O_3$ thin films for (a) x =0.0, (b) 0.10, (c) 0.15, (d) 0.40 and (e) 0.75 on (001) plane of sapphire substrate.

Table 7.2. Calculated FWHM and 2-theta position of $(Ga_{(1-x)}Fe_x)_2O_3$ thin films for x =0.0, 0.10, 0.15, 0.40 and 0.75.

Fe concentration (x)	2-theta position	FWHM
0.00	38.44	0.2243
0.10	38.35	0.2779
0.15	38.43	0.2613
0.40	38.34	0.2169
0.75	38.28	0.2225

Figure 7.3 shows the optical transmission spectra of the thin films after annealing. Tuning the optical energy gap of Ga_2O_3 by alloying opens the pathway for a broader range of applications, for example, solar cells, graded heterostructures for optoelectronic applications, photodetector having tunable cutoff wavelengths, optical filters with tunable transmission range, among others. It is obvious from figure 7.3 that the absorption edge

shifts to longer wavelength with the increasing Fe content (x) in the $(Ga_{1-x}Fe_x)_2O_3$ system. In the spectrum the dip in the transmission appears around 250 nm which is a typical hallmark for the presence of an intermediate band or an indirect semiconductor [301]. As shown in figure 7.3(a) (inset) the direct energy gap was obtained by extrapolating the linear part of $(\alpha h\upsilon)^2$ ~(Eg) to the horizontal axis. Similarly, an indirect bandgap was obtained using a linear fit of the plot $(\alpha h\upsilon)^{1/2}$ versus (Eg), shown in figure 7.3(b). The estimated direct bandgap for pure β-Ga_2O_3 (x=0.00) extend to 5.38eV, which is comparably much higher than the unannealed sample (4.99eV) and the literature values. As the concentration of Fe increases, the bandgap decreases from 5.57eV for x=0.02 to 4.90eV for x=0.75. Likewise, the estimated indirect bandgap was determined to be 4.81, 3.62, 3.37, 3.31,3.09,2.95, 2.93, 2.76, 2.63 eV, for Fe content x=0.00. 0.02, 0.05, 0.10, 0.15, 0.40, 0.50, 0.60, 0.75, respectively. The post-annealed samples clearly show an enhanced direct and indirect bandgap than compared to the as deposited samples. The optical absorption relies on short-range order in the microcrystalline or amorphous states and defects associated with it, the abnormality of the optical bandgap might be explained on the basis of the 'density of state model' proposed by Mott and Davis [226],[302]. Lower density of localized states can result in a larger optical bandgap. Hence the reason behind the augmented bandgap can be attributed to the decreased density of localized states, which is supported by the formation of larger grains as seen the AFM images even though there is an improved crystallinity from XRD 2-theta omega scans data, where intensity increases, as well as FWHM decreases of the thin films. A similar work trend was reported for $Cu_6Ge_{14}Te_{80}$ thin films [226]. Thus,

annealing improves the material properties and increases the potential for a wide range of optoelectronic applications.

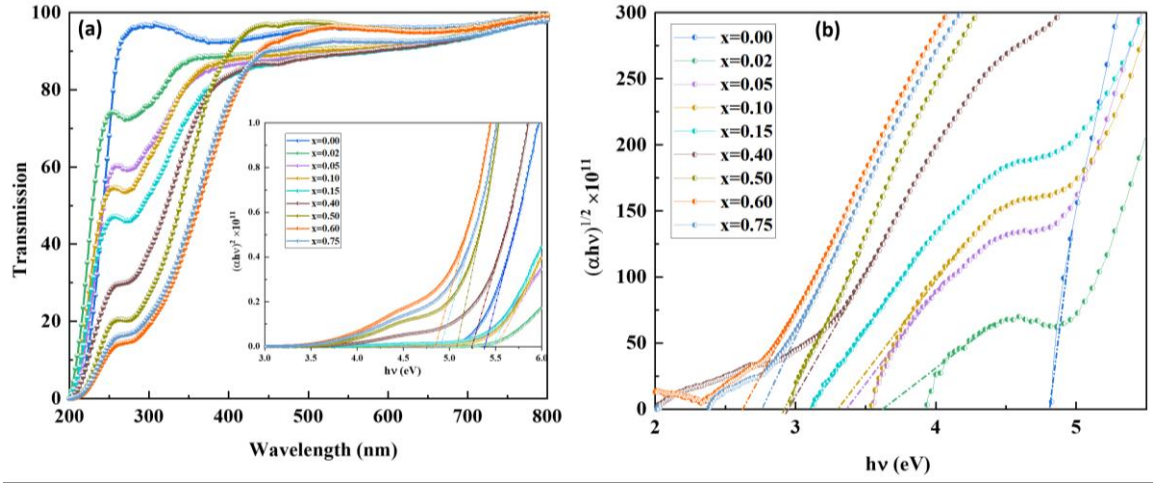

Figure 7.3. Optical transmission spectrum of annealed $(Ga_{(1-x)}Fe_x)_2O_3$ thin films for various Fe content.

Table 7.3. Direct and indirect band gap estimation of $(Ga_{1-x}Fe_x)_2O_3$ thin films for varied Fe content (x) using Tauc equation

	x=0.00	x=0.02	x=0.05	x=0.10	x=0.15	x=0.40	x=0.50	x=0.60	x=0.75
Direct bandgap (eV)	5.38	5.57	5.49	5.53	5.46	5.24	5.07	4.85	4.90
Indirect bandgap (eV)	4.81	3.62	3.37	3.31	3.09	2.95	2.93	2.63	2.76

Figure 7.4 shows the AFM images taken from the post annealed $(Ga_{1-x}Fe_x)_2O_3$ thin films for varying iron content. This showed that the grain sizes increase with annealing. The increase of grain size is a signal of a thermally activated diffusion mechanism of adatoms resulting in the coalescence of larger grains in regions with lower activation barriers[303]–[305]. The grain growth also results in increasing roughness,

which is evident by the RMS values. Increasing grain size has significant impact on materials properties, which has been observed from the UV-vis data.

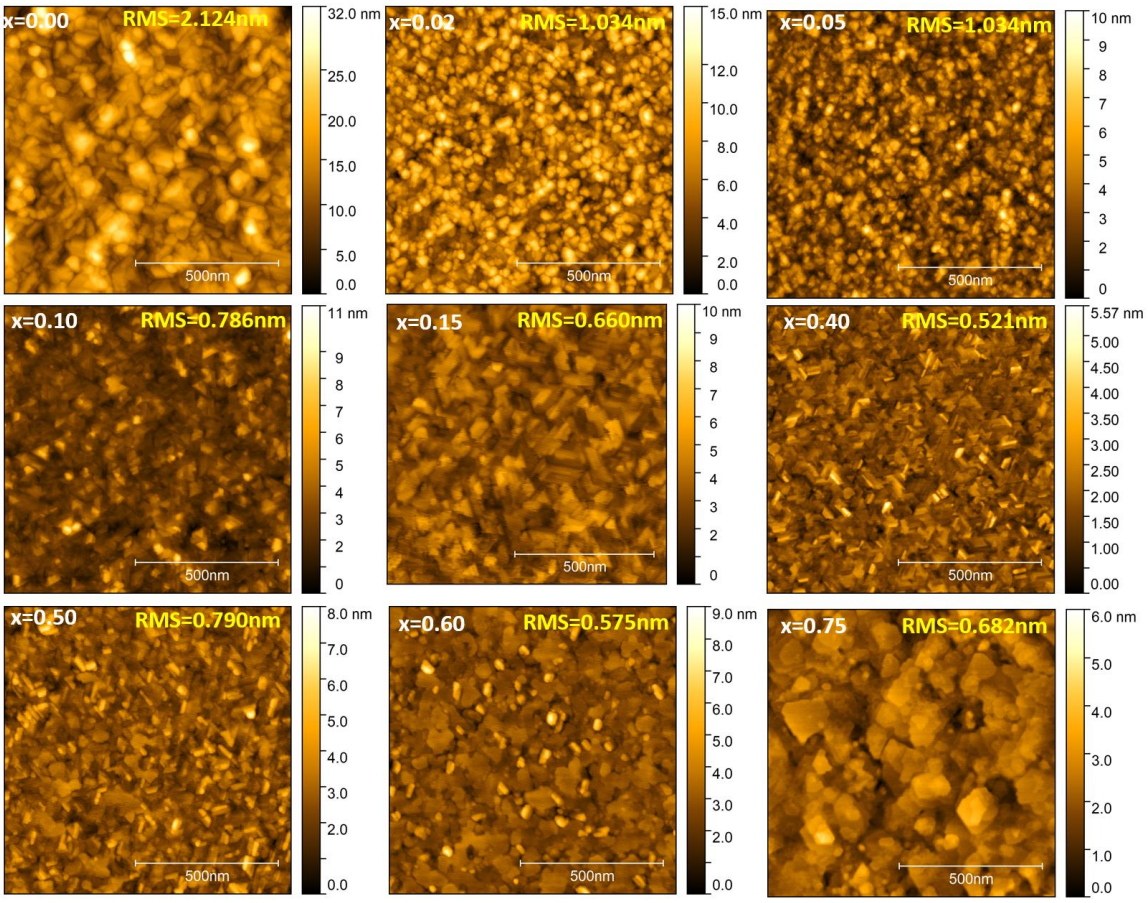

Figure 7.4. AFM (1 μm ×1 μm) surface plot of $(Ga_{(1-x)}Fe_x)_2O_3$ thin films annealed at 930 °C.

To access the electronic state and composition of the selectively annealed $(Ga_{1-x}Fe_x)_2O_3$ thin films for x=0.00 and 0.15 and 0.75, XPS measurement were conducted on the films grown on a sapphire substrates. Measurements were taken on a Scienta Omicron system in UHV (2×10^{-9} mbar)

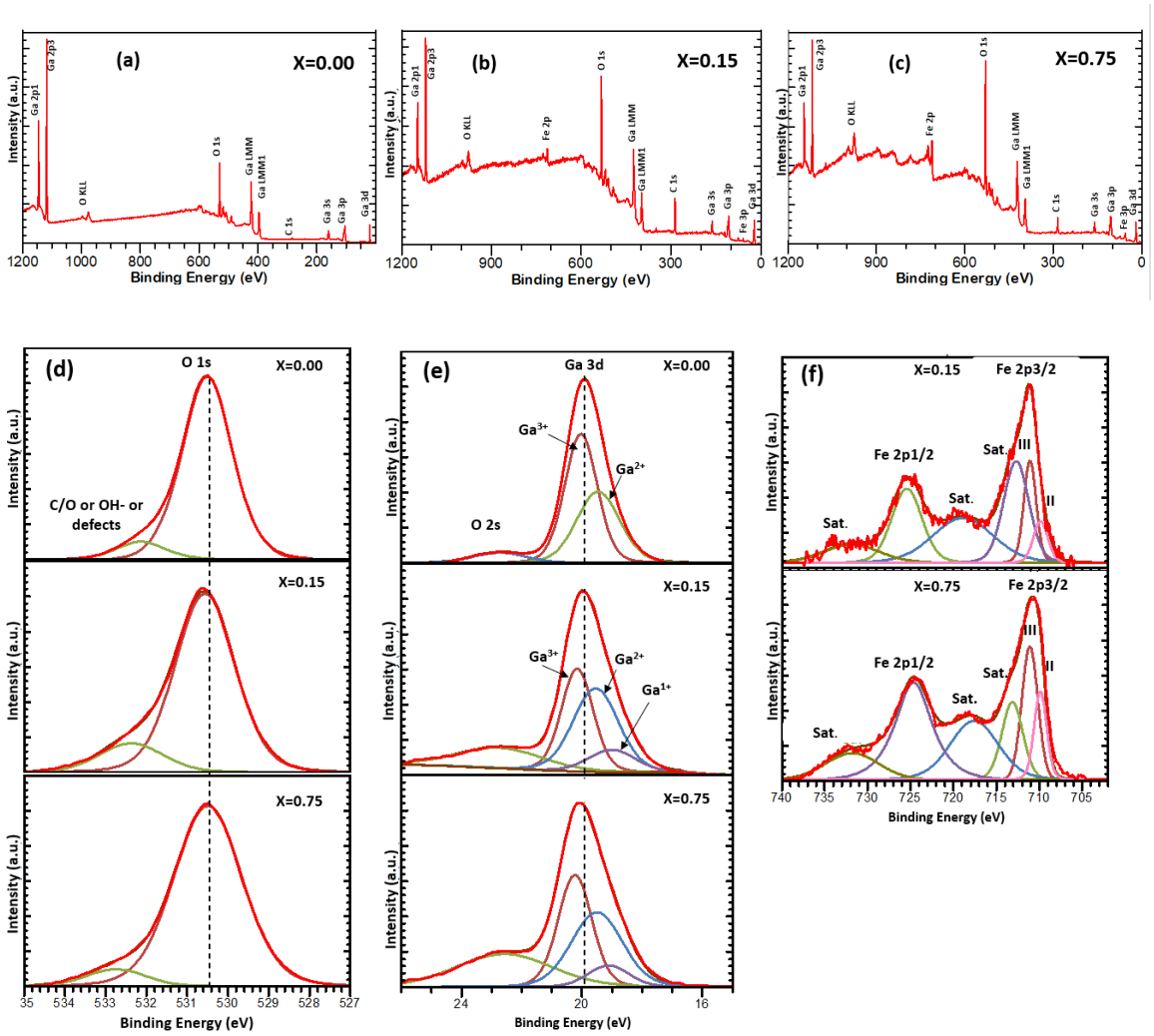

Figure 7.5. XPS (a), (b), (c) survey spectrum; (d) O 1s; (e) core levels Ga-3d and (f) are core levels Fe 2p for varied Fe content in Ga_2O_3.

at room temperature using a monochromatic aluminum Kα radiation source. Survey spectrum shown in figure 7.5(a), (b), (c), show no impurity peaks except adventitious carbon (C-1s), which was used to calibrate spectrum at a binding energy 284.8eV suggesting that the annealing did not introduce any impurities. The chemical composition of the film was analyzed using Ga-3d, O-1s and Fe-2p core levels [306], [307]. Figure 7.5(d) shows the core level O-1s peak for different Fe contents, which can be deconvoluted into two peaks located around 530.5eV for the 3 compositions, which can

be assigned to oxygen in the GaFeO lattice and other peak at higher binding energy related to the bonding of C-O or OH- or defects. The slight increase in the O 1s FWHM in the alloy is due to the oxygen bonding with both Ga and Fe in the lattice compared to the unannealed samples. Figure 7.5(e) shows the core level Ga-3d peak, deconvoluted into 4 peaks- O 2s, Ga $^{3+}$ (Ga_2O_3), Ga^{2+}(GaO) and Ga $^{1+}$ (Ga_2O) located at binding energies about~20.15, ~19.54 and ~19.00 eV, respectively.

Unlike the unannealed samples shown in figure 6.8 (e), where only Ga^{3+} and Ga $^{1+}$ are present, after annealing Ga^{2+} also appears in the spectrum for Fe content x=0.15 and 0.75. That indicates a large number of Ga^{3+} is converted to Ga^{2+} by recapturing electrons, which implies that Ga $^{3+}$ works as an electronic trap [308] in the presence of Fe, as shown as shown in figure 7.5(e). Typically, the slight BE shift occurs due to the redistribution of electronic charges of constituent atoms [307], [309]–[311], as the samples were annealed in the oxygen atmosphere, the bonding structure has been modified by the increase in certain bonds as more oxygen is present during the annealing. The XPS spectrum of the Fe 2p peak is shown for the case with Fe content of 0.15 and 0.75. In the spectrum the Fe $2p_{3/2}$ peak is greater than the Fe $2p_{1/2}$ because of spin orbit coupling (j-j) and, the fact that $Fe2p_{1/2}$ has a degeneracy of 2, while that of $Fe2p_{3/2}$ has a degeneracy of 4 [312]. The separation of the $Fe2p_{3/2}$ and the Fe $2p_{1/2}$ peaks is about 13.5eV which agrees well with the literature values [254], [313]–[316]. The deconvoluted Fe-2p peak consists of two pairs of doublet peaks and three satellite peaks shown in figure 7.5(f). The Fe $2p_{3/2}$ core level is composed of an Fe^{3+} peak (III) and an Fe^{2+} (II)-shoulder peak [317] which represents the different oxidation states of Fe. The obtained peak positions obtained agrees well with literature values [315], [318],[49]. For

high Fe content (x=0.75), the Fe^{2+} has clear enhancement as compared to the data for (x=0.15). A satellite peak around 718 eV is indicative of the coexistence of Fe^{3+} and Fe^{2+} [319], [320]. When compared to the case of the unannealed films shown in figure 6.8(e), it is clearly seen that the effect of annealing in an oxygen atmosphere is a reduction of the Fe^{2+} state relative to the Fe^{3+} oxidation state, which is confirmed by to the shift of Fe $2p_{3/2}$ peaks toward higher binding energy. In addition, the satellite peak around 718eV for the annealed sample is large compared with the unannealed sample, which is related to presence of higher Fe^{3+} content. The existence of a satellite peak has been used to determine high spin ferrous species [254],[321], such satellite peaks have been attributed to charge a transfer process or shake-up [322] . The estimated O/Ga ratios before annealing are about 2.058, 3.00 and 3.366 for x=0.00, 0.15 and 0.75 and after annealing 2.98, 4.57 and 6.29, respectively, indicating that relative oxygen content has increased during annealing.

Over the past few decades, there has been a constant search for diluted magnetic semiconductor for spintronics applications. Alloys of $(Ga_{1-x}Fe_x)_2O_3$ can be promising for ferromagnetic applications having a wide bandgap but there have been few reports on the magnetic properties of $(Ga_{1-x}Fe_x)_2O_3$ thin films [323]–[325]. This study serves to expand the knowledge of the structural and magnetic properties of this wide bandgap alloy for Fe composition up to 75%. Therefore, to examine magnetic properties samples were studied using VSM. Figure 7.6 shows room temperature as well as low temperature measurement of M-H curve of $(Ga_{1-x}Fe_x)_2O_3$ for x =0.0, 0.15 and 0.75 annealed thin films . The diamagnetic part of substrate (Al_2O_3) was subtracted from the raw data. The magnetic hysteresis observed for different Fe content suggested ferromagnetism that increases

with Fe content. The calculated magnetic saturation, remanence and coercivity was measured to be 4.99 emu/cm^3 , 1.02 emu/cm^3, 98.06 O_e for x= 0.15 respectively, and 8.92 emu/cm^3 , 2.39emu/cm^3, 143.48O_e for x= 0.75, respectively. The increase of magnetic properties might be related to the presence of more high spin Fe^{3+}, which contributed to the improved properties in comparison to the unannealed samples.

Low temperature measurements on the samples demonstrate higher magnetic properties (94.23 emu/cm^3 , 15.84emu/cm^3, 528.84 O_e for x= 0.75) than at RT. The increase of magnetic properties can be explained by a reduction of the random atomic movement and misalignment of magnetic domains. In addition, a broader hysteresis loop was observed in comparison to the sample that was not annealed. The increase of magnetic hysteresis not clearly understood for this monoclinic structure of $(Ga_{1-x}Fe_x)_2O_3$ thin films on sapphire substrate. However, the increase of the Fe^{3+}/ Fe^{2+} ratio due to the annealing and/or the resulting larger grain size may be responsible for the enhanced magnetic properties. The mechanism behind the ferromagnetic properties can be attributed to spin polarization of the 3d orbital of Fe, the overlapping of the p-d orbital of the Fe-O bonds and the existence of defects, for example the dislocation of cations (Fe^{2+} or F^{3+}), or oxygen vacancies [274], [295]–[298]

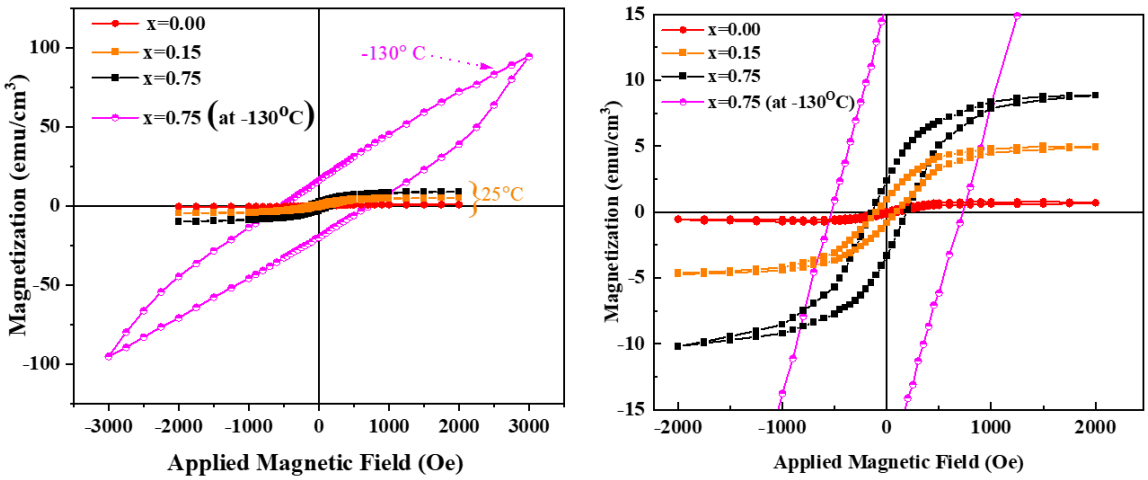

Figure 7.6. (a) M-H curve (b) enlarged view for thin films $(Ga_{(1-x)}Fe_x)_2O_3$ for x =0.00, 0.15 and 0.75. x=0.00 and 0.15 taken at RT and x=0.75 taken at RT as well as at -130°C.

8. CONCLUSIONS AND RECOMMENDATIONS FOR FUTURE WORK

8.1 Conclusions

Thin films of Ga_2O_3, $(Ga_{1-x}Gd_x)_2O_3$ and $(Ga_{1-X}Fe_X)_2O_3$ were successfully achieved using pulse laser deposition. Growth parameters, structural, optical, and magnetic properties were investigated. The monoclinic $(Ga_{1-x}Gd_x)_2O_3$ phase shows a slight red shift of the bandgap (4.99eV~4.82eV) in comparison with the pure β-Ga_2O_3, which is suitable for wideband gap applications, optical devices, MOSFET and hard radiation detectors.

Both Spinel and monoclinic $(Ga_{(1-x)}Fe_x)_2O_3$ thin films exhibit room temperature ferromagnetism, which can be used for fabrication of nonvolatile magnetic storage devices, magneto-optic devices, and microelectronics. Incorporation of Fe into Ga_2O_3 expands the lattice constant. Optical transmission measurement shows that increasing Fe content (x) moves the absorption edges toward longer wavelength and introduces an intermediate band. Similarly, high oxygen pressure introduces an intermediate band, while low oxygen pressure eliminates defects as well as induces a phase transformation from a monoclinic to the spinel phase. On the other hand, the thermally induced spinel structure in the as deposited films transforms to the monoclinic phase upon annealing the samples in high oxygen partial pressures. The spinel-phase has been important for optoelectronics and ferromagnetic applications. After annealing, an enhanced bandgap was observed for $(Ga_{(1-x)}Fe_x)_2O_3$, as well as improved magnetic properties. Chemical composition, surface states, optical properties, and crystal structure were systematically evaluated by several techniques. XRD and pole figure analysis were used to distinguish phases. The chemical composition demonstrates mixed valence state of Fe^{3+} and Fe^{2+} distributed in the films indicating and that higher oxygen pressure favors formation of

Fe^{3+} over Fe^{2+}. Surface morphology of the films was also discussed. Transitions of the surface based on concentration, pressure, temperature, and post deposition annealing were observed.

8.2 Recommendations for future Work

- Study and analysis of $(Ga_{1-x}Gd_x)_2O_3$ for gate dielectrics, heterojunctions for quantum well design, solar blind UV detector and neutron radiation detection.
- Epitaxial growth of $(Ga_{1-x}Fe_x)_2O_3$ thin films on native β- Ga_2O_3 substrate and design of multilayer thin films for transparent magnetic ferromagnetic applications.
- Investigations on spinel $(Ga_{1-x}Fe_x)_2O_3$ thin films for UV sensor design, and LED applications

REFERENCES

[1] Y. Zhang et al., "High Mobility two-dimensional electron gas in modulation-doped β-$(Al_xGa_{1-x})_2O_3/Ga_2O_3$ heterostructures, https://arxiv.org/ftp/arxiv/papers/1802/1802.04426.pdf

[2] D. Garrido-DIez and I. Baraia, "Review of wide bandgap materials and their impact in new power devices," in Proceedings of the 2017 IEEE International Workshop of Electronics, Control, Measurement, Signals and their Application to Mechatronics, ECMSM 2017, Jun. 2017, pp. 1–6, doi: 10.1109/ECMSM.2017.7945876.

[3] B. Bakeroot et al., "On the origin of the two-dimensional electron gas at AlGaN/GaN heterojunctions and its influence on recessed-gate metal-insulator-semiconductor high electron mobility transistors," Journal of Applied Physics, vol. 116, no. 13. American Institute of Physics Inc., p. 134506, Oct. 07, 2014, doi: 10.1063/1.4896900.

[4] W. Lambrechts and S. Sinha, "A Review on Si, SiGe, GaN, SiC, InP and GaAs as Enabling Technologies in EW and Space," 2017, pp. 301–329.

[5] M. Passlack et al., "Ga_2O_3 films for electronic and optoelectronic applications," Oxyg. Vacanc. donor impurities Appl. Phys. Lett., vol. 77, no. 3, p. 11301, 1995, doi: 10.1063/1.3499306.

[6] S. M. Sze and G. Gibbons, "Avalanche breakdwon voltages of abrupt and linearly graded p-n junctions in Ge, Si, GaAs, and GaP," Impact Ioniz. silicon Appl. Phys. Lett., vol. 8, p. 2744, 1966, doi: 10.1063/1.322999.

[7] J. L. Hudgins, G. S. Simin, E. Santi, and M. A. Khan, "An assessment of wide bandgap semiconductors for power devices," IEEE Trans. Power Electron., vol. 18, no. 3, pp. 907–914, 2003, doi: 10.1109/TPEL.2003.810840.

[8] H. Masataka et al., "Recent progress in Ga_2O_3 power devices," Semicond. Sci. Technol., vol. 31, no. 3, p. 34001, 2016, doi: 10.1088/0268-1242/31/3/034001.

[9] E. G. Villora, K. Shimamura, Y. Yoshikawa, K. Aoki, and N. Ichinose, "Large-size β-Ga_2O_3 single crystals and wafers," J. Cryst. Growth, vol. 270, no. 3–4, pp. 420–426, 2004, doi: 10.1016/j.jcrysgro.2004.06.027.

[10] Y. Zhuo, Z. Chen, W. Tu, X. Ma, Y. Pei, and G. Wang, "β-Ga_2O_3versus ε-Ga_2O_3: Control of the crystal phase composition of gallium oxide thin film prepared by metal-organic chemical vapor deposition," Appl. Surf. Sci., vol. 420, pp. 802–807, 2017, doi: 10.1016/j.apsusc.2017.05.241.

[11] O. Ueda et al., "Structural evaluation of defects in β-Ga_2O_3 single crystals grown by edge-defined film-fed growth process," Jpn. J. Appl. Phys., vol. 55, no. 12, p. 1202BD, 2016, doi: 10.7567/JJAP.55.1202BD.

[12] K. Hoshikawa, E. Ohba, T. Kobayashi, J. Yanagisawa, C. Miyagawa, and Y. Nakamura, "Growth of β-Ga_2O_3 single crystals using vertical Bridgman method in ambient air," J. Cryst. Growth, vol. 447, pp. 36–41, 2016, doi: 10.1016/j.jcrysgro.2016.04.022.

[13] Z. Galazka et al., "On the bulk β-Ga_2O_3 single crystals grown by the Czochralski method," J. Cryst. Growth, vol. 404, pp. 184–191, 2014, doi: 10.1016/j.jcrysgro.2014.07.021.

[14] Y. Tomm, P. Reiche, D. Klimm, and T. Fukuda, "Czochralski grown Ga_2O_3 crystals," J. Cryst. Growth, vol. 220, no. 4, pp. 510–514, 2000, doi: 10.1016/S0022-0248(00)00851-4.

[15] W. Mu et al., "High quality crystal growth and anisotropic physical characterization of β-Ga_2O_3 single crystals grown by EFG method," J. Alloys Compd., vol. 714, pp. 453–458, 2017, doi: 10.1016/j.jallcom.2017.04.185.

[16] W. Yu et al., "Improving gas sensing performance by oxygen vacancies in sub-stoichiometric WO_{3-x}," RSC Adv., vol. 9, no. 14, pp. 7723–7728, Mar. 2019, doi: 10.1039/c9ra00116f.

[17] M. Al-Hashem, S. Akbar, and P. Morris, "Role of Oxygen Vacancies in Nanostructured Metal-Oxide Gas Sensors: A Review," Sensors and Actuators, B: Chemical, vol. 301. Elsevier B.V., p. 126845, Dec. 12, 2019, doi: 10.1016/j.snb.2019.126845.

[18] E. G. Víllora, K. Shimamura, Y. Yoshikawa, T. Ujiie, and K. Aoki, "Electrical conductivity and carrier concentration control in β-Ga_2O_3 by Si doping," Appl. Phys. Lett., vol. 92, no. 20, 2008, doi: 10.1063/1.2919728.

[19] S. Müller, H. von Wenckstern, D. Splith, F. Schmidt, and M. Grundmann, "Control of the conductivity of Si-doped β-Ga_2O_3 thin films via growth temperature and pressure," Phys. status solidi, vol. 211, no. 1, pp. 34–39, Jan. 2014, doi: 10.1002/pssa.201330025.

[20] W. Zhou, C. Xia, Q. Sai, and H. Zhang, "Controlling n-type conductivity of β-Ga_2O_3 by Nb doping," Appl. Phys. Lett., vol. 111, no. 24, p. 242103, Dec. 2017, doi: 10.1063/1.4994263.

[21] B. Bayraktaroglu, "Assessment of Ga_2O_3 Technology," 2016. Accessed: Aug. 07, 2018. [Online]. Available: http://www.dtic.mil/dtic/tr/fulltext/u2/1035362.pdf.

[22] H. Asahi, Y. K. Zhou, S. Emura, and S. Hasegawa, "Gadolinium-doped III-nitride diluted magnetic semiconductors for spintronics applications," in Rare Earth and Transition Metal Doping of Semiconductor Materials: Synthesis, Magnetic Properties and Room Temperature Spintronics, Elsevier Inc., 2016, pp. 371–394.

[23] D. Gourier, L. Binet, and E. Aubay, "Magnetic bistability and memory of conduction electrons released from oxygen vacancies in gallium oxide," Radiat. Eff. Defects Solids, vol. 134, no. 1–4, pp. 223–228, Dec. 1995, doi: 10.1080/10420159508227219.

[24] S. J. Pearton et al., "A review of β-Ga_2O_3 materials, processing, and devices," Appl. Phys. Rev., vol. 5, no. 1, p. 011301, 2018, doi: 10.1063/1.5006941.

[25] L. Binet and D. Gourier, "Bistable magnetic resonance of conduction electrons in solids," J. Phys. Chem., vol. 100, no. 44, pp. 17630–17639, 1996, doi: 10.1021/jp962094y.

[26] F. Roulland, C. Lefevre, A. Thomasson, and N. Viart, "Study of $Ga_{(2-x)}Fe_xO_3$ solid solution: Optimisation of the ceramic processing," J. Eur. Ceram. Soc., vol. 33, no. 5, pp. 1029–1035, 2013, doi: 10.1016/j.jeurceramsoc.2012.11.014.

[27] E. Aubay and D. Gourier, "Magnetic bistability and Overhauser shift of conduction electrons in gallium oxide," Phys. Rev. B, vol. 47, no. 22, pp. 15023–15036, 1993, doi: 10.1103/PhysRevB.47.15023.

[28] Z. Der and D. M. Hofmann, "Structural and magnetic investigation of dilute magnetic semiconductors based on," 2010.

[29] T. Dietl, H. Ohno, F. Matsukura, J. Cibert, and D. Ferrand, “Zener model description of ferromagnetism in zinc-blende magnetic semiconductors,” Science (80-.)., vol. 287, no. 5455, pp. 1019–1022, Feb. 2000, doi: 10.1126/science.287.5455.1019.

[30] J. Li et al., “Identification and modulation of electronic band structures of single-phase β-$(Al_xGa_{1-x})_2O_3$ alloys grown by laser molecular beam epitaxy,” Appl. Phys. Lett., vol. 113, no. 4, p. 041901, 2018, doi: 10.1063/1.5027763.

[31] Y. Zhang et al., “Demonstration of high mobility and quantum transport in modulation doped β-$(Al_xGa_{1-x})_2O_3/Ga_2O_3$ heterostructures,” Appl. Phys. Lett., vol. 112, no. 17, p. 173502, Apr. 2018, doi: 10.1063/1.5025704.

[32] N. B. C. C. H. Sui, “Recent progress in research on $Mg_xZn_{1-x}O$ alloys - [PDF Document].” https://vdocuments.mx/recent-progress-in-research-on-mgxzn1xo-alloys.html (accessed Jul. 27, 2018).

[33] E. Monroy, F. Omnès, and F. Calle, “Wide-bandgap semiconductor ultraviolet photodetectors,” 2003. Accessed: Jul. 27, 2018. [Online]. Available: http://iopscience.iop.org/article/10.1088/0268-1242/18/4/201/pdf.

[34] F. Zhang, H. Li, M. Arita, and Q. Guo, “Ultraviolet detectors based on $(GaIn)_2O_3$ films,” Opt. Mater. Express, vol. 7, no. 10, p. 3769, 2017, doi: 10.1364/OME.7.003769.

[35] F. Zhang, K. Saito, T. Tanaka, M. Nishio, M. Arita, and Q. Guo, “Wide bandgap engineering of $(AlGa)_2O_3$ films,” Appl. Phys. Lett., vol. 105, no. 16, p. 162107, 2014, doi: 10.1063/1.4900522.

[36] S. Ghose, R. Droopad, C. E. Powell, W. Geerts, M. Chen, and T. Zirkle, “GROWTH AND CHARACTERIZATION OF WIDE BANDGAP SEMICONDUCTOR OXIDE THIN FILMS,” 2017, Accessed: Jul. 07, 2018. [Online]. Available: https://digital.library.txstate.edu/bitstream/handle/10877/6762/GHOSE-DISSERTATION-2017.pdf?sequence=1&isAllowed=y.

[37] S. Ghose et al., “Structural and optical properties of β-Ga_2O_3 thin films grown by plasma-assisted molecular beam epitaxy,” J. Vac. Sci. Technol. B, Nanotechnol. Microelectron. Mater. Process. Meas. Phenom., vol. 34, no. 2, p. 02L109, 2016, doi: 10.1116/1.4942045.

[38] M. Higashiwaki, K. Sasaki, A. Kuramata, T. Masui, and S. Yamakoshi, “Development of gallium oxide power devices,” Phys. Status Solidi Appl. Mater. Sci., vol. 211, no. 1, pp. 21–26, 2014, doi: 10.1002/pssa.201330197.

[39] Y. Tomm, J. M. Ko, A. Yoshikawa, and T. Fukuda, “Floating zone growth of-Ga O : A new window material for optoelectronic device applications,” 2001. Accessed: Aug. 02, 2018. [Online].Available:https://ac.elscdn.com/S0927024800001963/1-s2.0-S0927024800001963main.pdf?_tid=d380f46e-2c4b-4629-8736-23db12e08b68&acdnat=1533187544_b8d50242a790e43d0e8cbe6f60f16436.

[40] D. P. Halliday, “A visible large area light emitting diode fabricated from porous silicon using a conducting polyaniline contact,” in IEE Colloquium on Materials for Displays, 1995, vol. 1995, pp. 13–13, doi: 10.1049/ic:19950980.

[41] T. Wang, S. S. Farvid, M. Abulikemu, and P. V. Radovanovic, “Size-tunable phosphorescence in colloidal metastable γ- Ga_2O_3 nanocrystals,” J. Am. Chem. Soc., vol. 132, no. 27, pp. 9250–9252, Jul. 2010, doi: 10.1021/ja101333h.

[42] H. Hayashi et al., “Room temperature ferromagnetism in Mn-doped γ-Ga_2O_3 with spinel structure,” Appl. Phys. Lett., vol. 89, no. 18, p. 181903, Oct. 2006, doi: 10.1063/1.2369541.

[43] R. Huang, H. Hayashi, F. Oba, and I. Tanaka, “Microstructure of Mn-doped γ-Ga_2O_3 epitaxial film on sapphire (0001) with room temperature ferromagnetism,” J. Appl. Phys., vol. 101, no. 6, p. 063526, Mar. 2007, doi: 10.1063/1.2713349.

[44] H. Munekata, H. Ohno, S. Von Molnar, A. Segm̈ller, L. L. Chang, and L. Esaki, “Diluted magnetic III-V semiconductors,” Phys. Rev. Lett., vol. 63, no. 17, pp. 1849–1852, Oct. 1989, doi: 10.1103/PhysRevLett.63.1849.

[45] H. Ohno et al., “(Ga,Mn)As: A new diluted magnetic semiconductor based on GaAs,” Appl. Phys. Lett., vol. 69, no. 3, pp. 363–365, Jul. 1996, doi: 10.1063/1.118061.

[46] H. Ohno, “Making nonmagnetic semiconductors ferromagnetic,” Science, vol. 281, no. 5379. American Association for the Advancement of Science, pp. 951–956, Aug. 14, 1998, doi: 10.1126/science.281.5379.951.

[47] B. Beschoten et al., “Magnetic circular dichroism studies of carrier-induced ferromagnetism in $(Ga_{1-x}Mn_x)$ as,” Phys. Rev. Lett., vol. 83, no. 15, pp. 3074–3076, Jan. 1999, doi: 10.1103/PhysRevLett.83.3073.

[48] T. Kondo, H. Owa, and H. Munekata, “(Ga,Mn)N: Sn epilayers,” J. Supercond. Nov. Magn., vol. 16, no. 1, pp. 103–106, 2003, doi: 10.1023/A:1023249104791.

[49] Y. Huang et al., “Fe doping-stabilized γ- Ga_2O_3 thin films with a high room temperature saturation magnetic moment,” J. Mater. Chem. C, vol. 8, no. 2, pp. 536–542, Jan. 2020, doi: 10.1039/c9tc05823k.

[50] F. H. Teherani et al., “A review of the growth, doping, and applications of Beta-Ga_2O_3 thin films,” Oxide-based Mater. Devices IX, no. March, p. 25, 2018, doi: 10.1117/12.2302471.

[51] J. B. Varley, J. R. Weber, A. Janotti, and C. G. Van De Walle, “Oxygen vacancies and donor impurities in β-Ga_2O_3,” Appl. Phys. Lett., vol. 97, no. 14, pp. 97–100, 2010, doi: 10.1063/1.3499306.

[52] A. Kyrtsos, M. Matsubara, and E. Bellotti, “On the feasibility of p-type Ga_2O_3,” Appl. Phys. Lett., vol. 112, no. 3, 2018, doi: 10.1063/1.5009423.

[53] M. Passlack et al., “Dielectric properties of electron-beam deposited Ga_2O_3 films,” Cit. Appl. Phys. Lett, vol. 64, p. 2715, 1994, doi: 10.1063/1.111452.

[54] K. Sasaki, A. Kuramata, T. Masui, E. G. Víllora, K. Shimamura, and S. Yamakoshi, “Device-Quality Device-Quality β-Ga_2O_3 -Epitaxial Films Fabricated by Ozone Molecular Beam EpitaxyEpitaxial Films Fabricated by Ozone Molecular Beam Epitaxy,” Appl. Phys. Express, vol. 5, no. 3, p. 035502, 2012, doi: 10.1143/APEX.5.035502.

[55] K. Ghosh and U. Singisetti, “Electron mobility in monoclinic β-Ga_2O_3 - Effect of plasmon-phonon coupling, anisotropy, and confinement,” J. Mater. Res., vol. 32, no. 22, pp. 4142–4152, Nov. 2017, doi: 10.1557/jmr.2017.398.

[56] M. Baldini et al., “Semiconducting Sn-doped β-Ga_2O_3 homoepitaxial layers grown by metal organic vapour-phase epitaxy,” doi: 10.1007/s10853-015-9693-6.

[57] E. Ahmadi et al., “Ge doping of β-Ga_2O_3 films grown by plasma-assisted molecular beam epitaxy,” Appl. Phys. Express, vol. 10, no. 4, p. 041102, Apr. 2017, doi: 10.7567/APEX.10.041102.

[58] K. D. Leedy et al., “Highly conductive homoepitaxial Si-doped Ga_2O_3 films on (010) β-Ga_2O_3 by pulsed laser deposition,” Cit. Appl. Phys. Lett, vol. 111, p. 12103, 2017, doi: 10.1063/1.4991363.

[59] T. Oshima, K. Kaminaga, and A. Mukai, “Si-Ion Implantation Doping in β-Ga_2O_3 3 and Its Application to Fabrication of Low-Resistance Ohmic Contacts Related content Formation of Semi-Insulating Layers on Semiconducting-Ga 2 O 3 Single Crystals by Thermal Oxidation,” doi: 10.7567/APEX.6.086502.

[60] H. He, W. Li, H. Z. Xing, and E. J. Liang, “First Principles Study on the Electronic Properties of Cr, Fe, Mn and Ni Doped β-Ga_2O_3 ,” Adv. Mater. Res., vol. 535–537, pp. 36–41, Jun. 2012, doi: 10.4028/www.scientific.net/AMR.535-537.36.

[61] J. Atanelov and P. Mohn, “Electronic and magnetic properties of $GaFeO_3$: Ab initio calculations for varying Fe/Ga ratio, inner cationic site disorder, and epitaxial strain,” Phys. Rev. B, vol. 92, p. 104408, 2015, doi: 10.1103/PhysRevB.92.104408.

[62] Y. Huang et al., “High-insulating β-Ga_2O_3 thin films by doping with a valence controllable Fe element,” Appl. Phys. A, vol. 124, no. 9, p. 611, 2018, doi: 10.1007/s00339-018-2037-z.

[63] X. Bi, Z. Wu, Y. Huang, and W. Tang, “Stabilization and enhanced energy gap by Mg doping in **ε** -phase Ga_2O_3 thin films,” AIP Adv., vol. 8, no. 2, p. 025008, 2018, doi: 10.1063/1.5022600.

[64] F. Alema et al., “Solar blind photodetector based on epitaxial zinc doped Ga_2O_3 thin film,” Phys. Status Solidi Appl. Mater. Sci., vol. 214, no. 5, 2017, doi: 10.1002/pssa.201600688.

[65] M. Handwerg, R. Mitdank, Z. Galazka, and S. F. Fischer, “Temperature-dependent thermal conductivity and diffusivity of a Mg-doped insulating Ga_2O_3 single crystal along [100] ,” Semicond. Sci. Technol., vol. 31, no. 12, pp. 1–6, 2016, doi: 10.1088/0268-1242/31/12/125006.

[66] D. Guo et al., “Epitaxial growth and magnetic properties of ultraviolet transparent Ga_2O_3 /$(Ga_{1-x}Fe_x)_2O_3$ multilayer thin films,” Sci. Rep., vol. 6, no. 1, p. 25166, 2016, doi: 10.1038/srep25166.

[67] A. Kyrtsos, M. Matsubara, and E. Bellotti, “On the feasibility of p-type Ga_2O_3,” Appl. Phys. Lett., vol. 112, no. 3, p. 032108, Jan. 2018, doi: 10.1063/1.5009423.

[68] and C. G. V. de W. Youngho Kang, Karthik Krishnaswamy, Hartwin Peelaers, “Fundamental limits on the electron mobility of β-Ga_2O_3 . Journal of Physics: Condensed Matter, 29(23), 234001 | 10.1088/1361-648X/aa6f66.” https://sci-hub.tw/10.1088/1361-648x/aa6f66 (accessed Jun. 02, 2020).

[69] A. T. Neal et al., “Donors and deep acceptors in β-Ga_2O_3,” Cit. Appl. Phys. Lett, vol. 113, p. 62101, 2018, doi: 10.1063/1.5034474.

[70] Z. Galazka et al., “Doping of Czochralski-grown bulk β-Ga_2O_3 single crystals with Cr, Ce and Al,” J. Cryst. Growth, vol. 486, pp. 82–90, Mar. 2018, doi: 10.1016/j.jcrysgro.2018.01.022.

[71] C. Yu et al., “Synthesis of Eu^{2+} /Eu^{3+} Co-Doped Gallium oxide nanocrystals as a full colour converter for white light emitting diodes,” J. Colloid Interface Sci., vol. 530, pp. 52–57, 2018, doi: 10.1016/j.jcis.2018.06.047.

[72] Y. Usui, T. Oya, G. Okada, N. Kawaguchi, and T. Yanagida, “Ce-doped Ga_2O_3 single crystalline semiconductor showing scintillation features,” Optik (Stuttg)., vol. 143, pp. 150–157, Aug. 2017, doi: 10.1016/j.ijleo.2017.06.061.

[73] C. Lecerf, P. Marie, J. Cardin, F. Jomard, and X. Portier, “Texture effect of neodymium doped gallium oxide thin films on their optical properties,” 2011, doi: 10.1016/j.optmat.2010.10.026.

[74] B. Wu et al., “Applied Physics B Broadband infrared luminescence from transparent glass-ceramics containing Ni^{2+}-doped β-Ga_2O_3 nanocrystals,” Appl. Phys. B, vol. 87, pp. 697–699, 2007, doi: 10.1007/s00340-007-2639-1.

[75] R. Kumaran, T. Tiedje, S. E. Webster, S. Penson, and W. Li, “Epitaxial Nd-doped α-$(Al_{1-x}Ga_x)_2O_3$ films on sapphire for solid-state waveguide lasers,” Opt. Lett., vol. 35, no. 22, p. 3793, Nov. 2010, doi: 10.1364/OL.35.003793.

[76] A. Podhorodecki et al., “Influence of neodymium concentration on excitation and emission properties of Nd doped gallium oxide nanocrystalline films,” Cit. J. Appl. Phys., vol. 108, p. 143104, 2010, doi: 10.1063/1.3484039.

[77] M. Higashiwaki, K. Sasaki, A. Kuramata, T. Masui, and S. Yamakoshi, “Gallium oxide (Ga_2O_3) metal-semiconductor field-effect transistors on single-crystal β-Ga_2O_3 (010) substrates,” Appl. Phys. Lett., 2012, doi: 10.1063/1.3674287.

[78] Masataka, “Current status of Ga_2O_3 power devices,” Jpn. J. Appl. Phys, vol. 55, pp. 1202–1, 2016.

[79] K. D. Chabak et al., “Enhancement-mode Ga_2O_3 wrap-gate fin field-effect transistors on native (100) β-Ga_2O_3 substrate with high breakdown voltage,” Appl. Phys. Lett., vol. 109, no. 21, p. 213501, Nov. 2016, doi: 10.1063/1.4967931.

[80] T. Oshima, T. Okuno, and S. Fujita, “Ga_2O_3 Thin Film Growth on c -Plane Sapphire Substrates by Molecular Beam Epitaxy for Deep-Ultraviolet Photodetectors,” Jpn. J. Appl. Phys., vol. 46, no. 11, pp. 7217–7220, Nov. 2007, doi: 10.1143/JJAP.46.7217.

[81] G. C. Hu, C. X. Shan, N. Zhang, M. M. Jiang, S. P. Wang, and D. Z. Shen, “High gain Ga2O3 solar-blind photodetectors realized via a carrier multiplication process,” Opt. Express, vol. 23, no. 10, p. 13554, May 2015, doi: 10.1364/OE.23.013554.

[82] X. Z. Liu, P. Guo, T. Sheng, L. X. Qian, W. L. Zhang, and Y. R. Li, “β-Ga_2O_3 thin films on sapphire pre-seeded by homo-self-templated buffer layer for solar-blind UV photodetector,” Opt. Mater. (Amst)., vol. 51, pp. 203–207, Jan. 2016, doi: 10.1016/j.optmat.2015.11.023.

[83] D. Guo et al., “Fabrication of β-Ga_2O_3 thin films and solar-blind photodetectors by laser MBE technology,” Opt. Mater. Express, 2014, doi: 10.1364/OME.4.001067.

[84] and Q. G. Fabi Zhang, Haiou Li, Makoto Arita, “Ultraviolet detectors based on $(GaIn)_2O_3$ films,” Opt. Mater. Express, vol. 7, no. 10, 2017, Accessed: Sep. 10, 2018. [Online].

[85] X. Zhao et al., “Growth and Characterization of Sn Doped β-Ga_2O_3 Thin Films and Enhanced Performance in a Solar-Blind Photodetector,” J. Electron. Mater., vol. 46, no. 4, pp. 2366–2372, Apr. 2017, doi: 10.1007/s11664-017-5291-5.

[86] D. Guo et al., “Zero-Power-Consumption Solar-Blind Photodetector Based on β-Ga_2O_3/NSTO Heterojunction,” ACS Appl. Mater. Interfaces, vol. 9, no. 2, pp. 1619–1628, Jan. 2017, doi: 10.1021/acsami.6b13771.

[87] D. Y. Guo et al., “Fabrication of β-Ga_2O_3 /ZnO heterojunction for solar-blind deep ultraviolet photodetection,” Semicond. Sci. Technol., vol. 32, no. 3, p. 03LT01, Mar. 2017, doi: 10.1088/1361-6641/aa59b0.

[88] A. Kalra, S. Vura, S. Rathkanthiwar, R. Muralidharan, S. Raghavan, and D. N. Nath, “Demonstration of high-responsivity epitaxial β-Ga_2O_3 /GaN metal–heterojunction-metal broadband UV-A/UV-C detector,” Appl. Phys. Express, vol. 11, no. 6, p. 064101, Jun. 2018, doi: 10.7567/APEX.11.064101.

[89] X. C. Guo et al., “β-Ga_2O_3 /p-Si heterojunction solar-blind ultraviolet photodetector with enhanced photoelectric responsivity,” J. Alloys Compd., vol. 660, pp. 136–140, 2016, doi: 10.1016/j.jallcom.2015.11.145.

[90] C. C. Wang et al., “Growth and characterization of co-sputtered aluminum-gallium oxide thin films on sapphire substrates,” J. Alloys Compd., vol. 765, pp. 894–900, Oct. 2018, doi: 10.1016/j.jallcom.2018.06.270.

[91] T. Oshima and S. Fujita, “Properties of Ga_2O_3 -based $(In_xGa_{1-x})_2O_3$ alloy thin films grown by molecular beam epitaxy,” in Physica Status Solidi (C) Current Topics in Solid State Physics, 2008, vol. 5, no. 9, pp. 3113–3115, doi: 10.1002/pssc.200779297.

[92] X. L. and C.-K. Tan, “First-principle investigation of monoclinic $(Al_xIn_yGa1\text{-}x\text{-}y)_2O_3$ quaternary alloys - IOPscience.”https://iopscience.iop.org/article/10.1088/1361-6641/ab607c (accessed May 19, 2020).

[93] D. Guo, Q. Guo, Z. Chen, Z. Wu, P. Li, and W. Tang, “Review of β-Ga_2O_3 -based optoelectronic devices,” Materials Today Physics, vol. 11. Elsevier Ltd, p. 100157, Dec. 01, 2019, doi: 10.1016/j.mtphys.2019.100157.

[94] A. Y. Polyakov, N. B. Smirnov, I. V. Shchemerov, D. Gogova, S. A. Tarelkin, and S. J. Pearton, “Compensation and persistent photocapacitance in homoepitaxial Sn-doped β-Ga_2O_3 ,” J. Appl. Phys., vol. 123, no. 11, p. 115702, Mar. 2018, doi: 10.1063/1.5025916.

[95] Q. Liu et al., “Stabilizing the metastable γ phase in Ga_2O_3 thin films by Cu doping,” J. Alloys Compd., vol. 731, pp. 1225–1229, Jan. 2018, doi: 10.1016/j.jallcom.2017.10.162.

[96] M. Zinkevich, F. Aldinger, “Thermodynamic Assessment of the Gallium-Oxygen System,” J. Am. Ceram. Soc., 87, No. 4.

[97] M. Higashiwaki, K. Sasaki, A. Kuramata, T. Masui, and S. Yamakoshi, “Development of gallium oxide power devices,” Phys. Status Solidi Appl. Mater. Sci., 2014, doi: 10.1002/pssa.201330197.

[98] M. Higashiwaki et al., “Depletion-mode Ga_2O_3 metal-oxide-semiconductor field-effect transistors on β-Ga_2O_3 (010) substrates and temperature dependence of their device characteristics,” Appl. Phys. Lett., 2013, doi: 10.1063/1.4821858.

[99] S. Geller, “On the structure of β-Ga_2O_3,” J. Solid State Chem., 1977, doi: 10.1016/0022-4596(77)90070-6.

[100] R. Roy, V. G. Hill, and E. F. Osborn, “Polymorphism of β-Ga_2O_3 and the System Ga_2O_3-H_2O,” J. Amer. Chem. Soc., 1952, doi: 10.1021/ja01123a039.

[101] H. He et al., “First-principles study of the structural, electronic, and optical properties of Ga_2O_3 in its monoclinic and hexagonal phases,” Phys. Rev. B, 2006, doi: 10.1103/PhysRevB.74.195123.

[102] S. Geller, “Crystal Structure of β-Ga_2O_3 ,” Cit. J. Chem. Phys., vol. 33, p. 4166, 1960, doi: 10.1063/1.1330559.

[103] M. Mohamed et al., “The electronic structure of -Ga_2O_3,” J. Chem. Phys., vol. 97, p. 676, 2010, doi: 10.1063/1.1731237.

[104] M. Hegde, I. D. Hosein, and P. V. Radovanovic, “Molecular Origin of Valence Band Anisotropy in Single β-Ga_2O_3 Nanowires Investigated by Polarized X-ray Absorption Imaging,” J. Phys. Chem. C, vol. 119, no. 30, pp. 17450–17457, 2015, doi: 10.1021/acs.jpcc.5b04945.

[105] H. Su, X. T. Wang, J. X. Hu, T. Ouyang, K. Xiao, and Z. Q. Liu, “Co-Mn spinel supported self-catalysis induced N-doped carbon nanotubes with high efficiency electron transport channels for zinc-Air batteries,” J. Mater. Chem. A, vol. 7, no. 39, pp. 22307–22313, Oct. 2019, doi: 10.1039/c9ta08064c.

[106] H. Kawazoe and K. Ueda, “Transparent Conducting Oxides Based on the Spinel Structure,” J. Am. Ceram. Soc., vol. 82, no. 12, pp. 3330–3336, Dec. 2004, doi: 10.1111/j.1151-2916.1999.tb02247.x.

[107] H. Hayashi, R. Huang, F. Oba, T. Hirayama, and I. Tanaka, “Site preference of cation vacancies in Mn-doped Ga_2O_3 with defective spinel structure,” Appl. Phys. Lett., vol. 101, no. 24, p. 241906, Dec. 2012, doi: 10.1063/1.4770363.

[108] X. Xia et al., “Hexagonal phase-pure wide band gap ϵ-Ga_2O_3 films grown on 6H-SiC substrates by metal organic chemical vapor deposition,” Appl. Phys. Lett., vol. 108, no. 20, p. 202103, May 2016, doi: 10.1063/1.4950867.

[109] F. Boschi, M. Bosi, T. Berzina, E. Buffagni, C. Ferrari, and R. Fornari, “Hetero-epitaxy of ε-Ga_2O_3 layers by MOCVD and ALD,” J. Cryst. Growth, vol. 443, pp. 25–30, Jun. 2016, doi: 10.1016/j.jcrysgro.2016.03.013.

[110] Y. Oshima, E. G. Víllora, Y. Matsushita, S. Yamamoto, and K. Shimamura, “Epitaxial growth of phase-pure ε-Ga_2O_3 by halide vapor phase epitaxy,” J. Appl. Phys., vol. 118, no. 8, p. 085301, Aug. 2015, doi: 10.1063/1.4929417.

[111] S. et al. Yoshioka, “Structures and energetics of Ga_2O_3 polymorphs — Kyushu University.” https://kyushu-u.pure.elsevier.com/en/publications/structures-and-energetics-of-gasub2subosub3sub-polymorphs (accessed Jun. 06, 2020).

[112] M. Kracht et al., “Tin-Assisted Synthesis of ϵ-$Ga_2O_3$by Molecular Beam Epitaxy,” Phys. Rev. Appl., vol. 8, no. 5, p. 054002, Nov. 2017, doi: 10.1103/PhysRevApplied.8.054002.

[113] M. B. Maccioni and V. Fiorentini, “Phase diagram and polarization of stable phases of $(Ga_{1-x}In_x)_2O_3$,” Appl. Phys. Express, vol. 9, no. 4, p. 041102, Apr. 2016, doi: 10.7567/APEX.9.041102.

[114] H. Y. Playford, A. C. Hannon, E. R. Barney, and R. I. Walton, “Structures of uncharacterised polymorphs of gallium oxide from total neutron diffraction,” Chem. - A Eur. J., vol. 19, no. 8, pp. 2803–2813, Feb. 2013, doi: 10.1002/chem.201203359.

[115] F. Mezzadri, G. Calestani, F. Boschi, D. Delmonte, M. Bosi, and R. Fornari, "Crystal structure and ferroelectric properties of ϵ-Ga_2O_3 films grown on (0001)-sapphire," Inorg. Chem., vol. 55, no. 22, pp. 12079–12084, Nov. 2016, doi: 10.1021/acs.inorgchem.6b02244.

[116] Y. Cai et al., " Tin-assisted growth of ε-Ga_2O_3 film and the fabrication of photodetectors on sapphire substrate by PLD ," Opt. Mater. Express, vol. 8, no. 11, p. 3506, Nov. 2018, doi: 10.1364/ome.8.003506.

[117] D. Shinohara and S. Fujita, "Heteroepitaxy of corundum-structured α-Ga_2O_3thin films on α-Al_2O_3 substrates by ultrasonic mist chemical vapor deposition," Jpn. J. Appl. Phys., vol. 47, no. 9 PART 1, pp. 7311–7313, Sep. 2008, doi: 10.1143/JJAP.47.7311.

[118] J. W. Roberts et al., "Low temperature growth and optical properties of α-Ga_2O_3 deposited on sapphire by plasma enhanced atomic layer deposition," J. Cryst. Growth, vol. 528, p. 125254, Dec. 2019, doi: 10.1016/j.jcrysgro.2019.125254.

[119] M. Marezio and J. P. Remeika, "Bond lengths in the α-Ga_2O_3 structure and the high-pressure phase of $Ga_{2-x}Fe_xO_3$," J. Chem. Phys., vol. 46, no. 5, pp. 1862–1865, Mar. 1967, doi: 10.1063/1.1840945.

[120] R. Roy, V. G. Hill, and E. F. Osborn, "Polymorphism of Ga_2O_3 and the System Ga_2O_3-H_2O," 1952. Accessed: Aug. 21, 2018. [Online]. Available: https://pubs.acs.org/sharingguidelines.

[121] A. Sharma et al., "Nano-structured phases of gallium oxide (GaOOH, α-Ga_2O_3, β-Ga_2O_3, γ-Ga_2O_3, δ-Ga_2O_3, and ε-Ga_2O_3): fabrication, structural, and electronic structure investigations," Int. Nano Lett., vol. 10, no. 1, pp. 71–79, Mar. 2020, doi: 10.1007/s40089-020-00295-w.

[122] T. Onuma et al., "Correlation between blue luminescence intensity and resistivity in β-Ga_2O_3 single crystals," Cit. Appl. Phys. Lett, vol. 103, p. 41910, 2013, doi: 10.1063/1.4816759.

[123] N. Ueda, H. Hosono, R. Waseda, and H. Kawazoe, "Gallium oxide (Ga_2O_3) metal-semiconductor field-effect transistors on single-crystal-Ga_2O_3 (010) substrates," J. Chem. Phys., vol. 70, no. 3, p. 676, 1997, doi: 10.1063/1.1731237.

[124] D. B. C. and G. K. Hubler., “Oxygen vacancies and donor impurities in β-Ga_2O_3,” Appl. Phys. Lett., vol. 97, no. 14, p. 142106, Oct. 2010, doi: 10.1063/1.3499306.

[125] E. G. Víllora, K. Shimamura, Y. Yoshikawa, T. Ujiie, and K. Aoki, “Electrical conductivity and carrier concentration control in by Si doping,” Cit. Appl. Phys. Lett, vol. 92, p. 202120, 2008, doi: 10.1063/1.2919728.

[126] E. Chikoidze et al., “P-type β-gallium oxide: A new perspective for power and optoelectronic devices,” Mater. Today Phys., vol. 3, pp. 118–126, 2017, doi: 10.1016/j.mtphys.2017.10.002.

[127] K. Yamaguchi, “First principles study on electronic structure of β-Ga_2O_3,” Solid State Commun., vol. 131, no. 12, pp. 739–744, 2004, doi: 10.1016/j.ssc.2004.07.030.

[128] Y. P. Qian et al., “Mg-doped p -type β-Ga_2O_3 thin film for solar-blind ultraviolet photodetector,” Mater. Lett., vol. 209, pp. 558–561, Dec. 2017, doi: 10.1016/j.matlet.2017.08.052.

[129] X. H. Wang, F. B. Zhang, K. Saito, T. Tanaka, M. Nishio, and Q. X. Guo, “Electrical properties and emission mechanisms of Zn-doped β-Ga2O3 film,” J. Phys. Chem. Solids, vol. 75, no. 11, pp. 1201–1204, 2014, doi: 10.1016/j.jpcs.2014.06.005.

[130] S. Manandhar and C. V Ramana, “Direct, functional relationship between structural and optical properties in titaniumincorporated gallium oxide nanocrystalline thin films,” J. Chem. Phys., vol. 110, p. 676, 2017, doi: 10.1063/1.1731237.

[131] T. Oishi, Y. Koga, K. Harada, and M. Kasu, “High-mobility β-Ga_2O_3 single crystals grown by edge-defined film-fed growth method and their Schottky barrier diodes with Ni contact,” Appl. Phys. Express, vol. 8, no. 3, p. 031101, 2015, doi: 10.7567/APEX.8.031101.

[132] Z. Guo et al., “Anisotropic thermal conductivity in single crystal β-gallium oxide,” Cit. Appl. Phys. Lett, vol. 106, p. 111909, 2015, doi: 10.1063/1.4916078.

[133] T. Chen and K. Tang, “γ- Ga_2O_3 quantum dots with visible blue-green light emission property,” Appl. Phys. Lett., vol. 90, no. 5, p. 053104, Jan. 2007, doi: 10.1063/1.2437110.

[134] F.-P. Yu et al., “Pulsed laser deposition of gallium oxide films for high performance solar-blind photodetectors,” IEEE J. Sel. Top. Quantum Electron, vol. 10, no. 4, p. 103102, 2004, doi: 10.1364/OME.5.001240.

[135] L. M. Garten, A. Zakutayev, J. D. Perkins, B. P. Gorman, P. F. Ndione, and D. S. Ginley, “Structure property relationships in gallium oxide thin films grown by pulsed laser deposition,” MRS Commun., vol. 6, no. 04, pp. 348–353, Dec. 2016, doi: 10.1557/mrc.2016.50.

[136] S. Muller, H. Von Wenckstern, D. Splith, F. Schmidt, and M. Grundmann, “Control of the conductivity of Si-doped β-Ga_2O_3 thin films via growth temperature and pressure,” Phys. Status Solidi Appl. Mater. Sci., vol. 211, no. 1, pp. 34–39, 2014, doi: 10.1002/pssa.201330025.

[137] J. A. Greer, “History and current status of commercial pulsed laser deposition equipment Recent citations Enhanced Performance of Gadolinia-Doped Ceria Diffusion Barrier Layers Fabricated by Pulsed Laser Deposition for Large-Area Solid Oxide Fuel Cells Miguel Morales et al History and current status of commercial pulsed laser deposition equipment,” J. Phys. D Appl. Phys. J. Phys. D Appl. Phys, vol. 47, p. 10, 2014, doi: 10.1088/0022-3727/47/3/034005.

[138] C. Ngai Yui, “Study Of Barium Strontium Zirconate Titanate Thin Films And Their Microwave Device Applications,” no. January 2010, pp. 1–189, 2010.

[139] V. Serbezov, “Pulsed Laser Deposition: The Road to Hybrid Nanocomposites Coatings and Novel Pulsed Laser Adaptive Technique,” Recent Pat. Nanotechnol., vol. 7, no. 1, pp. 26–40, Nov. 2012, doi: 10.2174/1872210511307010026.

[140] D. C. and G. K. Hubler, “Pulsed laser deposition of thin films / edited by Douglas B. Chrisey and Graham K. Hubler. - Version details - Trove.” https://trove.nla.gov.au/work/10175783?q&versionId=11831285 (accessed Jun. 03, 2020).

[141] E. Gnecco, “Growth Modes.” Accessed: Jun. 03, 2020. [Online]. Available: https://nanolino.unibas.ch/pdf/surfacephysics/oberflaeche9.pdf.

[142] L. W. Martin, Y. H. Chu, and R. Ramesh, “Advances in the growth and characterization of magnetic, ferroelectric, and multiferroic oxide thin films,” Materials Science and Engineering R: Reports, vol. 68, no. 4–6. Elsevier Ltd, pp. 89–133, May 20, 2010, doi: 10.1016/j.mser.2010.03.001.

[143] F. Zhang, “Growth and characterization of Ga_2O_3 based wide bandgap semiconductor films,” 2016.

[144] G. Bracco and B. Holst, “Surface science techniques,” Springer Ser. Surf. Sci., vol. 51, no. 1, 2013, doi: 10.1007/978-3-642-34243-1.

[145] V. Von, “Controlled Deposition of Fullerenes: Effects of Topological nano-Modifications of a Surface on Aggregation and Growth Phenomena,” dissertation. https://www.researchgate.net/publication/329936003_Controlled_Deposition_of_Fullerenes_Effects_of_Topological_nanoModifications_of_a_Surface_on_Aggregation_and_Growth_Phenomena?channel=doi&linkId=5c24aa71458515a4c7fbbae3&showFulltext=true (accessed Jun. 03, 2020).

[146] F. C. Frank and J. H. van der Merwe, “One-Dimensional Dislocations. II. Misfitting Monolayers and Oriented Overgrowth,” Proceedings of the Royal Society of London. Series A, Mathematical and Physical Sciences, vol. 198. Royal Society, pp. 216–225, doi: 10.2307/98166.

[147] M. Volmer and A. Weber, “Keimbildung in übersättigten Gebilden,” Zeitschrift für Phys. Chemie, vol. 119U, no. 1, pp. 277–301, Jan. 1926, doi: 10.1515/zpch-1926-11927.

[148] W. Mu, Z. Jia, Y. Yin, and X. Tao, “Crystal growth and characterization of β-Ga_2O_3 single crystal,” vol. 184, no. 400, p. 250100, 2014.

[149] T. F. Hans J. Scheel, Crystal Growth Technology. .

[150] C. Ramsdale, “Ellipsometry What is Ellipsometry ?,” 2000.

[151] H. Fujiwara, Spectroscopic ellipsometry. 2007.

[152] “What is Ellipsometry ? Film thickness Refractive Index (n) Extinction Coefficient (k) Surface Roughness Anisotropy Retardation Phase Difference Birefringence Measure and.” Accessed: Aug. 17, 2018. [Online]. Available: http://www.sun-way.com.tw/Files/DownloadFile/Ellipsometry_basics.pdf.

[153] R. Synowicki, “Transparent Substrates : How To Suppress Reflections from the back surface,” JA Woollam, no. April, pp. 10–11, 2010.

[154] L. Meitner, “Über die Entstehung der β-Strahl-Spektren radioaktiver Substanzen,” vol. 9, no. 1, pp. 131–144, 1922, Accessed: Aug. 19, 2018. [Online]. Available: http://www.eagle-regpot.eu/EAgLE-Equipment_XPS.html.

[155] J. M. Lafferty, “Foundations of Vacuum Science and Technology | Wiley.” https://www.wiley.com/enus/Foundations+of+Vacuum+Science+and+Technology-p-9780471175933 (accessed Jun. 04, 2020).

[156] B. M. Weckhuysen, “CHAPTER 12 Ultraviolet-Visible Spectroscopy,” pp. 255–270, 2004.

[157] “U V Introduction to Ultraviolet-Visible Spectroscopy 1 (UV) Background Theory,” 2009. Accessed: Aug. 20, 2018. [Online]. Available: http://www.chemguide.co.uk/analysis/uvvisiblemenu.html#top.

[158] B. Law, “Sample Cell Selection Guide for Spectroscopy Applications,” p. 92910, 2014.

[159] P. W. Peter Eaton, Atomic Force Microscopy. .

[160] C. Zeng, C. Vitale-Sullivan, X. Ma, C. Zeng, C. Vitale-Sullivan, and X. Ma, “In Situ Atomic Force Microscopy Studies on Nucleation and Self-Assembly of Biogenic and Bio-Inspired Materials,” Minerals, vol. 7, no. 9, p. 158, Aug. 2017, doi: 10.3390/min7090158.

[161] “Atomic Force Microscopy - Nanoscience Instruments.”https://www.nanoscience.com/techniques/atomic-force-microscopy/ (accessed Aug. 20, 2018).

[162] P. F. Mode, “Atomic Force Microscopy,” Time, no. May 2017, 2000, doi: 10.1063/1.881238.

[163] L. M. Garten, A. Zakutayev, J. D. Perkins, B. P. Gorman, P. F. Ndione, and D. S. Ginley, “Structure property relationships in gallium oxide thin films grown by pulsed laser deposition,” MRS Commun., vol. 6, no. 4, pp. 348–353, Dec. 2016, doi: 10.1557/mrc.2016.50.

[164] R. Wakabayashi et al., “Oxygen-radical-assisted pulsed-laser deposition of β-Ga_2O_3 and β-$(Al_xGa_{1-x})_2O_3$ films,” J. Cryst. Growth, vol. 424, pp. 77–79, Jun. 2015, doi: 10.1016/j.jcrysgro.2015.05.005.

[165] A. Goyal, B. S. Yadav, O. P. Thakur, A. K. Kapoor, and R. Muralidharan, “Effect of annealing on β-Ga_2O_3 film grown by pulsed laser deposition technique,” J. Alloys Compd., vol. 583, pp. 214–219, Jan. 2014, doi: 10.1016/j.jallcom.2013.08.115.

[166] F. B. Zhang, K. Saito, T. Tanaka, M. Nishio, and Q. X. Guo, “Structural and optical properties of Ga2O3 films on sapphire substrates by pulsed laser deposition,” J. Cryst. Growth, vol. 387, pp. 96–100, Feb. 2014, doi: 10.1016/j.jcrysgro.2013.11.022.

[167] S. L. Ou et al., “Growth and etching characteristics of gallium oxide thin films by pulsed laser deposition,” Mater. Chem. Phys., vol. 133, no. 2–3, pp. 700–705, Apr. 2012, doi: 10.1016/j.matchemphys.2012.01.060.

[168] M. Ogita, N. Saika, Y. Nakanishi, Y. H.-A. S. Sci, and undefined 1999, “Design and performance of a simple, room-temperature Ga_2O_3 nanowire gas sensor.”

[169] K. Sasaki, A. Kuramata, T. Masui, E. G. Víllora, K. Shimamura, and S. Yamakoshi, “Device-quality β-Ga_2O_3 epitaxial films fabricated by ozone molecular beam epitaxy,” Appl. Phys. Express, vol. 5, no. 3, p. 035502, Mar. 2012, doi: 10.1143/APEX.5.035502.

[170] K. Sasaki, M. Higashiwaki, A. Kuramata, T. Masui, and S. Yamakoshi, “Growth temperature dependences of structural and electrical properties of Ga_2O_3 epitaxial films grown on β-Ga_2O_3 (010) substrates by molecular beam epitaxy,” J. Cryst. Growth, vol. 392, pp. 30–33, Apr. 2014, doi: 10.1016/j.jcrysgro.2014.02.002.

[171] S. Ghose et al., “Growth and characterization of β-Ga_2O_3 thin films by molecular beam epitaxy for deep-UV photodetectors,” J. Appl. Phys., vol. 122, no. 9, p. 095302, Sep. 2017, doi: 10.1063/1.4985855.

[172] A. Arias et al., “Structural, Optical, and Electrical Characterization of β-Ga_2O_3 Thin Films Grown by Plasma-Assisted Molecular Beam Epitaxy Suitable for UV Sensing,” 2018, doi: 10.1155/2018/9450157.

[173] S. Ghose et al., “Structural and optical properties of β-Ga_2O_3thin films grown by plasma-assisted molecular beam epitaxy,” J. Vac. Sci. Technol. B, Nanotechnol. Microelectron. Mater. Process. Meas. Phenom., vol. 34, no. 2, p. 02L109, Mar. 2016, doi: 10.1116/1.4942045.

[174] P. Vogt and O. Bierwagen, “Reaction kinetics and growth window for plasma-assisted molecular beam epitaxy of Ga_2O_3: Incorporation of Ga vs. Ga_2O desorption,” Appl. Phys. Lett., vol. 108, no. 7, p. 072101, Feb. 2016, doi: 10.1063/1.4942002.

[175] X. Z. Liu, P. Guo, T. Sheng, L. X. Qian, W. L. Zhang, and Y. R. Li, “β-Ga_2O_3 thin films on sapphire pre-seeded by homo-self-templated buffer layer for solar-blind UV photodetector,” Opt. Mater. (Amst)., vol. 51, pp. 203–207, Jan. 2016, doi: 10.1016/j.optmat.2015.11.023.

[176] E. G. Víllora, K. Shimamura, K. Kitamura, and K. Aoki, “Rf-plasma-assisted molecular-beam epitaxy of β-Ga_2O_3,” Appl. Phys. Lett., vol. 88, no. 3, pp. 1–3, Jan. 2006, doi: 10.1063/1.2164407.

[177] H.-S. Yoo and Y. Kim, “Chemical Vapor Deposition of Ga_2O_3 Thin Films on Si Substrates,” researchgate.net, vol. 23, no. 2, pp. 225–228, Feb. 2002, doi: 10.5012/bkcs.2002.23.2.225.

[178] S. Rafique, L. Han, M. J. Tadjer, J. A. Freitas, N. A. Mahadik, and H. Zhao, “Homoepitaxial growth of β-Ga_2O_3 thin films by low pressure chemical vapor deposition,” Appl. Phys. Lett., vol. 108, no. 18, p. 182105, May 2016, doi: 10.1063/1.4948944.

[179] D. J. Comstock and J. W. Elam, “Atomic layer deposition of Ga_2O_3 films using trimethylgallium and ozone,” Chem. Mater., vol. 24, no. 21, pp. 4011–4018, Nov. 2012, doi: 10.1021/cm300712x.

[180] M. Higashiwaki et al., “Temperature-dependent capacitance-voltage and current-voltage characteristics of Pt/Ga_2O_3 (001) Schottky barrier diodes fabricated on n-Ga_2O_3 drift layers grown by halide vapor phase epitaxy,” Appl. Phys. Lett., vol. 108, no. 13, p. 133503, Mar. 2016, doi: 10.1063/1.4945267.

[181] Y. OHYA, J. OKANO, Y. KASUYA, and T. BAN, “Fabrication of Ga_2O_3 thin films by aqueous solution deposition,” J. Ceram. Soc. Japan, vol. 117, no. 1369, pp. 973–977, 2009, doi: 10.2109/jcersj2.117.973.

[182] D. Gogova, M. Schmidbauer, and A. Kwasniewski, “Homo- and heteroepitaxial growth of Sn-doped β-Ga_2O_3 layers by MOVPE,” CrystEngComm, vol. 17, no. 35, pp. 6744–6752, Aug. 2015, doi: 10.1039/c5ce01106j.

[183] M. Higashiwaki, K. Sasaki, A. Kuramata, T. Masui, and S. Yamakoshi, “Gallium oxide (Ga_2O_3) metal-semiconductor field-effect transistors on single-crystal β-Ga_2O_3 (010) substrates,” Appl. Phys. Lett., vol. 100, no. 1, p. 013504, Jan. 2012, doi: 10.1063/1.3674287.

[184] B. W. Krueger, C. S. Dandeneau, E. M. Nelson, S. T. Dunham, F. S. Ohuchi, and M. A. Olmstead, “Variation of Band Gap and Lattice Parameters of β−$(Al_xGa_{1-x})_2O_3$ Powder Produced by Solution Combustion Synthesis,” J. Am. Ceram. Soc., vol. 99, no. 7, pp. 2467–2473, Jul. 2016, doi: 10.1111/jace.14222.

[185] Q. Feng et al., “$(AlGa)_2O_3$ solar-blind photodetectors on sapphire with wider bandgap and improved responsivity,” Opt. Mater. Express, vol. 7, no. 4, p. 1240, Apr. 2017, doi: 10.1364/ome.7.001240.

[186] F. Zhang, K. Saito, T. Tanaka, M. Nishio, M. Arita, and Q. Guo, “Wide bandgap engineering of $(AlGa)_2O_3$ films,” Appl. Phys. Lett., vol. 105, no. 16, p. 162107, Oct. 2014, doi: 10.1063/1.4900522.

[187] T. Wang, W. Li, C. Ni, and A. Janotti, “Band Gap and Band Offset of Ga_2O_3 and $(Al_xGa_{1-x})_2O_3$ Alloys,” Phys. Rev. Appl., vol. 10, no. 1, p. 011003, Jul. 2018, doi: 10.1103/PhysRevApplied.10.011003.

[188] A. E. Romanov, S. I. Stepanov, V. I. Nikolaev, and V. E. Bougrov, “GALLIUM OXIDE: PROPERTIES AND APPLICA A REVIEW,” 2016. Accessed: Aug. 28, 2019. [Online]. Available: http://www.ipme.ru/e-journals/RAMS/no_14416/06_14416_stepanov.pdf.

[189] T. Aoyama, Y. Oka, K. Honda, and C. Mori, “A neutron detector using silicon PIN photodiodes for personal neutron dosimetry,” Phys. Res. Sect. Nucl. Instruments Methods Phys. Res., vol. 314, pp. 590–594, 1992.

[190] J. Kim et al., “Radiation damage effects in Ga_2O_3 materials and devices,” Journal of Materials Chemistry C, vol. 7, no. 1. Royal Society of Chemistry, pp. 10–24, 2019, doi: 10.1039/c8tc04193h.

[191] C. Tang et al., “Electronic structure and optical property of metal-doped Ga_2O_3: A first principles study,” RSC Adv., vol. 6, no. 82, pp. 78322–78334, 2016, doi: 10.1039/c6ra14010f.

[192] P. Barpanda et al., “Supplementary material (ESI) for Structure and electrochemical properties of novel mixed $Li(Fe_{1-x} M_x)SO_4F$(M = Co, Ni, Mn) phases fabricated by low temperature ionothermal synthesis †,” 2010.

[193] A. Kaphle and P. Hari, “Variation of index of refraction in cobalt doped ZnO nanostructures,” J. Appl. Phys., vol. 122, no. 16, p. 165304, Oct. 2017, doi: 10.1063/1.5001713.

[194] F. B. Zhang, K. Saito, T. Tanaka, M. Nishio, and Q. X. Guo, “Structural and optical properties of Ga_2O_3 films on sapphire substrates by pulsed laser deposition,” J. Cryst. Growth, vol. 387, pp. 96–100, Feb. 2014, doi: 10.1016/j.jcrysgro.2013.11.022.

[195] Y. Lv, J. Ma, W. Mi, C. Luan, Z. Zhu, and H. Xiao, “Characterization of Ga_2O_3 3 thin films on sapphire (0001) using metal-organic chemical vapor deposition technique,” Vacuum, vol. 86, no. 12, pp. 1850–1854, Jul. 2012, doi: 10.1016/j.vacuum.2012.04.019.

[196] S. R. Thomas et al., “High electron mobility thin-film transistors based on Ga_2O_3 grown by atmospheric ultrasonic spray pyrolysis at low temperatures,” Appl. Phys. Lett., vol. 105, no. 9, p. 092105, Sep. 2014, doi: 10.1063/1.4894643.

[197] T. Wang et al., “Indirect to direct bandgap transition in methylammonium lead halide perovskite,” 2016.

[198] B. D. Viezbicke, S. Patel, B. E. Davis, and D. P. Birnie, “Evaluation of the Tauc method for optical absorption edge determination: ZnO thin films as a model system,” Phys. status solidi, vol. 252, no. 8, pp. 1700–1710, Aug. 2015, doi: 10.1002/pssb.201552007.

[199] S. S. Kumar et al., “Structure, morphology, and optical properties of amorphous and nanocrystalline gallium oxide thin films,” J. Phys. Chem. C, vol. 117, no. 8, pp. 4194–4200, Feb. 2013, doi: 10.1021/jp311300e.

[200] T. Onuma et al., “Spectroscopic ellipsometry studies on Ga_2O_3 films and single crystal,” in Japanese Journal of Applied Physics, Dec. 2016, vol. 55, no. 12, p. 1202B2, doi: 10.7567/JJAP.55.1202B2.

[201] R. M. A. Azzam and N. M. Bashara, Ellipsometry and polarized light, Paperback ed. Amsterdam ;;New York: North-Holland, 1987.

[202] M. Rebien, W. Henrion, M. Hong, J. P. Mannaerts, and M. Fleischer, “Optical properties of gallium oxide thin films,” Appl. Phys. Lett., vol. 81, no. 2, pp. 250–252, Jul. 2002, doi: 10.1063/1.1491613.

[203] C. Sturm, R. Schmidt-Grund, C. Kranert, J. Furthmüller, F. Bechstedt, and M. Grundmann, “Dipole analysis of the dielectric function of color dispersive materials: Application to monoclinic Ga_2O_3,” Phys. Rev. B, vol. 94, no. 3, p. 035148, Jul. 2016, doi: 10.1103/PhysRevB.94.035148.

[204] G. E. Jellison, Jr, “Spectroscopic ellipsometry data analysis: measured versus calculated quantities,” Thin Solid Films, vol. 313–314, pp. 33–39, Feb. 1998, doi: 10.1016/s0040-6090(97)00765-7.

[205] C. V. Ramana et al., “Chemical bonding, optical constants, and electrical resistivity of sputter-deposited gallium oxide thin films,” J. Appl. Phys., vol. 115, no. 4, p. 043508, Jan. 2014, doi: 10.1063/1.4862186.

[206] R. Manigandan, K. Giribabu, R. Suresh, L. Vijayalakshmi, A. Stephen, and V. Narayanan, “Structural, optical and magnetic properties of gadolinium sesquioxide nanobars synthesized via thermal decomposition of gadolinium oxalate,” Mater. Res. Bull., vol. 48, no. 10, pp. 4210–4215, Oct. 2013, doi: 10.1016/j.materresbull.2013.06.067.

[207] G. van der Laan, E. Arenholz, E. Navas, A. Bauer, and G. Kaindl, “Magnetic circular dichroism and orbital momentum coupling in photoemission from Gd(0001),” Phys. Rev. B - Condens. Matter Mater. Phys., vol. 53, no. 10, pp. R5998–R6001, Mar. 1996, doi: 10.1103/PhysRevB.53.R5998.

[208] S. P. Pavunny et al., “Structural and electrical properties of lanthanum gadolinium oxide: Ceramic and thin films for high-k application,” in Integrated Ferroelectrics, 2011, vol. 125, no. 1, pp. 44–52, doi: 10.1080/10584587.2011.574039.

[209] Y. Pan, J. Yang, Y. Fang, J. Zheng, R. Song, and C. Yi, “One-pot synthesis of gadolinium-doped carbon quantum dots for high-performance multimodal bioimaging,” J. Mater. Chem. B, vol. 5, no. 1, pp. 92–101, Dec. 2017, doi: 10.1039/c6tb02115h.

[210] Z. Azdad, L. Marot, L. Moser, R. Steiner, and E. Meyer, “Valence band behaviour of zirconium oxide, Photoelectron and Auger spectroscopy study OPEN,” Sci. REPoRTS |, vol. 8, p. 16251, 2018, doi: 10.1038/s41598-018-34570-w.

[211] K. Wright and A. Barron, “Catalyst Residue and Oxygen Species Inhibition of the Formation of Hexahapto-Metal Complexes of Group 6 Metals on Single-Walled Carbon Nanotubes,” C, vol. 3, no. 4, p. 17, May 2017, doi: 10.3390/c3020017.

[212] M. Higashiwaki and G. H. Jessen, “Guest Editorial: The dawn of gallium oxide microelectronics,” Applied Physics Letters, vol. 112, no. 6. American Institute of Physics Inc., p. 060401, Feb. 05, 2018, doi: 10.1063/1.5017845.

[213] S. Bhandari, M. E. Zvanut, and J. B. Varley, “Optical absorption of Fe in doped Ga_2O_3,” J. Appl. Phys., vol. 126, no. 16, p. 165703, Oct. 2019, doi: 10.1063/1.5124825.

[214] A. Mauze, Y. Zhang, T. Mates, F. Wu, and J. S. Speck, “Investigation of unintentional Fe incorporation in (010) β-Ga_2O_3 films grown by plasma-assisted molecular beam epitaxy,” Appl. Phys. Lett., vol. 115, no. 5, p. 052102, Jul. 2019, doi: 10.1063/1.5096183.

[215] I. Hany et al., “Low temperature cathodoluminescence study of Fe-doped β-Ga_2O_3,” Mater. Lett., vol. 257, p. 126744, Dec. 2019, doi: 10.1016/j.matlet.2019.126744.

[216] A. D. K. Marko J. Tadjer, z John L. Lyons, Neeraj Nepal, Jaime A. Freitas Jr. and and G. M. Foster, “Review-Theory and Characterization of Doping and Defects in β-Ga_2O_3,” 2016, doi: 10.1149/2.0341907jss.

[217] S. J. Pearton et al., “A review of Ga_2O_3 materials, processing, and devices,” Applied Physics Reviews, vol. 5, no. 1. American Institute of Physics Inc., p. 011301, Mar. 01, 2018, doi: 10.1063/1.5006941.

[218] S. J. Pearton et al., “A review of Ga_2O_3 materials, processing, and devices ARTICLES YOU MAY BE INTERESTED IN,” Appl. Phys. Rev, vol. 5, p. 11301, 2018, doi: 10.1063/1.5006941.

[219] F. Alema et al., “Solar blind photodetector based on epitaxial zinc doped Ga_2O_3thin film,” Phys. status solidi, vol. 214, no. 5, p. 1600688, May 2017, doi: 10.1002/pssa.201600688.

[220] X. H. Wang, F. B. Zhang, K. Saito, T. Tanaka, M. Nishio, and Q. X. Guo, “Electrical properties and emission mechanisms of Zn-doped Ga_2O_3 films,” J. Phys. Chem. Solids, vol. 75, no. 11, pp. 1201–1204, Nov. 2014, doi: 10.1016/j.jpcs.2014.06.005.

[221] M. Handwerg, R. Mitdank, Z. Galazka, and S. F. Fischer, “Temperature-dependent thermal conductivity and diffusivity of a Mg-doped insulating Ga_2O_3 single crystal along [100], [010] and [001],” Semicond. Sci. Technol., vol. 31, no. 12, p. 125006, Nov. 2016, doi: 10.1088/0268-1242/31/12/125006.

[222] Y. P. Qian et al., “Mg-doped p-type Ga_2O_3thin film for solar-blind ultraviolet photodetector,” Mater. Lett., vol. 209, pp. 558–561, Dec. 2017, doi: 10.1016/j.matlet.2017.08.052.

[223] A. Y. Polyakov et al., “Electrical properties of bulk semi-insulating Ga_2O_3 (Fe),” Appl. Phys. Lett., vol. 113, no. 14, p. 142102, Oct. 2018, doi: 10.1063/1.5051986.

[224] H. He, W. Li, H. Xing, and E. Liang, “First principles study on the electronic properties of Cr, Fe, Mn and Ni doped Ga_2O_3,” 2012, doi: 10.4028/www.scientific.net/AMR.535-537.36.

[225] Z. Galazka et al., “On the bulk Ga_2O_3 single crystals grown by the Czochralski method,” J. Cryst. Growth, vol. 404, pp. 184–191, Oct. 2014, doi: 10.1016/j.jcrysgro.2014.07.021.

[226] Y. Huang et al., “High-insulating β-Ga_2O_3 thin films by doping with a valence controllable Fe element,” Appl. Phys. A Mater. Sci. Process., vol. 124, no. 9, pp. 1–9, Sep. 2018, doi: 10.1007/s00339-018-2037-z.

[227] S. Mukherjee, A. Roy, S. Auluck, R. Prasad, R. Gupta, and A. Garg, “Room temperature nanoscale ferroelectricity in magnetoelectric $GaFeO_3$ epitaxial thin films,” Phys. Rev. Lett., vol. 111, no. 8, p. 087601, Aug. 2013, doi: 10.1103/PhysRevLett.111.087601.

[228] T. Katayama et al., “Ferroelectric and Magnetic Properties in Room-Temperature Multiferroic $Ga_xFe_{2-x}O_3$ Epitaxial Thin Films,” Adv. Funct. Mater., vol. 28, no. 2, p. 1704789, Jan. 2018, doi: 10.1002/adfm.201704789.

[229] S. H. Oh, J. H. Lee, R. H. Shin, Y. Shin, C. Meny, and W. Jo, “Room-temperature polarization switching and antiferromagnetic coupling in epitaxial $(Ga,Fe)_2O_3/SrRuO_3$ heterostructures,” Appl. Phys. Lett., vol. 106, no. 14, p. 142902, Apr. 2015, doi: 10.1063/1.4917249.

[230] Y. Hamasaki, T. Shimizu, H. Taniguchi, T. Taniyama, S. Yasui, and M. Itoh, “Epitaxial growth of metastable multiferroic $AlFeO_3$ film on SrTiO3 (111) substrate,” Appl. Phys. Lett., vol. 104, no. 8, p. 082906, Feb. 2014, doi: 10.1063/1.4866798.

[231] M. Gich et al., “Multiferroic Iron Oxide Thin Films at Room Temperature,” Adv. Mater., vol. 26, no. 27, pp. 4645–4652, Jul. 2014, doi: 10.1002/adma.201400990.

[232] W. Kim, J. H. We, S. J. Kim, and C. S. Kim, “Effects of cation distribution for $AFeO_3$ (A=Ga,Al),” in Journal of Applied Physics, May 2007, vol. 101, no. 9, p. 09M515, doi: 10.1063/1.2712819.

[233] M. B. Mohamed, A. Senyshyn, H. Ehrenberg, and H. Fuess, “Structural, magnetic, dielectric properties of multiferroic $GaFeO_3$ prepared by solid state reaction and sol-gel methods,” Journal of Alloys and Compounds, vol. 492, no. 1–2. pp. L20–L27, Mar. 04, 2010, doi: 10.1016/j.jallcom.2009.11.099.

[234] T. Arima et al., “Structural and magnetoelectric properties of $Ga_{2-x}Fe_xO_3$ single crystals grown by a floating-zone method,” Phys. Rev. B - Condens. Matter Mater. Phys., vol. 70, no. 6, p. 064426, Aug. 2004, doi: 10.1103/PhysRevB.70.064426.

[235] A. B. and V. G. S. Kavita Sharma, V Raghavendra Reddy1, Deepti Kothari, Ajay Gupta, “Low temperature Raman and high field 57Fe Mossbauer study of polycrystalline $GaFeO_3$,” J. Phys. Condens. Matter, Mar. 2010, doi: 10.1088/0953-8984.

[236] A. B. and A. M. A. Kavita Sharma, V Raghavendra Reddy, Ajay Gupta, "Magnetic and 57Fe Mössbauer study of magneto-electric $GaFeO_3$ prepared by the sol–gel route," J. Phys. Condens. Matter, Jan. 2013, doi: 10.1088/0953-8984.

[237] Z. H. Sun, S. Dai, Y. L. Zhou, L. Z. Cao, and Z. H. Chen, "Elaboration and optical properties of $GaFeO_3$ thin films," Thin Solid Films, vol. 516, no. 21, pp. 7433–7436, Sep. 2008, doi: 10.1016/j.tsf.2008.02.054.

[238] Z. H. Sun, Y. L. Zhou, S. Y. Dai, L. Z. Cao, and Z. H. Chen, "Preparation and properties of $GaFeO_3$ thin films grown at various oxygen pressures by pulsed laser deposition," Appl. Phys. A Mater. Sci. Process., vol. 91, no. 1, pp. 97–100, Apr. 2008, doi: 10.1007/s00339-007-4364-3.

[239] M. Trassin et al., "Room temperature ferrimagnetic thin films of the magnetoelectric $Ga_{2-x}Fe_xO_3$," J. Mater. Chem., vol. 19, no. 46, pp. 8876–8880, Nov. 2009, doi: 10.1039/b913359c.

[240] M. Trassin et al., "Epitaxial thin films of multiferroic $GaFeO_3$ on conducting indium tin oxide (001) buffered yttrium-stabilized zirconia (001) by pulsed laser deposition," Appl. Phys. Lett., vol. 91, no. 20, p. 202504, Nov. 2007, doi: 10.1063/1.2813020.

[241] D. C. Kundaliya et al., "Large second-harmonic kerr rotation in $GaFeO_3$ thin films on YSZ buffered silicon," J. Magn. Magn. Mater., vol. 299, no. 2, pp. 307–311, Apr. 2006, doi: 10.1016/j.jmmm.2005.04.017.

[242] D. Guo et al., "Epitaxial growth and magnetic properties of ultraviolet transparent $Ga_2O_3/(Ga_{1-x}Fe_x)_2O_3$ multilayer thin films," Sci. Rep., vol. 6, no. 1, pp. 1–7, Jul. 2016, doi: 10.1038/srep25166.

[243] K. Sharma, V. Raghavendra Reddy, A. Gupta, R. J. Choudhary, D. M. Phase, and V. Ganesan, "Study of site-disorder in epitaxial magneto-electric $GaFeO_3$ thin films," Appl. Phys. Lett., vol. 102, no. 21, p. 212401, May 2013, doi: 10.1063/1.4807757.

[244] J. C. A. Huang, H. S. Hsu, Y. M. Hu, C. H. Lee, Y. H. Huang, and M. Z. Lin, "Origin of ferromagnetism in ZnO/CoFe multilayers: Diluted magnetic semiconductor or clustering effect," Appl. Phys. Lett., vol. 85, no. 17, pp. 3815–3817, Oct. 2004, doi: 10.1063/1.1812844.

[245] J. Chovan, E. G. Kavousanaki, and I. E. Perakis, “Ultrafast light-induced magnetization dynamics in ferromagnetic semiconductors,” Phys. Rev. Lett., vol. 96, no. 5, Aug. 2005, doi: 10.1103/PhysRevLett.96.057402.

[246] H. Toyosaki et al., “Anomalous Hall effect governed by electron doping in a room-temperature transparent ferromagnetic semiconductor,” Nat. Mater., vol. 3, no. 4, pp. 221–224, Mar. 2004, doi: 10.1038/nmat1099.

[247] S. Zhang et al., “Enhancement of longitudinal magneto-optical Kerr effect in HfO_2/Co/HfO_2/Al/silicon thin films,” Opt. Commun., vol. 321, pp. 226–229, Jun. 2014, doi: 10.1016/j.optcom.2014.02.010.

[248] W. Zheng, A. T. Hanbicki, B. T. Jonker, and G. Lüpke, “Control of magnetic contrast with nonlinear magneto-plasmonics,” Sci. Rep., vol. 4, no. 1, pp. 1–5, Aug. 2014, doi: 10.1038/srep06191.

[249] S. Yan, K. Liu, G. Lv, and Z. Fan, “Fluorine doping inducing high temperature ferromagnetism in $(In_{1-x}Fe_x)_2O_3$,” J. Alloys Compd., vol. 551, pp. 40–43, Feb. 2013, doi: 10.1016/j.jallcom.2012.10.024.

[250] M. Ji, X. Zhang, J. Wang, and S. E. Park, “Ethylbenzene dehydrogenation with CO_2 over Fe-doped $MgAl_2O_4$ spinel catalysts: Synergy effect between Fe^{2+} and Fe^{3+},” J. Mol. Catal. A Chem., vol. 371, pp. 36–41, May 2013, doi: 10.1016/j.molcata.2013.01.025.

[251] T. Yamashita and P. Hayes, “Analysis of XPS spectra of Fe^{2+} and Fe^{3+} ions in oxide materials,” Appl. Surf. Sci., vol. 254, no. 8, pp. 2441–2449, Feb. 2008, doi: 10.1016/j.apsusc.2007.09.063.

[252] I. Uhlig, R. Szargan, H. W. Nesbitt, and K. Laajalehto, “Surface states and reactivity of pyrite and marcasite,” Appl. Surf. Sci., vol. 179, no. 1–4, pp. 222–229, Jul. 2001, doi: 10.1016/S0169-4332(01)00283-5.

[253] M. C. Biesinger, B. P. Payne, A. P. Grosvenor, L. W. Lau, A. R. Gerson, and R. StC Smart, “Resolving surface chemical states in XPS analysis of first row transition metals, oxides and hydroxides: Cr, Mn, Fe, Co and Ni,” Appl. Surf. Sci., vol. 257, pp. 2717–2730, 2010, doi: 10.1016/j.apsusc.2010.10.051.

[254] S. J. Roosendaal, B. Van Asselen, J. W. Elsenaar, A. M. Vredenberg, and F. H. P. M. Habraken, “The oxidation state of Fe(100) after initial oxidation in O_2,” Surf. Sci., vol. 442, no. 3, pp. 329–337, Dec. 1999, doi: 10.1016/S0039-6028(99)01006-7.

[255] R. D. Shannon, “Revised effective ionic radii and systematic studies of interatomic distances in halides and chalcogenides,” Acta Crystallogr. Sect. A, vol. 32, no. 5, pp. 751–767, Sep. 1976, doi: 10.1107/S0567739476001551.

[256] Z. Wu et al., “Deep ultraviolet photoconductive and near-infrared luminescence properties of Er^{3+}-doped β-Ga_2O_3 thin films,” Appl. Phys. Lett., vol. 108, no. 21, p. 211903, May 2016, doi: 10.1063/1.4952618.

[257] D. Guo et al., “Room temperature ferromagnetism in $(Ga_{1-x}Mn_x)_2O_3$ epitaxial thin films,” J. Mater. Chem. C, vol. 3, no. 8, pp. 1830–1834, Feb. 2015, doi: 10.1039/c4tc02833c.

[258] E. J. L. Hao He, Wei Li, Huai Zhong Xing, “First Principles Study on the Electronic Properties of Cr, Fe, Mn and Ni Doped β-Ga_2O_3 | Scientific.Net.” https://www.scientific.net/AMR.535-537.36 (accessed May 01, 2020).

[259] A. Luque and A. Martí, “Increasing the Efficiency of Ideal Solar Cells by Photon Induced Transitions at Intermediate Levels,” Phys. Rev. Lett., vol. 78, no. 26, pp. 5014–5017, Nov. 1997, doi: 10.1103/PhysRevLett.78.5014.

[260] C. Tablero and P. Wahnón, “Analysis of metallic intermediate-band formation in photovoltaic materials,” Appl. Phys. Lett., vol. 82, no. 1, pp. 151–153, Jan. 2003, doi: 10.1063/1.1535744.

[261] S. S. C. 133 (2005) 97 C. Tablero, “Nanostructured Materials for Solar Energy Conversion - Google Books.”

[262] D. H. Kim, W. Lee, and J. M. Myoung, “Flexible multi-wavelength photodetector based on porous silicon nanowires,” Nanoscale, vol. 10, no. 37, pp. 17705–17711, Oct. 2018, doi: 10.1039/c8nr05096a.

[263] “P. D. Borges and L. Scolfaro, private communication. First principles DFT calculations were performed for monoclinic $Ga_2Fe_xO_3$, for x varying from 0 to 0.30, using VASP-PAW and the GGA+mBJ approximation for the exchange-correlation functional. A Hubbard U,” [Online]. Available: potential was added to the Fe when simulating the different Fe concentrations. Details will be published elsewhere.

[264] M. Rebien, W. Henrion, M. Hong, J. P. Mannaerts, and M. Fleischer, “Optical properties of gallium oxide thin films,” Appl. Phys. Lett., vol. 81, no. 2, pp. 250–252, Jul. 2002, doi: 10.1063/1.1491613.

[265] A. E. Romanov, S. I. Stepanov, V. I. Nikolaev, and V. E. Bougrov, “GALLIUM OXIDE: PROPERTIES AND APPLICA A REVIEW,” 2016.

[266] S. Ghose et al., “Structural and optical properties of β-Ga_2O_3 thin films grown by plasma-assisted molecular beam epitaxy,” J. Vac. Sci. Technol. B, Nanotechnol. Microelectron. Mater. Process. Meas. Phenom., vol. 34, no. 2, p. 02L109, Mar. 2016, doi: 10.1116/1.4942045.

[267] M. Rebien, W. Henrion, M. Hong, J. P. Mannaerts, and M. Fleischer, “Optical properties of gallium oxide thin films,” 2002, doi: 10.1063/1.1491613.

[268] T. Oshima, T. Nakazono, A. Mukai, and A. Ohtomo, “Epitaxial growth of γ-Ga_2O_3 films by mist chemical vapor deposition,” J. Cryst. Growth, vol. 359, no. 1, pp. 60–63, Nov. 2012, doi: 10.1016/j.jcrysgro.2012.08.025.

[269] D. Guo et al., “Magnetic anisotropy and deep ultraviolet photoresponse characteristics in Ga_2O_3:Cr vermicular nanowire thin film nanostructure,” RSC Adv., vol. 5, no. 17, pp. 12894–12898, 2015, doi: 10.1039/c4ra13813a.

[270] S. A. Wolf et al., “Spintronics: A spin-based electronics vision for the future,” Science, vol. 294, no. 5546. pp. 1488–1495, Nov. 16, 2001, doi: 10.1126/science.1065389.

[271] F. Pulizzi, “The rise of semiconductor spintronics,” Nat. Phys., vol. 4, no. S1, pp. S20–S20, Feb. 2008, doi: 10.1038/nphys878.

[272] S. B. Ogale, “Dilute doping, defects, and ferromagnetism in metal oxide systems,” Advanced Materials, vol. 22, no. 29. pp. 3125–3155, Aug. 03, 2010, doi: 10.1002/adma.200903891.

[273] L. Nagarajan et al., “A chemically driven insulator-metal transition in non-stoichiometric and amorphous gallium oxide,” Nat. Mater., 2008, doi: 10.1038/nmat2164.

[274] D. Y. Guo et al., “Oxygen vacancy tuned Ohmic-Schottky conversion for enhanced performance in - Ga_2O_3 solar-blind ultraviolet photodetectors,” Appl. Phys. Lett., 2014, doi: 10.1063/1.4890524.

[275] H. Hayashi et al., “Room temperature ferromagnetism in Mn-doped γ-Ga_2O_3 with spinel structure,” Appl. Phys. Lett., vol. 89, no. 18, p. 181903, Oct. 2006, doi: 10.1063/1.2369541.

[276] T. Katayama, S. Yasui, Y. Hamasaki, and M. Itoh, “Control of crystal-domain orientation in multiferroic $Ga_{0.6}Fe_{1.4}O_3$ epitaxial thin films,” Appl. Phys. Lett., vol. 110, no. 21, p. 212905, May 2017, doi: 10.1063/1.4984211.

[277] H. J. HOOK, “Thermal Stability of Gallium Orthoferrite in the System Fe_2O_3-FeO-Ga_2O_3,” J. Am. Ceram. Soc., vol. 48, no. 9, pp. 470–472, Sep. 1965, doi: 10.1111/j.1151-2916.1965.tb14801.x.

[278] S. D. Lee, Y. Ito, K. Kaneko, and S. Fujita, “Enhanced thermal stability of alpha gallium oxide films supported by aluminum doping,” Jpn. J. Appl. Phys., vol. 54, no. 3, Mar. 2015, doi: 10.7567/JJAP.54.030301.

[279] I. Cora et al., “The real structure of ε-Ga_2O_3 and its relation to κ-phase,” CrystEngComm, vol. 19, no. 11, pp. 1509–1516, Mar. 2017, doi: 10.1039/c7ce00123a.

[280] S. Krishnamoorthy, Z. Xia, S. Bajaj, M. Brenner, and S. Rajan, “Delta-doped β-gallium oxide field-effect transistor,” Appl. Phys. Express, vol. 10, no. 5, p. 051102, May 2017, doi: 10.7567/APEX.10.051102.

[281] Z. L. Wang, “Nanowires and Nanobelts: Materials, Properties and Devices. Volume 1: Metal ... - Google Books.”

[282] W. Cui et al., “Electrical and optical properties of In_2O_3 thin films deposited on sapphire substrate,” J. Nanosci. Nanotechnol., vol. 18, no. 2, pp. 1220–1223, 2018, doi: 10.1166/jnn.2018.14111.

[283] S. Nandy, B. Saha, M. K. Mitra, and K. K. Chattopadhyay, “Effect of oxygen partial pressure on the electrical and optical properties of highly (200) oriented p-type $Ni_{1-x}O$ films by DC sputtering,” J. Mater. Sci., vol. 42, no. 14, pp. 5766–5772, Jul. 2007, doi: 10.1007/s10853-006-1153-x.

[284] T. K. Oanh Vu, D. U. Lee, and E. K. Kim, “The effect of oxygen partial pressure on band gap modulation of Ga_2O_3 grown by pulsed laser deposition,” J. Alloys Compd., vol. 806, pp. 874–880, Oct. 2019, doi: 10.1016/j.jallcom.2019.07.326.

[285] S. Ghose et al., “Structural and optical properties of Ga_2O_3 thin films grown by plasma-assisted molecular beam epitaxy,” J. Vac. Sci. Technol. B, Nanotechnol. Microelectron. Mater. Process. Meas. Phenom., vol. 34, no. 2, p. 02L109, Mar. 2016, doi: 10.1116/1.4942045.

[286] S. Ghose et al., “Growth and characterization of β-Ga_2O_3 thin films by molecular beam epitaxy for deep-UV photodetectors,” J. Appl. Phys., vol. 122, no. 9, p. 095302, Sep. 2017, doi: 10.1063/1.4985855.

[287] J. Liu, S. Zou, L. Xiao, and J. Fan, “Well-dispersed bimetallic nanoparticles confined in mesoporous metal oxides and their optimized catalytic activity for nitrobenzene hydrogenation,” Catal. Sci. Technol., vol. 4, no. 2, pp. 441–446, 2014, doi: 10.1039/c3cy00689a.

[288] Z. Chen et al., “Band alignment of Ga_2O_3/Si heterojunction interface measured by X-ray photoelectron spectroscopy,” Appl. Phys. Lett., vol. 109, no. 10, p. 102106, Sep. 2016, doi: 10.1063/1.4962538.

[289] C. Huang et al., “Effect of OH- on chemical mechanical polishing of β-Ga_2O_3 (100) substrate using an alkaline slurry,” RSC Adv., vol. 8, no. 12, pp. 6544–6550, Feb. 2018, doi: 10.1039/c7ra11570a.

[290] P. C. J. Graat and M. A. J. Somers, “Simultaneous determination of composition and thickness of thin iron-oxide films from XPS Fe 2p spectra,” Appl. Surf. Sci., vol. 100–101, pp. 36–40, Jul. 1996, doi: 10.1016/0169-4332(96)00252-8.

[291] S. J. Roosendaal, B. Van Asselen, J. W. Elsenaar, A. M. Vredenberg, and F. H. P. M. Habraken, “The oxidation state of Fe(100) after initial oxidation in O2,” Surf. Sci., vol. 442, no. 3, pp. 329–337, Dec. 1999, doi: 10.1016/S0039-6028(99)01006-7.

[292] S. Song et al., “Ferroelectric polarization switching with a remarkably high activation energy in orthorhombic $GaFeO_3$ thin films,” NPG Asia Mater., vol. 8, no. 2, pp. e242–e242, Feb. 2016, doi: 10.1038/am.2016.3.

[293] R. Saha, A. Shireen, S. N. Shirodkar, U. V. Waghmare, A. Sundaresan, and C. N. R. Rao, “Multiferroic and magnetoelectric nature of $GaFeO_3$, $AlFeO_3$ and related oxides,” Solid State Commun., vol. 152, no. 21, pp. 1964–1968, Nov. 2012, doi: 10.1016/j.ssc.2012.07.018.

[294] S. Mukherjee, A. Roy, S. Auluck, R. Prasad, R. Gupta, and A. Garg, “Room Temperature Nanoscale Ferroelectricity in Magnetoelectric $GaFeO_3$ Epitaxial Thin Films,” Phys. Rev. Lett., vol. 111, no. 8, Feb. 2013, doi: 10.1103/PhysRevLett.111.087601.

[295] F. Tolea, M. N. Grecu, V. Kuncser, S. G. Constantinescu, and D. Ghica, “On the role of Fe ions on magnetic properties of doped TiO_2 nanoparticles,” Appl. Phys. Lett., vol. 106, no. 14, p. 142404, Apr. 2015, doi: 10.1063/1.4917037.

[296] Y. Chen, B. Wu, H. Yuan, Y. Feng, and H. Chen, “The defect-induced changes of the electronic and magnetic properties in the inverse Heusler alloy Ti_2CoAl,” J. Solid State Chem., vol. 221, pp. 311–317, Jan. 2015, doi: 10.1016/j.jssc.2014.08.027.

[297] R. Murugan, G. Vijayaprasath, T. Mahalingam, and G. Ravi, “Defect induced magnetic transition in Co doped CeO2 sputtered thin films,” Ceram. Int., vol. 42, no. 10, pp. 11724–11731, Aug. 2016, doi: 10.1016/j.ceramint.2016.04.091.

[298] B. Pal, D. Sarkar, and P. K. Giri, “Structural, optical, and magnetic properties of Ni doped ZnO nanoparticles: Correlation of magnetic moment with defect density,” Appl. Surf. Sci., vol. 356, pp. 804–811, 2015, doi: 10.1016/j.apsusc.2015.08.163.

[299] J. D. Verhoeven, Fundamentals of physical metallurgy. .

[300] S. Nakagomi and Y. Kokubun, “Crystal orientation of β-Ga_2O_3 thin films formed on c-plane and a-plane sapphire substrate,” J. Cryst. Growth, vol. 349, no. 1, pp. 12–18, Jun. 2012, doi: 10.1016/j.jcrysgro.2012.04.006.

[301] G.-L. Tan, L. Liu, and W. Wu, “Mid-IR band gap engineering of $Cd_xPb_{1-x}S$ nanocrystals by mechanochemical reaction,” J. Chem. Phys., vol. 4, p. 20018, 2014, doi: 10.1063/1.4881878.

[302] A. Srivastava, S. N. Tiwari, M. A. Alvi, and S. A. Khan, “Phase change studies in Se85In15-xZnx chalcogenide thin films,” J. Appl. Phys., vol. 123, no. 12, p. 125105, Mar. 2018, doi: 10.1063/1.5018777.

[303] W. C. Shih and M. S. Wu, “Growth of ZnO films on GaAs substrates with a SiO_2 buffer layer by RF planar magnetron sputtering for surface acoustic wave applications,” J. Cryst. Growth, vol. 137, no. 3–4, pp. 319–325, Apr. 1994, doi: 10.1016/0022-0248(94)90968-7.

[304] M. K. Puchert, P. Y. Timbrell, and R. N. Lamb, “Postdeposition annealing of radio frequency magnetron sputtered ZnO films,” J. Vac. Sci. Technol. A Vacuum, Surfaces, Film., vol. 14, no. 4, pp. 2220–2230, Jul. 1996, doi: 10.1116/1.580050.

[305] F. Otieno, M. Airo, R. M. Erasmus, D. G. Billing, A. Quandt, and D. Wamwangi, “Effect of thermal treatment on ZnO:Tb^{3+} nano-crystalline thin films and application for spectral conversion in inverted organic solar cells,” RSC Adv., vol. 8, no. 51, pp. 29274–29282, Aug. 2018, doi: 10.1039/c8ra04398a.

[306] S. R. Thomas et al., “High electron mobility thin-film transistors based on Ga_2O_3grown by atmospheric ultrasonic spray pyrolysis at low temperatures,” Appl. Phys. Lett., vol. 105, no. 9, p. 092105, Sep. 2014, doi: 10.1063/1.4894643.

[307] C. V. Ramana et al., “Chemical bonding, optical constants, and electrical resistivity of sputter-deposited gallium oxide thin films,” J. Appl. Phys., vol. 115, no. 4, p. 043508, Jan. 2014, doi: 10.1063/1.4862186.

[308] H. Cui, Q. Sai, H. Qi, J. Zhao, J. Si, and M. Pan, “Analysis on the electronic trap of β-Ga_2O_3 single crystal,” J. Mater. Sci., vol. 54, no. 19, pp. 12643–12649, Oct. 2019, doi: 10.1007/s10853-019-03777-1.

[309] B. Zheng, W. Hua, Y. Yue, and Z. Gao, “Dehydrogenation of propane to propene over different polymorphs of gallium oxide,” J. Catal., vol. 232, no. 1, pp. 143–151, May 2005, doi: 10.1016/j.jcat.2005.03.001.

[310] V. V. Atuchin, A. V. Kalinkin, V. A. Kochubey, V. N. Kruchinin, R. S. Vemuri, and C. V. Ramana, “Spectroscopic ellipsometry and x-ray photoelectron spectroscopy of La_2O_3 thin films deposited by reactive magnetron sputtering,” J. Vac. Sci. Technol. A Vacuum, Surfaces, Film., vol. 29, no. 2, p. 021004, Mar. 2011, doi: 10.1116/1.3539069.

[311] V. V. Atuchin, L. D. Pokrovsky, O. Y. Khyzhun, A. K. Sinelnichenko, and C. V. Ramana, “Surface crystallography and electronic structure of potassium yttrium tungstate,” J. Appl. Phys., vol. 104, no. 3, p. 033518, Aug. 2008, doi: 10.1063/1.2963957.

[312] T. Yamashita and P. Hayes, “Analysis of XPS spectra of Fe 2+ and Fe 3+ ions in oxide materials,” Appl. Surf. Sci., vol. 254, no. 8, pp. 2441–2449, Feb. 2008, doi: 10.1016/j.apsusc.2007.09.063.

[313] P. C. J. Graat and M. A. J. Somers, “Simultaneous determination of composition and thickness of thin iron-oxide films from XPS Fe 2p spectra,” Appl. Surf. Sci., vol. 100–101, pp. 36–40, Jul. 1996, doi: 10.1016/0169-4332(96)00252-8.

[314] de, Regt, van, Dijk, van Mullen, D. Schram, and J. van Dijk, “Components of continuum radiation in an inductively coupled plasma,” J. Phys. D. Appl. Phys., vol. 28, no. 1, pp. 40–46, 1995, doi: 10.1088/0022-3727.

[315] M. Oku, K. Wagatsuma, and H. Matsuta, “Background subtraction from transition metal 2p XPS by deconvolution using ligand atom XPS: Study on first transition metal cyanide complexes,” J. Electron Spectros. Relat. Phenomena, vol. 83, no. 1, pp. 31–39, Jan. 1997, doi: 10.1016/S0368-2048(96)03075-7.

[316] M. Muhler, R. Schlögl, and G. Ertl, “The nature of the iron oxide-based catalyst for dehydrogenation of ethylbenzene to styrene 2. Surface chemistry of the active phase,” J. Catal., vol. 138, no. 2, pp. 413–444, Dec. 1992, doi: 10.1016/0021-9517(92)90295-S.

[317] M. H. Hamed, D. N. Mueller, and M. Müller, “Thermal phase design of ultrathin magnetic iron oxide films: From Fe_3O_4 to γ-Fe_2O_3 and FeO,” J. Mater. Chem. C, vol. 8, no. 4, pp. 1335–1343, 2020, doi: 10.1039/c9tc05921k.

[318] T. Fujii, F. M. F. de Groot, G. A. Sawatzky, F. C. Voogt, T. Hibma, and K. Okada, “In situ xps analysis of various iron oxide films grown by (formula presented)-assisted molecular-beam epitaxy,” Phys. Rev. B - Condens. Matter Mater. Phys., vol. 59, no. 4, pp. 3195–3202, Jan. 1999, doi: 10.1103/PhysRevB.59.3195.

[319] F. Wu et al., “One-step synthesis of hierarchical metal oxide nanosheet/carbon nanotube composites by chemical vapor deposition,” J. Mater. Sci., vol. 54, no. 2, pp. 1291–1303, Jan. 2019, doi: 10.1007/s10853-018-2889-9.

[320] A. Yazdanbakhsh, Y. Hashempour, and M. Ghaderpouri, “Performance of granular activated carbon/nanoscale zero-valent iron for removal of humic substances from aqueous solution based on experimental design and response surface modeling,” Glob. Nest J., vol. 20, no. 1, pp. 57–68, Feb. 2018, doi: 10.30955/gnj.002264.

[321] A. Sellai, “Electrical characteristics of InAs self-assembled quantum dots embedded in GaAs using admittance spectroscopy,” J. Nanophotonics, vol. 6, no. 1, p. 063502, 2012, doi: 10.1117/1.JNP.6.063502.

[322] L. Yin, I. Adler, T. Tsang, L. J. Matienzo, and S. O. Grim, “Paramagnetism and shake-up satellites in X-ray photoelectron spectra,” Chem. Phys. Lett., vol. 24, no. 1, pp. 81–84, Jan. 1974, doi: 10.1016/0009-2614(74)80219-8.

[323] S. C. Abrahams and J. M. Reddy, “Magnetic, electric, and crystallographic properties of gallium iron oxide,” Phys. Rev. Lett., vol. 13, no. 23, pp. 688–690, Dec. 1964, doi: 10.1103/PhysRevLett.13.688.

[324] R. Allen Kellogg and R. Allen, “Development and modeling of iron-gallium alloys Recommended Citation,” 2006.

[325] H. Yan et al., “Magnetic properties and crystal structure of $Ga_{2-x}Fe_xO_3$,” Powder Diffr., vol. 33, no. 3, pp. 195–201, Sep. 2018, doi: 10.1017/S0885715618000374.